Band structure calculation of Si-Ge-Sn binary and ternary alloys, nanostructures and devices

Pairot Moontragoon

The University of Leeds
School of Electronic and Electrical Engineering
Institute of Microwaves and Photonics

September 2009

Submitted in accordance with the requirements for the degree of Doctor of Philosophy.

The candidate confirms that the work submitted is his own and that appropriate credit has been given where reference has been made to the work of others.

Acknowledgments

I would like to express my appreciation and gratitude to all the people who have helped me with this dissertation.

Firstly, I would like to gratefully acknowledge the excellent supervision of Dr Zoran Ikonić and Professor Paul Harrison during this work for their support, patience and encouragement throughout the project. With their inspiration and enthusiasm, they led me to make this a success. They offered me exceptional insight and prepared me for future challenges. The professional research skills and personal lessons that I have learnt from them are invaluable for future endeavors. Without their invaluable and professional supervision, I could not achieve the objectives of the project. I also thank Dr Nenad Vukmirović for sharing his strong experience in physics of nanostructures. I would also like to thank all my office mates, Alexander Valavanis, Theerapong Puangmali, Goran Isic, Dr. Leon Lever, and Dr. Craig Evans, for providing a pleasant research atmosphere.

Secondly, I would like to my sponsors. My PhD research was funded by the Royal Thai Government Scholarship and Khon kaen University.

My thanks also go to all the members of staff of the Jino's Thai Cafe who gave me friendship in part time job.

Finally, my Wife and my parents in'law receive my deepest gratitude and love for their mental support during my studies in the United Kingdom. I am also indebted to my parents and my brothers for their understanding and encouragement when it was most required.

Abstract

Alloys of silicon (Si), germanium (Ge) and tin (Sn) are continuously attracting research attention as possible direct band gap semiconductors with prospective applications in optoelectronics. The direct gap property may be brought about by the alloy composition alone or combined with the influence of strain, when an alloy layer is grown on a virtual substrate of different composition. Si-Ge-Sn nanostructures are also promising materials because they are compatible with Si-based technology, and have a high potential in many optoelectronic applications, such as silicon-based Ge/SiGeSn band-to-band and inter-subband lasers.

In search for direct gap materials, the electronic structure of relaxed or strained $Ge_{1-x}Sn_x$ and $Si_{1-x}Sn_x$ alloys, and of strained Ge grown on relaxed $Ge_{1-x-y}Si_xSn_y$, were calculated by the self-consistent pseudo-potential plane wave method, within the mixed-atom supercell model of alloys, which was found to offer a much better accuracy than the virtual crystal approximation. Expressions are given for the direct and indirect band gaps in relaxed $Ge_{1-x}Sn_x$, strained Ge grown on relaxed $Si_xGe_{1-x-y}Sn_y$, and for strained $Ge_{1-x}Sn_x$ grown on a relaxed $Ge_{1-y}Sn_y$ substrate, and these constitute the criteria for achieving a direct band gap semiconductor, by using appropriate tensile strain. In particular, strained Ge on relaxed $Si_xGe_{1-x-y}Sn_y$ has a direct gap for $y > 0.12 + 0.20x$, while strained $Ge_{1-x}Sn_x$ on relaxed $Ge_{1-y}Sn_y$ has a direct gap for $y > 3.2x^2 - 0.07x + 0.09$. In contrast, within the mixed-atom approach the Sn_xSi_{1-x} alloys never show a finite direct band gap (while the VCA calculation does predict it).

Self-assembled quantum dots in Si-Ge-Sn system attract research attention as possible direct band gap materials, compatible with Si-based technology, with potential applications in optoelectronics. In this work, the electronic structure near the Γ-point and interband optical matrix elements of strained Sn and SnGe quantum dots in Si or Ge matrix are calculated using the eight-band $\mathbf{k}\cdot\mathbf{p}$ method, and the competing L-valley conduction band states were found by the effective mass method. The strain distribution in the dots was found with the continuum mechanical model. The parameters required for the $\mathbf{k}\cdot\mathbf{p}$ or effective mass calculation for Sn were extracted by fitting to the energy band structure calculated by the nonlocal empirical pseudopotential method (EPM). The calculations show that the self-assembled Sn/Si dots, sized between 4 nm and 12 nm, have indirect interband transition energies between 0.8 to 0.4 eV and direct interband transitions between 2.5 to 2.0 eV. In particular, the actually grown, approximately cylindrical Sn dots in Si with a diameter and height of about 5 nm are calculated to have an indirect transition (to the L valley) of about 0.7 eV, which agrees very well with experimental results. Similar good agreement with experiment was also found for SnGe dots grown on Si. However, neither of these are predicted to be direct band gap materials, in contrast to some earlier expectations.

In order to extend a creativity in developing a complete suite of Si-base optoelectronic devices, SiGeSn alloys are considered as promising materials for optoelectronic applications because they offer the possibility for a direct band gap and are compatible with Si-based technology, therefore having a perspective of applications for interband lasers and detectors, solar cells, etc. In this work, another possible application of nanostructures based on these materials was considered: to extend the suite of Si-based optoelectronic devices, namely for interband electro-absorption modulators. Using the 8-band k.p method asymmetric double quantum wells have been designed and optimized, by varying the well and barrier widths and material composition, to show large optical transmission sensitivity to the applied bias. Generally, these structures are useful for electro-absorption modulators in the mid-infrared spectral range.

Contents

Publications

Papers in peer reviewed journals [1]

1. ⋆ **P. Moontragoon**, Z. Ikonić, and P. Harrison, "Band structure calculations of SiGeSn alloys: achieving direct band gap materials", *Semicond. Sci. Technol.* **22**, 742 (2007).
2. ⋆ **P. Moontragoon**, N. Vukmirović, Z. Ikonić, and P. Harrison, "Electronic structure and optical properties of Sn and SnGe quantum dots", *J. Appl. Phys.* **103**, 103712 (2008).
3. ⋆ **P. Moontragoon**, N. Vukmirović, Z. Ikonić, and P. Harrison, "Electronic structure and optical transitions in Sn and SnGe quantum dots in a Si matrix", *Microelectronics Journal* **40**, 483 (2009).
4. ⋆ **P. Moontragoon**, N. Vukmirović, Z. Ikonić, and P. Harrison, "SnGe asymmetric quantum well electro-absorption modulators for long-wave silicon photonics", accepted in IEEE Selected Topics in Quantum Electronics.

Seminars

1. "Optical properties of Si-Ge-Sn quantum dots", Quantum Dots Optoelectronics Symposium, Limassol, Cyprus, 14-16 November 2007.
2. "Band structure calculation of Si-Ge-Sn binary and ternary alloys", Rank Prize Funds Mini-Symposium on Si-Based Optoelectronics, Windermere,

---

[1] Key journal papers are marked with ⋆

Lake District, UK, 3–6 April 2006.

Conference papers

1. P. Moontragoon, Z. Ikonić, P. Harrison, "Band structure calculation of Si-Ge-Sn binary and ternary alloys", Rank Prize Funds Mini-Symposium on Si-Based Optoelectronics, Windermere, Lake District, UK, 3–6 April 2006.

2. P. Moontragoon, N. Vukmirović, Z. Ikonić, P. Harrison, "Optical properties of Si-Ge-Sn quantum dots", Quantum Dot Optoelectronics Symposium – QDOS2007, Limassol, Cyprus, 14–16 Nov. 2007, Technical Digest.

3. P. Moontragoon, N. Vukmirović, Z. Ikonić, P. Harrison, "Direct and indirect optical transitions in Sn and SnGe quantum dots in Si matrix", UK Semiconductors 2008, Sheffield, UK, 2–3 July 2008, Abstract Book, poster E-P-6.

4. Z. Ikonić, P. Harrison, P. Moontragoon, N. Vukmirović, "SiGeSn alloys for infrared emission and detection applications", (invited talk), Silicon Based Emission Technology Conference (SiBET 2009), Manchester, UK, 14–17 June 2009, Book of Abstracts.

5. P. Moontragoon, N. Vukmirović, Z. Ikonić, P. Harrison, "Infrared optical properties of SiGeSn nanostructures", Silicon Based Emission Technology Conference (SiBET 2009), Manchester, UK, 14–17 June 2009, Book of Abstracts.

List of Figures

List of Tables

List of Principal Abbreviations

MBE	Molecular Beam Epitaxy
UHV-VCD	Ultra-High-Vacuum Chemical Vapor Deposition
MOCVD	Metalorganic Chemical Vapour Deposition
RBS	Rutherford Back Scattering
VCA	Virtual Crystal Approximation
CPA	Coherent Potential Approximation
EAMs	Electroabsorption Modulators
ADQWs	Asymmetric Double Quantum Wells
SQWs	single quantum wells
LIO	Longwave Integrated Optoelectronics
CB	conduction band
VB	valence band
BZ	Brillouin zone
DFT	Density Functional Theory
EPM	Empirical Pseudopotential Method
VFF	Valence Force Field
CM	Continuum Mechanical
WEM	Wavefunction Expansion Method
FDM	Finite Difference Method
SCBA	Self-consistent Born Approximation

Chapter 1

Introduction

1.1 Introduction

In recent years, optoelectronics has moved into widespread use. It is because of that there is an increasing need for optoelectronic devices in many branches of technology, such as optoelectronic devices in telecommunications, transportation, medical, computer and entertainment industries. Additionally, due to the high demand of consumers in the transfer of tremendous amount of information with high speed, there are many attempts to enhance the efficiency of electronic and communication devices, by increasing their speed and bandwidth. In order to achieve a high speed of data transfer in electronic equipment, the fascinating idea of optically integrated circuits (IC) has been introduced. This concept is an integration between optical devices and the widely used technology of silicon-based electronic devices. Unfortunately, silicon is an indirect band gap semiconductor which is infamous for its low radiative efficiency. Inevitably, this technology still has to rely on direct band gap semiconductors, such as gallium arsenide (GaAs) which is expensive and highly toxic. Therefore, an interesting idea for optoelectronics is finding a new tuneable direct band gap semiconductor which is easily compatible with silicon and abundant in order to reduce the production cost. One solution could be in design and fabrication of an artificial group IV material. The epitaxial growth of random alloys of group IV semiconductors has been widely investigated because of their potential use in optoelectronic devices. Among the materials in this group, the alloys of silicon (Si), germanium (Ge) and tin (Sn), including the binary $Ge_{1-x}Sn_x$ material are the most interesting. As a result of the particular band structure of alpha-Sn, which is a zero direct band gap semiconductor, alloys of Si, Ge and Sn attract research attention as possible direct band gap semiconductors with potential applications in optoelectronic devices, compatible with widely used silicon technology.

1.2 Physical and optical properties of bulk silicon, germanium and alpha-tin

Silicon has the diamond type of crystal structure, which is the face centered cubic lattice with two identical basis atoms, displaced by one quarter of the body diagonal, so their coordinates are e.g. (0,0,0) and (1/4,1/4,1/4) in cubic lattice constant units. This is shown in Fig.2.4 in Sec. 2.3. Unlike the zinc-blende crystal structure such as GaAs or AlAs in which the two atomic sites are of different type, silicon does not have polarity which is present in III-V binary compounds. The lattice constant of silicon is 5.431 Å, density 2.329 $g{\cdot}cm^{-3}$ and its dielectric constant is 11.7 [1]. The indirect bandgap of silicon is 1.12 eV at room temperature, and occurs towards the conduction band L valley minimum, at the L point of the first Brillouin zone [2], (Fig. 1.1, see also Sec. 2.3). Therefore, non-radiative recombination in silicon is dominant, which causes very low luminescence efficiency. Similar to silicon, germanium also has the diamond crystal structure with lattice constant, density and dielectric constant of 5.658 Å, 5.3234 $g{\cdot}cm^{-3}$ and 16.2 respectively [1]. According to the band structure illustrated in Fig. 1.1, germanium is also an indirect bandgap semiconductor. The minimum energy bandgap is 0.661 eV is at the L point of the first Brillouin zone while the energy bandgap at the Γ point is 0.8 eV, at room temperature.

In order to overcome the indirect bandgap limitations in light emission from Si and Ge, the idea of material engineering has been introduced, especially the energy band engineering. There are different possibilities of achieving this

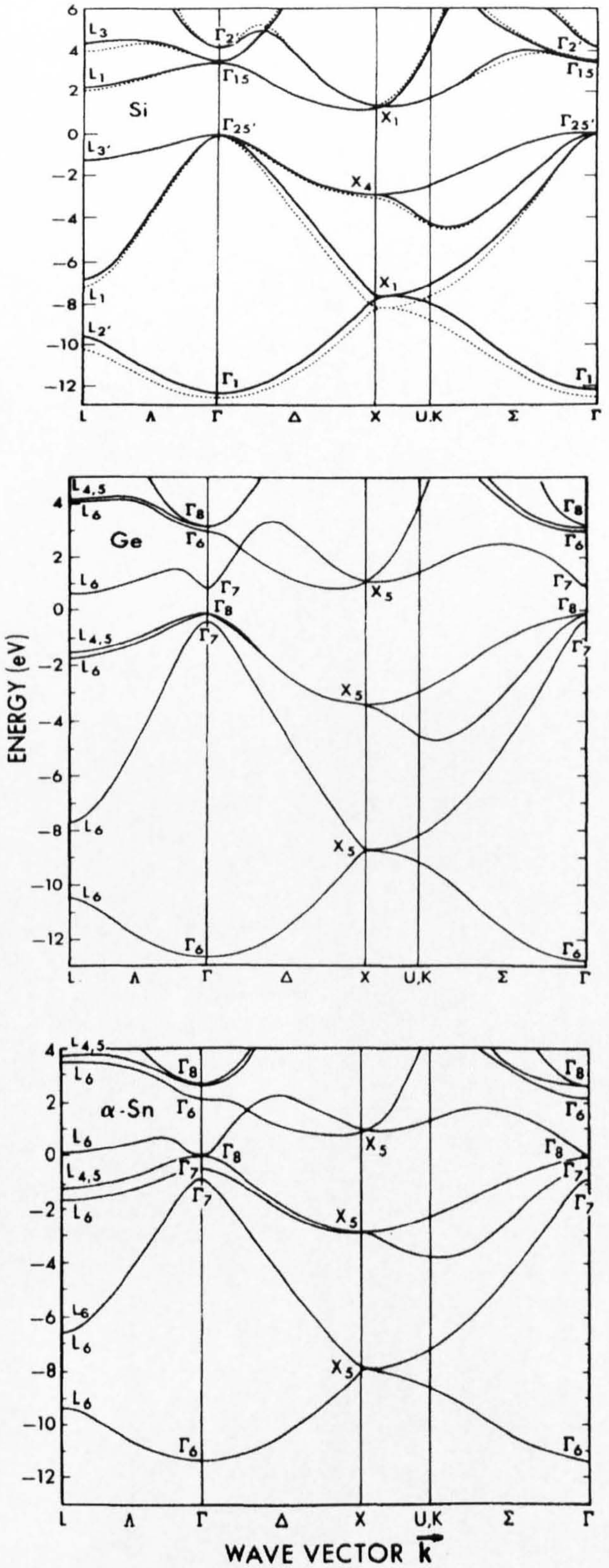

Figure 1.1: Band structure of silicon, germanium, and α-tin along different high-symmetry directions of the first Brillouin zone [3].

goal [2]:

- Localization of the wavefunctions of electrons and holes via quantum confinement (nanoclusters and quantum wells, wires and dots) and band structure engineering so that the nonradiative recombination lifetime is very long and increases the efficiency of the radiative luminescence.
- Forming alloys, molecules and clusters so that the energy gap of the material or wavelength of emitted photon can be tuned.
- Using intraband transitions, within the conduction band or valence band, so that the indirect bandgap becomes irrelevant.

Band structure engineering via alloy formation can improve the electroluminescence and photoluminescence intensity, for example the intensity of $\mathrm{Si}_{1-x}\mathrm{Ge}_x$ is higher than that of Si. Furthermore, alloys also change the minimum energy bandgap point from near X point to L point, depending on the Ge composition x. The indirect-direct energy bandgap transition can be achieved by forming alloys of silicon and germanium with a suitable semiconductor which has the lowest bandgap at Γ point, and is compatible with silicon and germanium. Considering the physical and optical properties of silicon and germanium, the semiconductor with which Si and Ge should form alloys is α-Sn. It belongs to group IV semiconductors like silicon and germanium. Its crystal structure is also diamond-type with lattice constant, density and dielectric constant of 6.489 Å, 5.769 $\mathrm{g{\cdot}cm^{-3}}$ and 24 respectively. The energy band structure is displayed in Fig. 1.1.

1.3 New direct band gap semiconductors

In early studies of epitaxial Si, Ge, Sn alloys no reliable method of growing these alloys was found, except for $\mathrm{Si}_{1-x}\mathrm{Ge}_x$ binary alloys. The difficulty in the growth of $\mathrm{Ge}_{1-x}\mathrm{Sn}_x$ alloys is the large lattice mismatch, segregation on interfaces and the instability of the alpha-tin structure. Hence, $\mathrm{Ge}_{1-x}\mathrm{Sn}_x$ bulk alloys cannot be readily grown. However, using the new technology of film growth, called low temperature molecular beam epitaxy (MBE), vital progress of epitaxial growth of $Ge_{1-x}Sn_x$ has been made. For example, there is an achievement of growing fully strained $Ge_{1-x}Sn_x$, but it is believed that they do not show indirect-to-direct transitions. This is because of their compressive strain. Thus, it is believed that indirect-to-direct transition can only occur in tensile strained or strain-free $Ge_{1-x}Sn_x$, e.g. in the work of G. He and H. A. Atwater which showed interband transitions with a change in direct energy gap of $0.35 < E_g < 0.80$ eV for $0.15 > x > 0$ [4]. Although growth of $Ge_{1-x}Sn_x$ can be achieved, the limitation on the thickness of the epitaxial alloys and the surface segregation of tin are still problematic. By other technologies of epitaxial growth, i.e. novel chemical methods based on deuterium-stabilized Sn hydrides and ultra-high-vacuum chemical vapor deposition (UHV-VCD), uniform homogeneous relaxed $Ge_{1-x}Sn_x$ alloys with composition of tin less than 0.2 ($x < 0.2$), determined by Rutherford backscattering (RBS), have been grown directly on silicon substrates. In order to understand its optical and physical properties, its complex pseudo-dielectric function and the film thickness, were investigated by spectroscopic ellipsometry.

Although still waiting for clear experimental confirmation, it is believed that the binary alloy of Ge and Sn, as well as ternary alloys of Si, Ge, Sn, could be very fascinating materials for infrared detectors. This is due to the theoretical prediction by Soref and Perry [5] who used a linear interpolation scheme and calculated the energy bands and optical indices of $Ge_{1-x-y}Si_xSn_y$ alloys, and concluded that these alloys will be direct tunable band gap semiconductors when they are grown with an appropriate composition of silicon, germanium and tin.

A number of researchers have investigated some important properties of these alloys, by using quantum mechanical band structure theory and explored the influence of random fluctuations of the composition of SiGeSn alloys on their electronic properties by using different models, like the virtual crystal approximation (VCA) with the tight-binding method or with the pseudopotential method. In order to take into account the disorder effects of an alloy, the Coherent Potential Approximation (CPA) was introduced and successfully applied to $Si_{1-x}Ge_x$ alloys. However, so far there is no theoretical model which properly describes the optical properties of GeSiSn alloys. Thus, the aim of this work is to use theoretical simulation to show the possibility of achieving a direct tunable semiconductor in group IV, and to investigate the composition dependence of the electronic properties. The most vital objective is engineering a tunable direct energy gap semiconductor and finding its optical parameters in order to be able to design optoelectronic devices.

1.4 The SiGeSn nanostructures as revolutionary semiconductor devices

With a remarkable progress in cutting edge technology, the production of semiconductor structures of nanometer sizes became possible, and many prospective applications are rapidly emerging. Self-assembled Sn quantum dots embedded in Si have been successfully grown in recent years. It was anticipated that these would also be important nanostructures for optoelectronic devices, because of their potential for synthesis of a Si-based direct bandgap semiconductor, a property not found in the more conventional Ge and SiGe quantum dots. Although bulk Sn is a direct zero band gap semiconductor, the gap at the Γ point is expected to increase, as a combined result of quantum confinement and strain. Among possible important optoelectronic devices are electroabsorption modulators (EAMs) because of their high modulation efficiency and small size. These can be engineered as asymmetric double quantum wells (ADQWs), and can potentially be optimized to exhibit superior extinction ratio to single quantum wells (SQWs), as is required for digital optical modulation. The group IV alloys thus hold a promise of long wavelength silicon technology applications, such as for chemical and biological agents detectors, infrared detectors and Longwave Integrated Optoelectronics (LIO) [6].

1.5 Thesis outline

From the discussion presented, one can see that the prospect of having SiGeSn semiconductor devices in the future has not been fully exploited. While this is partly due to difficulties in experimentally desired characteristics, there is also a lack of theoretical understanding of their properties. The goal of this thesis is to bridge this gap by investigating the electronic and interband optical properties of SiGeSn material, including binary alloys, ternary alloys and nanostructures, of interest for future semiconductor devices. The organization of this thesis is as follows. In chapter 2, the theoretical frameworks which are used throughout this thesis, the density functional, empirical pseudopotential and $\mathbf{k} \cdot \mathbf{p}$ method, will be described. Band structure calculations of Si-Ge-Sn alloys are performed, including those for pure silicon, germanium and alpha-tin. Moreover, the model which explains the behavior of the alloys and the validity of the models is also given. In order to search for a direct band gap semiconductor, the results of calculation of composition dependence of energy band structure of relaxed $\mathrm{Ge}_{1-x}\mathrm{Sn}_x$ and strained Ge on relaxed $\mathrm{Ge}_{1-x-y}\mathrm{Si}_x\mathrm{Sn}_y$ alloys, strained $\mathrm{Ge}_{1-x}\mathrm{Sn}_x$ on relaxed $\mathrm{Ge}_{1-y}\mathrm{Sn}_y$, and of relaxed $\mathrm{Si}_{1-x}\mathrm{Sn}_x$ alloys are presented in chapter 3. In chapter 4, the single-particle states and interband absoprtion in Sn or SnGe dots within the framework of $\mathbf{k} \cdot \mathbf{p}$ method are calculated. Due to the lack of some of material parameters for Sn, these were extracted from empirical nonlocal pseudopotentials, as described in detail. The results of this study are presented, with special attention devoted to the issue of the nature of the band gap of quantum dot material, which is relevant for optoelectronic devices. In chapter 5, the asymmetric double quantum well structures which have a strong electric field sensitivity, are designed within the framework of $\mathbf{k} \cdot \mathbf{p}$ method. Asymmetric double quantum wells (ADQWs) are optimized to exhibit maximum optical modulation sensitivity by varying the barrier width, barrier position, and well width. The required Sn composition of the layers are investigated in order to have interband transition energy in the photon wavelength ranges of interest. The electronic structure, optical properties, and the absorption coefficient are calculated. Finally, chapter 6 is a conclusion and discussion of topics for future investigations.

Chapter 2

Theoretical framework

2.1 Introduction

In this chapter, the theoretical frameworks which are used throughout this thesis, the density functional, empirical pseudopotential, and the $\mathbf{k} \cdot \mathbf{p}$ method, will be described. The density functional theory including some approximations, which is an approach used to simplify solving the complicated problem of many electrons moving in an induced potential field, is introduced and the energy band structure and electron charge density of elemental silicon, germanium and alpha-tin are presented. The physical system of interest consists not only of electrons but also of nuclei, and each of these particles move in the field generated by others so, in this chapter, the Hartree-Fock theory and the density functional theory, which are two different approaches to the many-body problem, are discussed. Both theories are the simplification of the full problem of many electrons moving in a potential field. The empirical pseudopotential is one of a variety of different forms of pseudopotential, fitted to reproduce experimental results. It can be used to calculate properties of a large number of semiconductors because it is simple, easy to implement and accurate.

The $\mathbf{k} \cdot \mathbf{p}$ method is an efficient framework to accurately describe either the conduction band (CB), or the valence band (VB), or both, near a given point of the Brillouin zone (BZ). The simplest version of this method is the well known effective mass method which can describe semiconductor properties in the conduction band and, to the first approximation, in the valence band.

The general idea of the **k** · **p** method is to expand the wavefunctions in a limited number of bulk Bloch bands at some characteristic point, usually the point $\mathbf{k} = 0$ or Γ-point. Throughout this work, the 8-band Hamiltonian, which simultaneously describes the top three valence bands and the bottom of the conduction band, has been adopted because interband transitions were interested. It also can include the effects of band mixing, strain, as well as the influence of external fields, while one can keep a lower computational cost when compared to atomistic methods, as described in more detail below.

2.2 Self-consistent local density functional pseudopotential method

2.2.1 The Hamiltonian of a solid

Based on solving a many-body Schrödinger equation [7–11], consider a system of ions and interacting electrons, consisting of N electrons and K nuclei. The Schrödinger equation has the form

$$H\Psi\left(\{\mathbf{R}_I;\mathbf{r}_i\}\right) = E\Psi\left(\{\mathbf{R}_I;\mathbf{r}_i\}\right), \tag{2.1}$$

where E is the energy of the system, $\Psi\left(\{\mathbf{R}_I;\mathbf{r}_i\}\right)$ is the many-body wave function which describes states of the system and is a function of the positions of the ions ($\mathbf{R}_I$) and the electrons ($\mathbf{r}_i$), and H is the Hamiltonian of this system, consisting of the kinetic energy operators and the potential energy due to the interaction between ions and the electrons. The former has the kinetic energies of both nuclei and electrons, i.e.

$$-\sum_{I=1}^{K}\frac{\hbar^2}{2M_I}\nabla^2_{\mathbf{R}_I} - \sum_{i=1}^{N}\frac{\hbar^2}{2m_e}\nabla^2_{\mathbf{r}_i},$$

where $\hbar$ is Planck's constant divided by 2π, M_I and m_e are the masses of nuclei and electron respectively. The latter, known as the interaction potential, includes interaction between ions and ions, interaction between electrons and ions and interaction between electrons and electrons. Firstly, the ion-ion interaction potential which is a repulsive energy of ions at R_I and R_J is written as

$$\frac{1}{4\pi\epsilon_o}\frac{Z_I Z_J e^2}{|\mathbf{R}_I - \mathbf{R}_J|},$$

where Z_I is the atomic number of nucleus I and e is the electronic charge. The second term is the attractive energy which is produced by the interaction of the electron at a position $\mathbf{r}$ in the potential field of positive charge of every ion in the system. This electron-ion potential can be written in the form

$$V_{el-ion} = -\frac{1}{4\pi\epsilon_o}\sum_{I=1}^{N}\frac{Z_I e^2}{|\mathbf{R}_I - \mathbf{r}|},$$

where V_{el-ion} is the total ion potential. Finally, two electrons which are described by variables r_i and r_j repel each other, which produces the electron-electron interaction potential

$$\frac{1}{4\pi\epsilon_o}\frac{e^2}{|\mathbf{r}_i - \mathbf{r}_j|}.$$

Therefore, the Hamiltonian of the system becomes

$$\begin{aligned} H \; = \; & -\sum_{I=1}^{K}\frac{\hbar^2}{2M_I}\nabla^2_{\mathbf{R}_I} - \sum_{i=1}^{N}\frac{\hbar^2}{2m_e}\nabla^2_{\mathbf{r}_i} + \frac{1}{2}\frac{1}{4\pi\epsilon_o}\sum_{i,j=1;i\neq j}^{N}\frac{e^2}{|\mathbf{r}_i - \mathbf{r}_j|} \\ & -\frac{1}{4\pi\epsilon_o}\sum_{I=1}^{K}\sum_{i=1}^{N}\frac{Z_I e^2}{|\mathbf{R}_I - \mathbf{r}_i|} + \frac{1}{2}\frac{1}{4\pi\epsilon_o}\sum_{I,J=1;I\neq J}^{K}\frac{Z_I Z_J e^2}{|\mathbf{R}_I - \mathbf{R}_J|}. \end{aligned} \tag{2.2}$$

It is very difficult to solve the stationary Schrödinger equation for this Hamiltonian directly. However, to simplify this Hamiltonian and system, some approximations are introduced in view of the fact that ions move slowly in space when compared with electrons. This approximation is called the Born-Oppenheimer approximation [12]. It takes advantage of the fact that, in a system consisting of both heavy particles such as ions and light particles such as electrons, the motion of the nuclei is slower than that of electrons because the mass of a proton or a neutron is about 1835 times larger than the electron mass. Therefore, it is reasonable to separate the degrees of freedom, related to the motion of the nuclei, from those of the electrons. Moreover, it is clear that the ion-ion interaction, known as the Madelung energy, is constant for a given structure. Therefore, the Born-Oppenheimer Hamiltonian for the electrons can be written as:

$$\begin{aligned} \hat{H}_{BO} &= -\sum_{i=1}^{N} \frac{\hbar^2}{2m_e} \nabla^2_{\mathbf{r}_i} + \frac{1}{2} \frac{1}{4\pi\epsilon_o} \sum_{i,j=1;i \neq j}^{N} \frac{e^2}{|\mathbf{r}_i - \mathbf{r}_j|} \\ &- \frac{1}{4\pi\epsilon_o} \sum_{I=1}^{K} \sum_{i=1}^{N} \frac{Z_I e^2}{|\mathbf{R}_I - \mathbf{r}_i|}. \end{aligned} \tag{2.3}$$

However, this Hamiltonian is still too complicated to be dealt with. In the next section, a further approximation, known as the one-electron approximation, is introduced.

2.2.2 One Electron Approximation

This approximation is based on the fact that all electrons are identical particles and also on the assumption that they are independent particles, so each can be treated as a particle moving in a mean field potential $V^{\text{eff}}(\mathbf{r})$ and can be considered separately. The reason why the one electron approximation can reduce the complexity of the system is that the a complexity of the Hamiltonian is pushed into the mean field potential, which represents the effects of all the other particles in the system. This approximation was first considered by Hartree. The one-electron equation is then of the form:

$$\left\{ -\frac{\hbar^2}{2m_e} \nabla^2 + V_i^{\text{eff}}(\mathbf{r}) \right\} \psi_i(\mathbf{r}) = \epsilon_i \psi_i(\mathbf{r}), \tag{2.4}$$

where $-\hbar^2 \nabla^2 / 2m_e$ is the kinetic energy operator, $\psi_i(\mathbf{r})$ are the one-electron wave functions, that must satisfy the normalization condition and ϵ_i are eigenenergies of electrons. All $\psi_i(\mathbf{r})$ can then be used as a basis to construct a many-body wave function Ψ.

2.2.3 Hartree Approximation

In accordance with the assumption that the electrons are independent particles, it is reasonable to adopt, as Hartree stated, that the N-electron wave function

Ψ is just the product of one-electron wave functions

$$\Psi(\mathbf{r}_1,\mathbf{r}_2,...,\mathbf{r}_N) = \psi_1(\mathbf{r}_1)\psi_2(\mathbf{r}_2)...\psi_N(\mathbf{r}_N), \tag{2.5}$$

where $\psi(\mathbf{r})$ are one-electron wave functions. This many-body wave function can be used to find the expectation value of the Hamiltonian as:

$$\begin{aligned}\langle\Psi|\hat{H}|\Psi\rangle &= \sum_{i=1}^{N}\int d\mathbf{r}\psi_i^*(\mathbf{r})\left(-\frac{\hbar^2}{2m_e}\nabla^2 - \frac{1}{4\pi\epsilon_0}\sum_{I=1}^{K}\frac{Z_I e^2}{|\mathbf{R_I}-\mathbf{r_i}|}(\mathbf{r})\right)\psi_i(\mathbf{r})\\ &+\frac{1}{2}\frac{1}{4\pi\epsilon_0}\sum_{i=1}^{N}\sum_{j\neq i}^{N}\int\frac{e^2}{|\mathbf{r_1}-\mathbf{r_2}|}|\psi_i(\mathbf{r_1})|^2|\psi_j(\mathbf{r_2})|^2 d\mathbf{r}_1 d\mathbf{r}_2.\end{aligned} \tag{2.6}$$

This leads to a set of one-electron equations which are known as the Hartree equations:

$$\left\{-\frac{\hbar^2}{2m_e}\nabla^2 + V_i^{\text{eff}}(\mathbf{r})\right\}\psi_i(\mathbf{r}) = \epsilon_i\psi_i(\mathbf{r}), \tag{2.7}$$

It can be easily shown that in the Hartree approximation,

$$V_i^{\text{eff}}(\mathbf{r}) = -\frac{1}{4\pi\epsilon_0}\sum_{I}^{K}\frac{e^2 Z_I}{|\mathbf{r}-\mathbf{R}_I|} + \frac{1}{4\pi\epsilon_0}\sum_{j\neq i}^{N}\int d\mathbf{r}_1\,|\psi_j(\mathbf{r}_1)|^2\frac{e^2}{|\mathbf{r}-\mathbf{r}_1|}. \tag{2.8}$$

2.2.4 Hartree-Fock Approximation

When a many-electron problem is considered, one should be aware that electrons are fermions which are identical particles and have antisymmetric wave functions. When any two arguments are swapped, the wave function changes sign, for example

$$\Psi(\mathbf{X}_1,\mathbf{X}_2,...,\mathbf{X}_i,...,\mathbf{X}_j,...,\mathbf{X}_N) = -\Psi(\mathbf{X}_1,\mathbf{X}_2,...,\mathbf{X}_j,...,\mathbf{X}_i,...,\mathbf{X}_N), \tag{2.9}$$

where $\mathbf{X}_i$ contains r_i representing the electron coordinates and s_i representing the electron-spin projection. In the Hartree approximation this effect is not included, but the Hartree-Fock approximation, developed from Hartree approximation by Fock, has taken into account the spin statistics. By taking the Pauli principle into account, the wave function can be written in form of a Slater determinant, first introduced by Slater [13], as:

$$\Psi(\mathbf{X}_1,\mathbf{X}_2,...,\mathbf{X}_N)=\frac{1}{\sqrt{N!}}\begin{bmatrix}\psi_1(\mathbf{X}_1) & \psi_2(\mathbf{X}_1) & \cdots & \psi_N(\mathbf{X}_1)\\ \psi_1(\mathbf{X}_2) & \psi_2(\mathbf{X}_2) & \cdots & \psi_N(\mathbf{X}_2)\\ \vdots & \vdots & \ddots & \vdots\\ \psi_1(\mathbf{X}_N) & \psi_2(\mathbf{X}_N) & \cdots & \psi_N(\mathbf{X}_N)\end{bmatrix}. \tag{2.10}$$

This wave function is also used for finding the expectation value of the Hamiltonian as:

$$\begin{aligned}\langle\Psi|\hat{H}|\Psi\rangle &= \sum_i^N\int d\mathbf{r}\psi_i^*(\mathbf{r})\left(-\frac{\hbar^2}{2m_e}\nabla^2-\frac{1}{4\pi\epsilon_0}\sum_{I=1}^{K}\frac{Z_Ie^2}{|\mathbf{R_I}-\mathbf{r_i}|}\right)\psi_i(\mathbf{r})\\ &+\frac{1}{2}\frac{1}{4\pi\epsilon_0}\sum_i^N\sum_{j\neq i}^N\int d\mathbf{r}_1d\mathbf{r}_2\frac{e^2|\psi_i(\mathbf{r_1})|^2|\psi_j(\mathbf{r_2})|^2}{|\mathbf{r_1}-\mathbf{r_2}|}\\ &-\frac{1}{2}\frac{1}{4\pi\epsilon_0}\sum_i^N\sum_{j\neq i}^N\int\int d\mathbf{r_1}d\mathbf{r_2}\frac{e^2\left(\psi_i^*(\mathbf{r_1})\psi_j^*(\mathbf{r_2})\psi_i(\mathbf{r_2})\psi_j(\mathbf{r_1})\right)}{|\mathbf{r_1}-\mathbf{r_2}|}.\end{aligned} \tag{2.11}$$

The result of minimizing the expectation value of $\hat{H}$ with respect to the one-electron wavefunctions are the Hartree-Fock equations:

$$\begin{aligned}\epsilon_i\psi_i(\mathbf{r}) &= \left(-\frac{\hbar^2}{2m_e}\nabla^2-\frac{1}{4\pi\epsilon_0}\sum_{I=1}^{K}\frac{Z_Ie^2}{|\mathbf{R_I}-\mathbf{r_i}|}(\mathbf{r})\right)\psi_i(\mathbf{r})\\ &+\frac{1}{4\pi\epsilon_0}\sum_j\int\frac{e^2}{|\mathbf{r}-\mathbf{r}_1|}|\psi_j(\mathbf{r}_1)|^2\psi_i(\mathbf{r})d\mathbf{r}_1\\ &-\frac{1}{4\pi\epsilon_0}\sum_j\int\frac{e^2}{|\mathbf{r}-\mathbf{r}_1|}\psi_j^*(\mathbf{r}_1)\psi_i(\mathbf{r}_1)\psi_j(\mathbf{r})d\mathbf{r}_1.\end{aligned} \tag{2.12}$$

The first two terms are the kinetic energy and the electron-ion interaction potential. The third term is the contribution from the electron potentials which are approximated by the electrostatic interaction with all other electrons and can be written in terms of the electron density $\rho(\mathbf{r})$. The electron density is constructed from the single electron wavefunction:

$$\rho(\mathbf{r})=\sum_{j=1}^{N}|\psi_j(\mathbf{r})|^2, \tag{2.13}$$

where the summation over j thus includes all occupied states. Lastly, the extra term, when compared with Hartree equation, is the exchange term. The effects of the exchange term are that the electrons of like spins tend to avoid each other.

2.2.5 Density Functional Theory

A weakness of the Hartree-Fock equation is that it depends on the assumption that the electron is an independent particle to make the Hamiltonian more simple but in reality it is not totally valid because there is an effect of the correlation between each electron. A better way to solve this problem is called density functional theory, first introduced by Hohenberg and Kohn [14], and later extended by Kohn and Sham [7]. In the density functional theory, the Schrödinger equation depends on the electron density rather than on the individual electron orbitals. In addition, this approach can include correlation effects which are completely neglected in the Hartree-Fock approximation.

The minimal-energy density is given by solving the single particle equation, called the Kohn-Sham equation,

$$\left(-\frac{\hbar^2}{2m}\nabla^2 + V_i^{\text{eff}}(\mathbf{r})\right)\psi_i(\mathbf{r}) = \epsilon_i \psi_i(\mathbf{r}), \tag{2.14}$$

where the effective potential is given by

$$V^{\text{eff}}(\mathbf{r}) = V_{ion} + \frac{e^2}{4\pi\epsilon_0}\int d\mathbf{r}' \frac{\rho(\mathbf{r})}{|\mathbf{r}-\mathbf{r}'|} + V_{xc}(\mathbf{r}), \tag{2.15}$$

where V_{ion} is the external potential due to the ions, which is replaced by pseudopotentials in Chapter 3. $\rho(\mathbf{r})$ is the electron charge density which is calculated from:

$$\rho(\mathbf{r}) = \sum_i^N |\psi_i(\mathbf{r})|^2,$$

and $V_{\text{XC}}(\mathbf{r})$ is exchange-correlation potential. It is clear that $\psi_i(\mathbf{r})$ can be solved only if $V_{\text{eff}}(\mathbf{r})$ is known, yet $V_{\text{eff}}(\mathbf{r})$ is a function of $\psi_i(\mathbf{r})$. Thus these equations must be solved self-consistently. This scheme naturally leads to an iterative procedure, so do Hatree equations and Hartree-Fock equations. The first step of a cycle starts from the approximation of an effective potential ($V_{\text{eff}}(\mathbf{r})$) and then one-particle wave functions ($\psi_i(\mathbf{r})$) are solved to construct the electron charge density. The next step is that the finer effective potential is recalculated and then the new cycle is started by the calculation of the new wave functions. The solution is refined (details given in Sec.3.2) through the self consistent cycles until the system reaches convergence, as illustrated in Fig. 2.1. This method has been used to calculate electronic properties of materials in chapter 3, called self-consistent local density functional pseudopotential plane wave method.

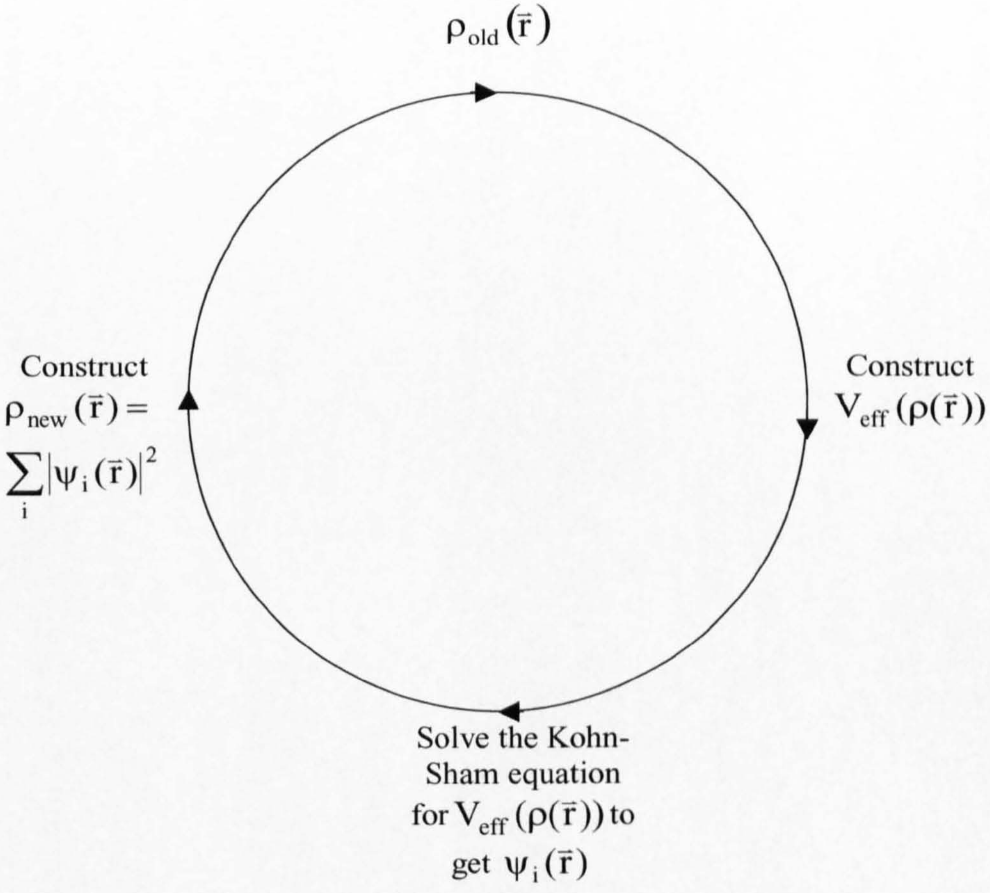

Figure 2.1: The self consistent cycle of the calculation

2.2.6 Pseudopotentials

The concept of pseudopotentials was introduced to study high-lying atomic states. Afterwards, it was proposed that pseudopotentials can be used for calculating the energy levels of alkali metals. The main advantage of using pseudopotentials is that only the valence electrons have to be considered. The core electrons are treated as if they are frozen in an atomic-like configuration. As a result, the valence electrons are considered to move in a weak one-electron potential. To simplify the problem further, model pseudopotenials are used in place of the actual pseudopotential, such as a constant effective potential in the core region, empty core model, model potential due to Heine and Abarenkov, and Lin and Kleinman model potentials. In this work, the pseudopotential form of Srivastava [15] is adopted. The 3D Fourier transforms (for bulk systems) of this pseudopotential is described in the following general form:

$$V_{\mathrm{ps}}(q) = \left(\frac{b_1}{q^2}\right)(\cos(b_2 q) + b_3)\exp(-b_4 q^4), \tag{2.16}$$

where $\mathbf{q}$ is the wave vector and the parameters b_1, b_2, b_3 and b_4 will be discussed in Chapter 3.

2.2.7 Local Density Approximation (LDA)

For an (almost) homogeneous electron gas, the density $\rho(\mathbf{r})$ of which is a slowly varying function of $\mathbf{r}$, the exchange-correlation potential at position $\mathbf{r}$ is assumed to depend only on the electron density at $\mathbf{r}$. In contrast, in a nonhomogeneous system, it depends not only on the density at $\mathbf{r}$ but also on its variation close to $\mathbf{r}$. The explicit local density approximation expression for the exchange-correlation energy is

$$E_{\mathrm{xc}}(\rho(\mathbf{r})) \approx \int \epsilon_{\mathrm{xc}}(\rho(\mathbf{r}))\,\rho(\mathbf{r})\,d\mathbf{r}, \tag{2.17}$$

where $\epsilon_{xc}(\rho(\mathbf{r}))$ is the exchange-correlation energy per electron of the uniform electron gas of density $\rho(\mathbf{r})$. However, the exact form of the exchange-correlation potential can not be readily stated: it is unknown. For the local density approximation, the exchange energy per electron can be written in the form:

$$\epsilon_{\mathrm{ex}}(\rho(\mathbf{r})) = -\frac{3e^2}{4}\left(\frac{3}{\pi}\right)^{\frac{1}{3}}(\rho(\mathbf{r}))^{\frac{1}{3}}, \tag{2.18}$$

and the local density exchange potential is given by:

$$V_{\mathrm{ex}}\left(\rho\left(\mathbf{r}\right)\right)=-e^{2}\left(\frac{3}{\pi}\right)^{\frac{1}{3}}\left(\rho\left(\mathbf{r}\right)\right)^{\frac{1}{3}}. \tag{2.19}$$

In order to take into account the correlation part, in an early attempt Slater [16] has introduced the parameter α, called fudge factor, for the exchange potential. Thus, the exchange-correlation potential for local density approximation was written as:

$$V_{\mathrm{xc}}\left(\rho\left(\mathbf{r}\right)\right)=2\alpha\epsilon_{ex}=-\frac{3\alpha e^{2}}{2}\left(\frac{3}{\pi}\right)^{\frac{1}{3}}\left(\rho\left(\mathbf{r}\right)\right)^{\frac{1}{3}}. \tag{2.20}$$

2.2.8 Total energy

In accordance with the full Kohn-Sham theory and plane wave pseudopotential, the total energy of the system will be derived in reciprocal space explicitly. Finally, the total energy per cell of system is written as,

$$\begin{aligned} E_{\mathrm{total}} &= \frac{1}{N_k}\sum_{k,i}^{N_k} w_{k,i}\epsilon_i+\sum_{\mathbf{G}}^{k}\left[\epsilon_{xc}\left(\mathbf{G}\right)-V_{xc}\left(\mathbf{G}\right)\right]\rho\left(\mathbf{G}\right) && (2.21)\\ &+\left[\gamma_{\mathrm{Ewald}}-\frac{1}{2}4\pi e^{2}\sum_{\mathbf{G}\neq\mathbf{0}}^{k}\frac{\rho\left(\mathbf{G}\right)^{2}}{G^{2}}\right]+\left(\sum_{\kappa}^{k}\alpha_{\kappa}\right)\frac{N_e}{\Omega}. && (2.22)\end{aligned}$$

where the first term on the right hand side is the integration over the first Brillouin zone of the one-electron energy which can be handled by the tetrahedron method explained below, γ_{Ewald} is ion-ion interaction, the next term is the Hartree energy and the last term is a contribution from the non-Coulombic part of the local pseudopotential, with $\frac{N_e}{\Omega}$ representing the average electron density.

In a crystalline solid, the lattice translation symmetry introduces the quantum number of electron quasi-momentum k. The wave function $\psi_n\left(\mathbf{k}\right)$ and the eigenvalue $E_n\left(\mathbf{k}\right)$ depend on the band index n and the electron quasi momentum $\mathbf{k}$. The expectation value $\left\langle\hat{A}\right\rangle$ of an operator $\hat{A}$ is obtained by integrating the matrix elements $A_n\left(\mathbf{k}\right)$ over occupied states in reciprocal space as

$$\left\langle\hat{A}\right\rangle=\frac{1}{V_G}\sum_{n}\int_{V_G}A_n\left(\mathbf{k}\right)f\left(E_n\left(\mathbf{k}\right)\right)d\mathbf{k}, \tag{2.23}$$

where $A_n(\mathbf{k}) = \left\langle \psi_n(\mathbf{k}) \left| \hat{A} \right| \psi_n(\mathbf{k}) \right\rangle$, V_G is the volume of the reciprocal unit cell and $f(E_n(\mathbf{k}))$ is the occupation number or the Fermi distribution function which is equal to 1 for $E < E_F$ and zero for $E > E_F$ at absolute zero temperature. In order to deal with this integration, the widely used tetrahedron method, which was introduced by Blöchl [17], is used. The expectation value $\left\langle \hat{A} \right\rangle$ of an operator $\hat{A}$ is obtained by changing the integral into summation over irreducible $\mathbf{k}$ points:

$$\left\langle \hat{A} \right\rangle = \sum_{j,n} A_n(\mathbf{k}_j)\, w_{n,j}, \tag{2.24}$$

where $w_{n,j}$ are called weights and are given below.

In this method one first defines an equispaced grid in reciprocal space. Then each mesh cell is divided into six tetrahedra as illustrated in Fig. 2.2.

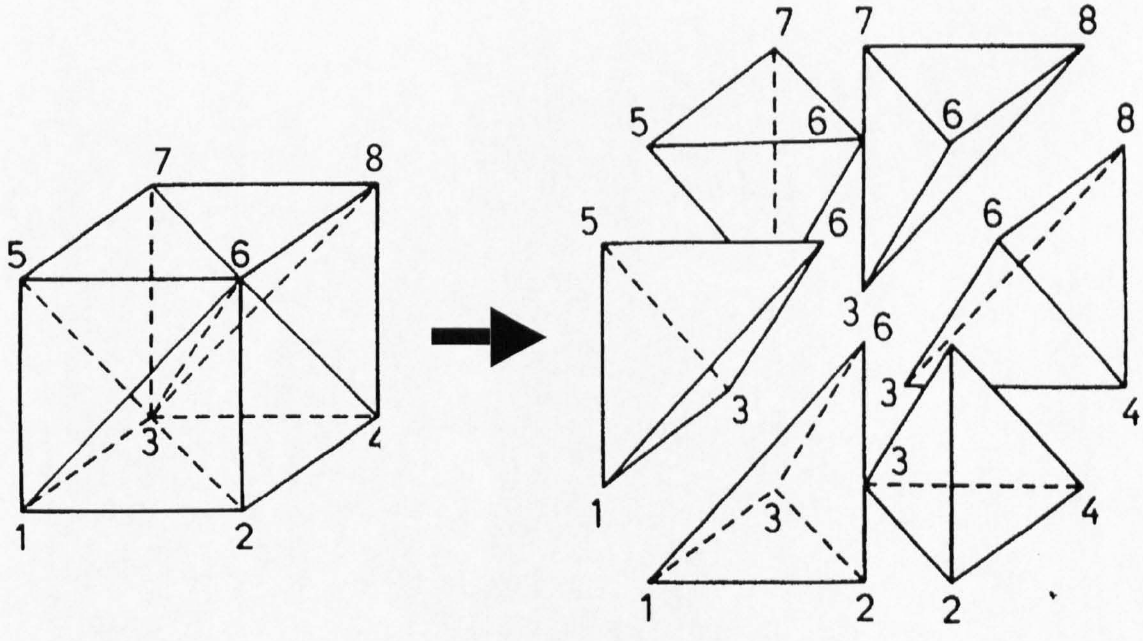

Figure 2.2: Break up of a submesh cell into six tetrahedra

The energy $E(\mathbf{k})$ at the set of grid points is calculated and the variation of the energy between the grid points can be approximated by a linear interpolation scheme using tetrahedra. For this purpose it is convenient to arrange the energies at the corners of the tetrahedrons in ascending order, i.e.

$E_1 < E_2 < E_3 < E_4$. Let $\mathbf{k}_i \, (i = 1, 2, 3, 4)$ be the coordinates of the four corners of the tetrahedron with associated energies E_i. The density of states $D\left(E\right)$ and the number of states $n\left(E\right)$ or the integrated density of states from a given tetrahedron are:

$$D\left(E\right) = 0, \tag{2.25}$$

$$n\left(E\right) = 0. \tag{2.26}$$

For $E < E_1$,

$$D\left(E\right) = \frac{V_T 3 \left(E - E_1\right)^2}{V_G E_{21} E_{31} E_{41}}, \tag{2.27}$$

$$n\left(E\right) = \frac{V_T \left(E - E_1\right)^3}{V_G E_{21} E_{31} E_{41}}, \tag{2.28}$$

for $E_1 < E < E_2$,

$$D\left(E\right) = \frac{V_T}{V_G E_{31} E_{41}} \left[3E_{21} + 6\left(E - E_2\right) - 3\frac{E_{31} + E_{42}}{E_{32} E_{42}} \left(E - E_2\right)^2\right], \tag{2.29}$$

$$n\left(E\right) = \frac{V_T}{V_G E_{31} E_{41}} \left[E_{21}^2 + 3E_{21}\left(E - E_2\right) + 3\left(E - E_2\right)^2 - \frac{E_{31} + E_{42}}{E_{32} E_{42}} \left(E - E_2\right)^3\right], \tag{2.30}$$

for $E_2 < E < E_3$,

$$D\left(E\right) = \frac{V_T}{V_G} \frac{3\left(E_4 - E\right)^2}{E_{41} E_{42} E_{43}}, \tag{2.31}$$

$$n\left(E\right) = \frac{V_T}{V_G} \left(1 - \frac{\left(E_4 - E\right)^3}{E_{41} E_{42} E_{43}}\right), \tag{2.32}$$

for $E_3 < E < E_4$, and

$$D\left(E\right) = 0, \tag{2.33}$$

$$n\left(E\right) = \frac{V_T}{V_G}, \tag{2.34}$$

for $E > E_4$, where E_{ij} is a shorthand notation for $E_i - E_j$ and V_T is the reciprocal space volume of the tetrahedron. Note that the band index n is suppressed. After a number of states is calculated, it is used to determine the Fermi energy level. The weight is also evaluated by using these expressions. For a fully unoccupied tetrahedron, $E_F < E_1$, the contributions vanish, i.e.

$$w_1 = w_2 = w_3 = w_4 = 0. \tag{2.35}$$

For $E_1 < E_F < E_2$,

$$w_1 = C\left[4 - (E_F - E_1)\left(\frac{1}{E_{21}} + \frac{1}{E_{31}} + \frac{1}{E_{41}}\right)\right], \tag{2.36}$$

$$w_2 = C\frac{(E_F - E_1)}{E_{21}}, \tag{2.37}$$

$$w_3 = C\frac{(E_F - E_1)}{E_{31}}, \tag{2.38}$$

$$w_4 = C\frac{(E_F - E_1)}{E_{41}}, \tag{2.39}$$

with

$$C = \frac{V_T}{4V_G}\frac{(E_F - E_1)^3}{E_{21}E_{31}E_{41}}.$$

For $E_2 < E_F < E_3$,

$$w_1 = C_1 + (C_1 + C_2)\frac{(E_3 - E_F)}{E_{31}} + (C_1 + C_2 + C_3)\frac{E_4 - E_F}{E_{41}}, \tag{2.40}$$

$$w_2 = C_1 + C_2 + C_3 + (C_2 + C_3)\frac{E_3 - E_F}{E_{32}} + C_3\frac{E_4 - E_F}{E_{42}}, \tag{2.41}$$

$$w_3 = (C_1 + C_2)\frac{E_F - E_1}{E_{31}} + (C_2 + C_3)\frac{E_F - E_2}{E_{32}}, \tag{2.42}$$

$$w_4 = (C_1 + C_2 + C_3)\frac{E_F - E_1}{E_{41}} + C_3\frac{E_F - E_2}{E_{42}}, \tag{2.43}$$

with

$$C_1 = \frac{V_T}{4V_G}\frac{(E_F - E_1)^2}{E_{31}E_{41}},$$

$$C_2 = \frac{V_T}{4V_G}\frac{(E_F - E_1)(E_F - E_2)(E_3 - E_F)}{E_{31}E_{31}E_{41}},$$

$$C_3 = \frac{V_T}{4V_G}\frac{(E_F - E_2)^2(E_4 - E_F)}{E_{41}E_{32}E_{42}}.$$

For $E_3 < E_F < E_4$,

$$w_1 = \frac{V_T}{4V_G} - C\frac{(E_4 - E_F)}{E_{41}}, \tag{2.44}$$

$$w_2 = \frac{V_T}{4V_G} - C\frac{(E_4 - E_F)}{E_{42}}, \tag{2.45}$$

$$w_3 = \frac{V_T}{4V_G} - C\frac{(E_4 - E_F)}{E_{43}}, \tag{2.46}$$

$$w_4 = \frac{V_T}{4V_G} - C\left[4 - (E_4 - E_F)\left(\frac{1}{E_{43}} + \frac{1}{E_{42}} + \frac{1}{E_{41}}\right)\right], \tag{2.47}$$

with

$$C = \frac{V_T}{4V_G}\frac{(E_4 - E_F)^3}{E_{43}E_{42}E_{41}}.$$

For a fully occupied tetrahedron the contribution for each corner is identical, i.e.

$$w_1 = w_2 = w_3 = w_4 = \frac{V_T}{4V_G}. \tag{2.48}$$

The correction terms of the weight factors have a simple form

$$dw_i = \sum_T \frac{1}{40} D_T(E_F) \sum_{j=1}^{4} (E_j - E_i). \tag{2.49}$$

where $D_T(E_F)$ is the density of states of the T^{th} tetrahedra at the Fermi energy. For a finite temperature case, the step function is replaced by the Fermi distribution and the Fermi energy is determined from the requirement that

$$N = \sum_k \sum_n w(k, \epsilon_n(k) - E_F), \tag{2.50}$$

where the weights are given by

$$w(k, \epsilon_n(k) - E_F) = w(k) \frac{1}{e^{(\epsilon_n(k) - E_F)/k_B T} + 1}. \tag{2.51}$$

The computer code for band structure calculations according to the above algorithm was written in C language.

2.3 Empirical pseudopotential theory

The microscopic pseudopotential [18] in a structure is the superposition of potentials of all the constituent atoms which are situated at every atom site $\mathbf{r}_a$,

$$V_c(\mathbf{r}) = \sum_{\mathbf{r}_a} V_a(\mathbf{r} - \mathbf{r}_a) \tag{2.52}$$

where the summation is done over all the atomic constituents of the basis (atoms type α at basis sites $\mathbf{r}_a$), and all the unit cells. For many semiconductors, which have face-centered cubic crystal structure, shown on the left of Fig.

2.3, the primitive lattice vectors $\mathbf{a}_{1,2,3}$ are:

$$\begin{aligned} \mathbf{a}_1 &= \frac{A_0}{2}(\mathbf{j}+\mathbf{k}), & (2.53)\\ \mathbf{a}_2 &= \frac{A_0}{2}(\mathbf{k}+\mathbf{i}), & (2.54)\\ \mathbf{a}_3 &= \frac{A_0}{2}(\mathbf{i}+\mathbf{j}), & (2.55) \end{aligned}$$

where A_0 is lattice constant of face-centered cubic Bravais lattice. For materials such as Si, Ge and α-Sn, there are two atoms, one at $(\frac{1}{8}, \frac{1}{8}, \frac{1}{8})$ and another at $(-\frac{1}{8}, -\frac{1}{8}, -\frac{1}{8})$ in units of A_0, at each Bravais lattice point. They can be the same atomic type which corresponds to diamond crystal structure (illustrated in Fig. 2.4 (left)) as in Si, Ge and α-Sn, or can be different which corresponds to zincblende crystal structure (illustrated in Fig. 2.4 (right)), as in AlAs and GaAs.

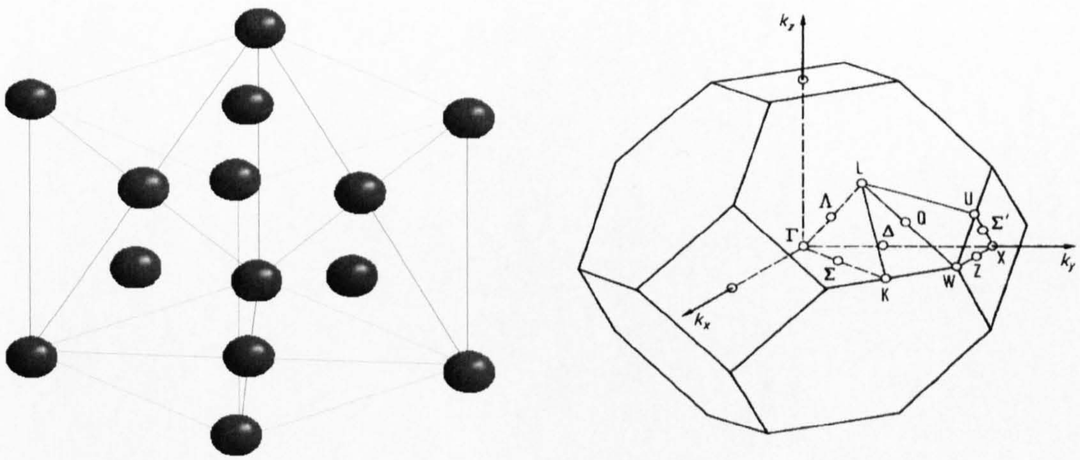

Figure 2.3: The face centered cubic crystal structure (left) and the first Brillouin zone of a face-centered cubic lattice (right).

To solve the Schrödinger equation the wave function is written as a linear combination of the complete orthonomal set of plane waves, i.e. for a state

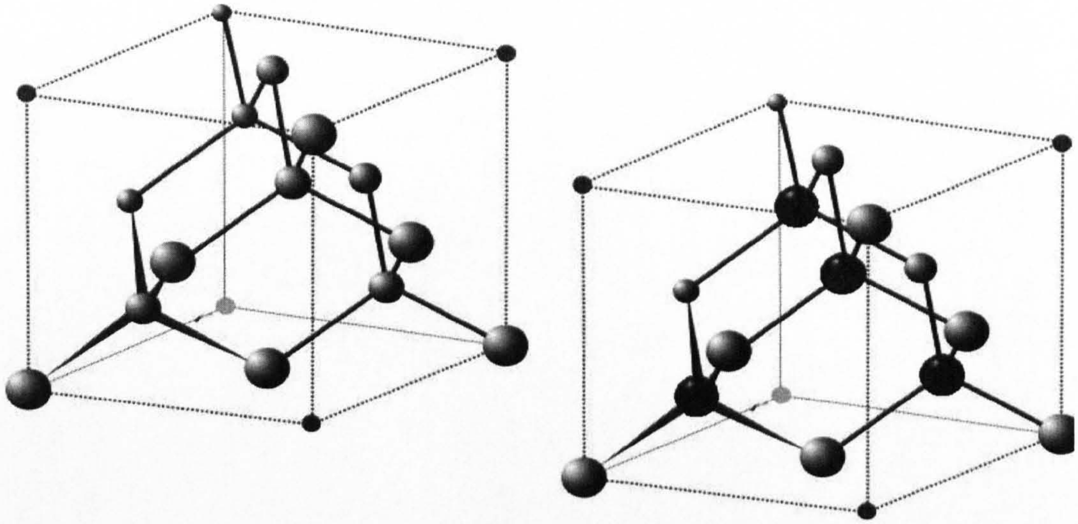

Figure 2.4: Diamond crystal structure (left) and zincblende crystal structure (right).

corresponding to the wave vector $\mathbf{k}$ in the first Brillouin zone:

$$\psi_{n,\mathbf{k}}(\mathbf{r}) = \frac{1}{\sqrt{\Omega}} \sum_{\mathbf{G}} C_{n\mathbf{G}} \exp(i\mathbf{k}\cdot\mathbf{r}) \exp(i\mathbf{G}\cdot\mathbf{r}) \tag{2.56}$$

where $\mathbf{G}$ are linear combinations of the elementary reciprocal lattice vectors $\mathbf{b}$, which satisfy $\mathbf{b}_i \cdot \mathbf{a}_j = 2\pi\delta_{i,j}$ and $\int d\tau e^{i(G-G')\cdot\mathbf{r}} = \Omega\delta_{i,j}$. The primitive reciprocal lattice vectors can be written as follows:

$$\begin{aligned}
\mathbf{b}_1 &= 2\pi\frac{\mathbf{a}_2\times\mathbf{a}_3}{\mathbf{a}_1\cdot(\mathbf{a}_2\times\mathbf{a}_3)} = \frac{2\pi}{A_0}(-\mathbf{i}+\mathbf{j}+\mathbf{k}), && (2.57)\\
\mathbf{b}_2 &= 2\pi\frac{\mathbf{a}_3\times\mathbf{a}_1}{\mathbf{a}_1\cdot(\mathbf{a}_2\times\mathbf{a}_3)} = \frac{2\pi}{A_0}(+\mathbf{i}-\mathbf{j}+\mathbf{k}), && (2.58)\\
\mathbf{b}_3 &= 2\pi\frac{\mathbf{a}_1\times\mathbf{a}_2}{\mathbf{a}_1\cdot(\mathbf{a}_2\times\mathbf{a}_3)} = \frac{2\pi}{A_0}(+\mathbf{i}+\mathbf{j}-\mathbf{k}), && (2.59)
\end{aligned}$$

Therefore, the Hamiltonian matrix element is

$$
\begin{aligned}
H_{\mathbf{G}',\mathbf{G}} &= \frac{1}{\Omega}\int d\tau e^{-i(\mathbf{G}'+\mathbf{k})\cdot\mathbf{r}}\left(-\frac{\hbar}{2m_0}\nabla^2\right)e^{i(\mathbf{G}+\mathbf{k})\cdot\mathbf{r}} && (2.60)\\
&+\frac{1}{\Omega}\int d\tau e^{-i(\mathbf{G}'+\mathbf{k})\cdot\mathbf{r}}V_c(\mathbf{r})\,e^{i(\mathbf{G}+\mathbf{k})\cdot\mathbf{r}}, && (2.61)\\
&= \frac{\hbar^2}{2m_0\Omega}\int d\tau\,|\mathbf{G}+\mathbf{k}|^2\,e^{i(\mathbf{G}-\mathbf{G}')\cdot\mathbf{r}} && (2.62)\\
&+\frac{1}{\Omega}\int d\tau e^{-i(\mathbf{G}'+\mathbf{k})\cdot\mathbf{r}}V_c(\mathbf{r})\,e^{i(\mathbf{G}+\mathbf{k})\cdot\mathbf{r}}, && (2.63)\\
&= \frac{\hbar^2\,|\mathbf{G}_i+\mathbf{k}|^2}{2m_0}\delta_{\mathbf{G}',\mathbf{G}}+V(\mathbf{G}'+\mathbf{k},\mathbf{G}+\mathbf{k}), && (2.64)
\end{aligned}
$$

where $V(\mathbf{G}'+\mathbf{k},\mathbf{G}+\mathbf{k})$ is the potential given by:

$$
V(\mathbf{G}'+\mathbf{k},\mathbf{G}+\mathbf{k}) = \frac{1}{\Omega}\int d\tau e^{-i(\mathbf{G}'+\mathbf{k})\cdot\mathbf{r}}V_c(\mathbf{r})\,e^{i(\mathbf{G}+\mathbf{k})\cdot\mathbf{r}}. \tag{2.65}
$$

After substituting the potential $V_c(\mathbf{r})$ into this equation, one arrives at

$$
\begin{aligned}
V(\mathbf{G}'+\mathbf{k},\mathbf{G}+\mathbf{k}) &= \frac{1}{\Omega}\int d\tau e^{-i(\mathbf{G}'+\mathbf{k})\cdot\mathbf{r}}\sum_{\mathbf{r}_a}V_a(\mathbf{r}-\mathbf{r}_a)e^{i(\mathbf{G}+\mathbf{k})\cdot\mathbf{r}} && (2.66)\\
&= \frac{1}{\Omega}\sum_{\mathbf{r}_a}\int d\tau V_a(\mathbf{r}-\mathbf{r}_a)e^{i(\mathbf{G}-\mathbf{G}')\cdot\mathbf{r}}. && (2.67)
\end{aligned}
$$

After a mathematically convenient, $\mathbf{r}\Rightarrow\mathbf{r}+\mathbf{r}_a$ transformation V becomes

$$
\begin{aligned}
V(\mathbf{G}'+\mathbf{k},\mathbf{G}+\mathbf{k}) &= \frac{1}{\Omega}\sum_{\mathbf{r}_a}\int d\tau V_a(\mathbf{r})e^{i(\mathbf{G}-\mathbf{G}')\cdot(\mathbf{r}-\mathbf{r}_a)} && (2.68)\\
&= \frac{1}{\Omega}\sum_{\mathbf{r}_a}e^{i(\mathbf{G}-\mathbf{G}')\cdot(\mathbf{r}_a)}\int d\tau V_a(\mathbf{r})e^{i(\mathbf{G}-\mathbf{G}')\cdot(\mathbf{r})} && (2.69)
\end{aligned}
$$

where the term $\sum_{\mathbf{r}_a}e^{i(\mathbf{G}-\mathbf{G}')\cdot(\mathbf{r}_a)}$ is called the geometrical structure factor S. The formfactor of atom type α at basis sites $\mathbf{r}_a$ is defined as the Fourier transform of the atomic potential and also is known as pseudopotential form factor. Ω denotes the scaling volume (that of the unit cell) and $q=|\mathbf{q}|=|\mathbf{k}+\mathbf{G}|$. For diamond and zincblende crystal structures, which have two basis atoms at $\frac{A_0}{8}(\mathbf{i}+\mathbf{j}+\mathbf{k})$ and $\frac{A_0}{8}(-\mathbf{i}-\mathbf{j}-\mathbf{k})$, the geometrical structure factor S is given as

$$
S=\sum_{\mathbf{r}_a}e^{i(\mathbf{G}-\mathbf{G}')\cdot\mathbf{r}_a} \tag{2.70}
$$

where the summation goes over all the basis atom sites **T**. Taking spherical atomic the potential formfactors actually depend only on the modulus of **q**. The number of vectors (plane waves) to actually work with is chosen according to the energy cutoff criteria. In selecting the **q** vectors to be included in the basis set, a **q** vector is included in the basis set if

$$E(\mathbf{K}) = E(K) = \frac{\hbar^2 K^2}{2m_0} \leq E_{\text{cutoff}} \tag{2.71}$$

is satisfied, where m_0 is the free electron mass, $K = |\mathbf{K}| = |\mathbf{k} + \mathbf{G}|$. For bulk band structure calculations the local part of the pseudopotential is more conveniently described by a continuous formfunction of the wave vector, $V(q)$, for each of the atomic constituents of the unit cell. The most frequently used types of formfunctions are the classical Falicov form [19]:

$$V(q) = \frac{a_1(q^2 - a_2)}{1 + \exp[a_3(q^2 - a_4)]} \tag{2.72}$$

the parameters for which are available in the literature for a wide range of atomic species, or the modified Falicov form, after Friedel et al. in Ref. [20], also used by Fischetti and Laux in Ref. [21], parameters available for Si and Ge, only which is adopted to use in band structure calculation in chapter 4:

$$V(q) = \frac{a_1(q^2 - a_2)}{1 + \exp[a_3(q^2 - a_4)]} \cdot \frac{1}{2}\left[\tanh\left(\frac{a_5 - q^2}{a_6}\right) + 1\right] \tag{2.73}$$

or the Zunger form [22],

$$V(g) = \frac{a_1(q^2 - a_2)}{a_3 \exp(a_4 q^2) - 1}, \tag{2.74}$$

where the parameters for which are now available for Si and most of III-V s.

2.3.1 Nonlocal potential

The accuracy of the empirical pseudopotential calculations is often improved by introducing a nonlocal potential [3], along with the local one. Like nonlocal density functional, in the plane wave representation of the wave function the nonlocal potential depends on the wave vectors of the two basis states separately, not just on the difference of their wave vectors. The nonlocal potential matrix element relating the basis states with the reciprocal lattice vectors $\mathbf{G}$ and $\mathbf{G}'$ is given by

$$V_{NL}^{\ell}(\mathbf{K},\mathbf{K}') = \frac{4\pi}{\Omega} A_\ell \cdot (2\ell+1) P_\ell(\cos\theta) \cdot F_\ell(K,K') \cdot S(\mathbf{K}-\mathbf{K}') \qquad (2.75)$$

where $\mathbf{K} = \mathbf{G} + \mathbf{k}$ and $\mathbf{K}' = \mathbf{G}' + \mathbf{k}$, and $\mathbf{k}$ is the wave vector in the first Brillouin zone, Ω is the scaling volume, ℓ the azimuthal quantum number, $\cos\theta = \mathbf{K} \cdot \mathbf{K}'/(K \cdot K')$, $P_\ell(.)$ is the Legendre polynomial of order ℓ, the potential strength A_ℓ is the depth of the nonlocal square well, characterizing the particular atomic type, $S(\mathbf{K}-\mathbf{K}')$ is the structure factor determined by the position of the atom, Eq. (2.70), and

$$F_\ell(K,K') = \begin{cases} \frac{R_s^3}{2}\left[j_\ell^2(K R_s) - j_{\ell-1}(K R_s) j_{\ell+1}(K R_s)\right], & K = K' \\ \frac{R_s^2}{K^2-K'^2}\begin{bmatrix} K\, j_{\ell+1}(K R_s) j_\ell(K' R_s) \\ -K'\, j_{\ell+1}(K' R_s) j_\ell(K R_s) \end{bmatrix}, & K \neq K' \end{cases} \qquad (2.76)$$

where R_s is the radius of the nonlocal square well (characterizing the particular atomic type), and $j_\ell(.)$ the spherical Bessel function of order ℓ. Various atoms are usually characterized by either the $\ell = 0$ (s type) or the $\ell = 2$ (d type) nonlocality (almost never both).

In the case of $\ell = 0$ nonlocality the strength A_ℓ is usually made energy-dependent, according to either of the two expressions, related by units used:

$$A_0 = \alpha + \beta \cdot \left[(E(K) \cdot E(K'))^{1/2} - E_F\right], \quad \text{or} \quad A_0 = \alpha + \beta_0 \cdot [K\, K' - k_F] \qquad (2.77)$$

where E_F (or k_F) denote the Fermi energy (or the equivalent wave vector), and the parameters α and β (or β_0) characterize the particular atomic type.

In the case of $\ell = 2$ nonlocality the screening is occasionally introduced, i.e. defining the screening function

$$w(K) = \exp\left[-\alpha\left(\frac{K-\chi}{2k_F}\right)^2\right] \qquad (2.78)$$

where α and χ are the screening parameters characterizing the particular atomic type, the matrix elements, Eq.(2.75), are rescaled as

$$V_{NL}^{\ell}(\mathbf{K},\mathbf{K}') \rightarrow w(K) \cdot V_{NL}^{\ell}(\mathbf{K},\mathbf{K}') \cdot w(K') \qquad (2.79)$$

2.3.2 Spin-orbit coupling

The spin-orbit (S.O.) interaction Hamiltonian, in the plane wave basis, is [3]

$$H_{so} = -i\lambda\sigma \cdot (\mathbf{K} \times \mathbf{K}') \cdot S(\mathbf{K} - \mathbf{K}') \tag{2.80}$$

where λ is the spin-orbit coupling constant, characterizing the particular atomic type, and σ are the Pauli matrices:

$$\sigma_x = \frac{1}{2}\begin{bmatrix} 0 & 1 \\ 1 & 0 \end{bmatrix}, \quad \sigma_y = \frac{1}{2}\begin{bmatrix} 0 & -i \\ i & 0 \end{bmatrix}, \quad \sigma_z = \frac{1}{2}\begin{bmatrix} 1 & 0 \\ 0 & -1 \end{bmatrix} \tag{2.81}$$

As in Ref. [23] screening of the spin-orbit coupling is introduced. Analytic expressions for the screening functions may be obtained when using the Slater-type orbitals. These expressions read (Z. Ikonić, unpublished):

$$\begin{aligned} f_1(K) &= \frac{1}{(1+\chi^2)^2}, \quad f_2(K) = \frac{1}{(1+\chi^2)^3}, \quad f_3(K) = \frac{5-\chi^2}{5(1+\chi^2)^4}, \\ f_4(K) &= \frac{5-3\chi^2}{5(1+\chi^2)^5}, \quad f_5(K) = \frac{35-42\chi^2+3\chi^4}{35(1+\chi^2)^6} \end{aligned} \tag{2.82}$$

where the subscript denotes the row in the periodic table that the particular atomic type belongs to, and where $\chi = K \cdot \xi$, with ξ denoting the screening length (being ~0.1 Å for Si and Ge). The s.o. interaction matrix elements are then rescaled as:

$$H_{so}(K, K') \rightarrow f(K) \cdot H_{so}(K, K') \cdot f(K') \tag{2.83}$$

2.4 k · p method

In contrast to the previously described methods, the k·p method [24] is based upon perturbation theory. In this method, the energy is calculated near a band maximum or minimum by considering the wavenumber (measured from the extremum) as a perturbation. In the absence of strain, one describes the Hamiltonian of an electron in a semiconductor as

$$\hat{H} = \frac{\hat{\mathbf{p}}^2}{2m_0} + V_0(\mathbf{r}) + \hat{H}_{so}, \tag{2.84}$$

where $\hat{\mathbf{p}}$ is the momentum operator, in this section $V_0(\mathbf{r})$ is the periodic crystal potential (including nuclei, core electrons and self-consistent potential of valence electrons), and $\hat{H}_{\text{so}}$ is the spin-orbit interaction arising from relativistic corrections to Schrödinger equation in real space form given by

$$\hat{H}_{\text{so}} = \frac{\hbar}{4m_0^2c^2}\left[\nabla V_0(\mathbf{r}) \times \hat{\mathbf{p}}\right]\cdot\sigma, \tag{2.85}$$

where σ is a vector of Pauli matrices

$$\sigma_x = \begin{bmatrix} 0 & 1 \\ 1 & 0 \end{bmatrix}, \sigma_y = \begin{bmatrix} 0 & -i \\ i & 0 \end{bmatrix}, \sigma_z = \begin{bmatrix} 1 & 0 \\ 0 & -1 \end{bmatrix}. \tag{2.86}$$

Considering a periodic lattice in space, Bloch theorem states that the solution of the Schrodinger equation for the periodic lattice is of the form

$$\Psi(\mathbf{r}) = u_{n\mathbf{k}}(\mathbf{r})e^{i\mathbf{k}\cdot\mathbf{r}}, \tag{2.87}$$

where $u_{n\mathbf{k}}(\mathbf{r})$ is a periodic function, called Bloch function, at band n, wave vector from the first Brillouin zone $\mathbf{k}$. By substituting (2.87) into the Schrödinger equation,

$$\hat{H}\Psi = E\Psi, \tag{2.88}$$

the equation is written as,

$$\begin{aligned} E_{n\mathbf{k}}u_{n\mathbf{k}}(\mathbf{r}) &= (\frac{\hat{\mathbf{p}}^2}{2m_0} + V_0(\mathbf{r}) + \frac{\hbar^2k^2}{2m_0} + \hbar\frac{\mathbf{k}\cdot\hat{\mathbf{p}}}{m_0} + \frac{\hbar}{4m_0^2c^2}\left[\nabla V_0(\mathbf{r}) \times \hat{\mathbf{p}}\right]\cdot\sigma \\ &+\frac{\hbar^2}{4m_0^2c^2}\left[\nabla V_0(\mathbf{r}) \times \mathbf{k}\right]\cdot\sigma)u_{n\mathbf{k}}(\mathbf{r}) \end{aligned} \tag{2.89}$$

After neglecting the last term in this equation because the term $\hbar\mathbf{k}$ ($\mathbf{k}$ around Γ-point) is much smaller compared with matrix elements of $\hat{\mathbf{p}}$ and expressing the solution of (2.89), $u_{n\mathbf{k}}(\mathbf{r})$, as a linear combination of orthonormal basis states, $u_{n0}(\mathbf{r})$,

$$u_{n\mathbf{k}}(\mathbf{r}) = \sum_n c_{n\mathbf{k}}u_{n0}(\mathbf{r}), \tag{2.90}$$

where $u_{n0}(\mathbf{r})$ are the solutions at the Γ point of the eigenvalue problem of a Hermitian operator with periodic boundary conditions and spin-orbit interaction not included,

$$\hat{H}_0 u_{n0}(\mathbf{r}) = \left(\frac{\hat{\mathbf{p}}^2}{2m_0} + V_0(\mathbf{r})\right) u_{n0}(\mathbf{r}) = E_{n0} u_{n0}(\mathbf{r}). \tag{2.91}$$

One has arrived at the eigenvalue problem of the Hamiltonian matrix whose elements are given as,

$$h_{mn} = \langle u_{m0}| \left(\frac{\hat{\mathbf{p}}^2}{2m_0} + V_0(\mathbf{r}) + \frac{\hbar^2 k^2}{2m_0} + \hbar\frac{\mathbf{k}\cdot\hat{\mathbf{p}}}{m_0} + \hat{H}_{\mathrm{so}}\right) |u_{n0}\rangle\,. \tag{2.92}$$

Using (2.91) and the orthonormality condition, the Hamiltonian matrix is finally expressed as,

$$h_{mn} = \left(E_{n0} + \frac{\hbar^2 k^2}{2m_0}\right)\delta_{m,n} + \frac{\hbar}{m_0}\langle u_{m0}|\,\mathbf{k}\cdot\hat{\mathbf{p}}\,|u_{n0}\rangle + \langle u_{m0}|\,\hat{H}_{\mathrm{so}}\,|u_{n0}\rangle\,. \tag{2.93}$$

This method, therefore, is called the $\mathbf{k}\cdot\mathbf{p}$ method, as shown in the third term of the Hamiltonian. It was first applied to the valence band (6-band Hamiltonian) [25, 26] and later on the conduction band was added (8-band Hamiltonian) [27]. The explicit forms of 8-band Hamiltonians in semiconductors with zincblende and diamond structure, used in this work, will be explained in the next section.

2.4.1 The 8-band $\mathbf{k}\cdot\mathbf{p}$ Hamiltonian for semiconductors with zincblende and diamond crystal symmetry

The explicit form of the 8-band $\mathbf{k}\cdot\mathbf{p}$ Hamiltonian is built to include the three highest states in the valence band and the lowest states in the conduction band. Since semiconductors have sp^3 hybridization tetrahedral bonds, an interaction between valence electrons in s-and p-type orbitals in the individual atoms after forming a semiconductor crystal, the suitable basis consisting of spin up and down states, denoted as

$$\{u_1,\ldots,u_8\} = \{|S\uparrow\rangle, |X\uparrow\rangle, |Y\uparrow\rangle, |Z\uparrow\rangle, |S\downarrow\rangle, |X\downarrow\rangle, |Y\downarrow\rangle, |Z\downarrow\rangle\}, \tag{2.94}$$

is chosen in expansion (2.90). One can see the analogy of these states to s and p_{x-z} orbitals of a spherically symmetric system (such as for example a hydrogen atom). Instead of S, X, Y, Z, one has instead choose to work in the basis of eigenstates of the total angular momentum operator $|JJ_z\rangle$ because it can diagonalize the Hamiltonian at $\mathbf{k} = 0$ and be expressed in the previous basis as [28]:

$$\begin{aligned}
|1\rangle &= |\frac{1}{2}, -\frac{1}{2}\rangle = |S \downarrow\rangle, \\
|2\rangle &= |\frac{1}{2}, \frac{1}{2}\rangle = |S \uparrow\rangle, \\
|3\rangle &= |\frac{3}{2}, \frac{1}{2}\rangle = -\frac{i}{\sqrt{6}}|(X + iY) \downarrow\rangle + i\sqrt{\frac{2}{3}}|Z \uparrow\rangle, \\
|4\rangle &= |\frac{3}{2}, \frac{3}{2}\rangle = \frac{i}{\sqrt{2}}|(X + iY) \uparrow\rangle, \\
|5\rangle &= |\frac{3}{2}, -\frac{3}{2}\rangle = -\frac{i}{\sqrt{2}}|(X - iY) \downarrow\rangle, \qquad (2.95) \\
|6\rangle &= |\frac{3}{2}, -\frac{1}{2}\rangle = \frac{i}{\sqrt{6}}|(X - iY) \uparrow\rangle + i\sqrt{\frac{2}{3}}|Z \downarrow\rangle, \\
|7\rangle &= |\frac{1}{2}, -\frac{1}{2}\rangle = -\frac{i}{\sqrt{3}}|(X - iY) \uparrow\rangle + \frac{i}{\sqrt{3}}|Z \downarrow\rangle, \\
|8\rangle &= |\frac{1}{2}, \frac{1}{2}\rangle = -\frac{i}{\sqrt{3}}|(X + iY) \downarrow\rangle - \frac{i}{\sqrt{3}}|Z \uparrow\rangle.
\end{aligned}$$

The Bloch functions labelled by '1' and '2' correspond to electron states of spin down and spin up, those labelled by '3' and '6' to light-hole states, '4' and '5' to heavy-hole states and '7' and '8' to split-off band states. In this basis, the Hamiltonian acquires the form:

$$\hat{H}_k = \qquad (2.96)$$

$$\begin{bmatrix}
A & 0 & V^+ & 0 & \sqrt{3}V & -\sqrt{2}U & -U & \sqrt{2}V^+ \\
0 & A & -\sqrt{2}U & -\sqrt{3}V^+ & 0 & -V & \sqrt{2}V & U \\
V & -\sqrt{2}U & -P + Q & -S^+ & R & 0 & \sqrt{\frac{3}{2}}S & -\sqrt{2}Q \\
0 & -\sqrt{3}V & -S & -P - Q & 0 & R & -\sqrt{2}R & \frac{1}{\sqrt{2}}S \\
\sqrt{3}V^+ & 0 & R^+ & 0 & -P - Q & S^+ & \frac{1}{\sqrt{2}}S^+ & \sqrt{2}R^+ \\
-\sqrt{2}U & -V^+ & 0 & R^+ & S & -P + Q & \sqrt{2}Q & \sqrt{\frac{3}{2}}S^+ \\
-U & \sqrt{2}V^+ & \sqrt{\frac{3}{2}}S^+ & -\sqrt{2}R^+ & \frac{1}{\sqrt{2}}S & \sqrt{2}Q & -P - \Delta & 0 \\
\sqrt{2}V & U & -\sqrt{2}Q & \frac{1}{\sqrt{2}}S^+ & \sqrt{2}R & \sqrt{\frac{3}{2}}S & 0 & -P - \Delta
\end{bmatrix},$$

where

$$\begin{aligned}
A &= E_C + \frac{\hbar^2}{m_0}A'^2 + \frac{\hbar^2 k^2}{2m_0}, \\
U &= \frac{1}{\sqrt{3}}P_0 k_z, \\
V &= \frac{1}{\sqrt{6}}P_0(k_x - ik_y), \\
P &= -E_V + \gamma_1 \frac{\hbar^2 k^2}{2m_0}, \\
Q &= \gamma_2 \frac{\hbar^2}{2m_0}\left(k_x^2 + k_y^2 - 2k_z^2\right), \\
R &= -\frac{\sqrt{3}}{2}\frac{\hbar^2}{m_0}\left[\gamma_2\left(k_x^2 - k_y^2\right) - 2i\gamma_3 k_x k_y\right], \\
S &= \sqrt{3}\gamma_3 \frac{\hbar^2}{m_0} k_z(k_x - ik_y),
\end{aligned}$$

when $E_g = E_C - E_V$ is the energy gap and γ_1, γ_2, γ_3 are Luttinger parameters of the 8-band model, expressed in terms of the more experimentally accessible parameters of the 6-band model as

$$\begin{aligned}
\gamma_1 &= \gamma_1^L - \frac{E_P}{3E_g + \Delta}, \\
\gamma_2 &= \gamma_2^L - \frac{1}{2}\frac{E_P}{3E_g + \Delta}, \\
\gamma_3 &= \gamma_3^L - \frac{1}{2}\frac{E_P}{3E_g + \Delta}.
\end{aligned}$$

Δ denotes the spin-orbit splitting, and P_0 is the interband matrix element of the velocity operator [29] usually reported in energy units as $E_P = \frac{2m_0}{\hbar^2}P_0^2$. After considering all bands other than the conduction band as remote bands and applying Löwdin's perturbation theory, the parameter A' can be related to conduction band effective mass m^* as

$$\frac{\hbar^2}{2m_0}(1 + A') = \frac{\hbar^2}{2m^*} - \frac{P_0^2}{E_g + \frac{1}{3}\Delta}. \qquad (2.97)$$

2.4.2 The effect of strain in diamond crystals

The aim of this section is to explain how the influence of strain can be taken into account in the **k** · **p** model, approach of Ref. [28], because it has a strong effect on the electronic structure of semiconductors, such as changing the potential in semiconductors, modifying the bandstructure and relocating the atoms from their original positions (the last of these effects does not appear explicitly in the $\mathbf{k}\cdot\mathbf{p}$ method, but is taken within the empirical pseudopotential calculations in this thesis). Let the component of the displacement vector of a point in the semiconductor in the direction i be u_i. The strain tensor components are then defined as:

$$e_{ij} = \frac{1}{2}\left(\frac{\partial u_i}{\partial x_j} + \frac{\partial u_j}{\partial x_i}\right), \tag{2.98}$$

where the indices i, j represent the x, y, z. The Hamiltonian contributed by the strain in the basis (2.95) is given as [28]

$$\hat{H}_s = \tag{2.99}$$

$$\begin{bmatrix} a_c e & 0 & -v^+ & 0 & -\sqrt{3}v & \sqrt{2}u & u & -\sqrt{2}v^+ \\ 0 & a_c e & \sqrt{2}u & \sqrt{3}v^+ & 0 & v & -\sqrt{2}v & -u \\ -v & \sqrt{2}u & -p+q & -s^+ & r & 0 & \sqrt{\frac{3}{2}}s & -\sqrt{2}q \\ 0 & \sqrt{3}v & -s & -p-q & 0 & r & -\sqrt{2}r & \frac{1}{\sqrt{2}}s \\ -\sqrt{3}v^+ & 0 & r^+ & 0 & -p-q & s^+ & \frac{1}{\sqrt{2}}s^+ & \sqrt{2}r^+ \\ \sqrt{2}u & v^+ & 0 & r^+ & s & -p+q & \sqrt{2}q & \sqrt{\frac{3}{2}}s^+ \\ u & -\sqrt{2}v^+ & \sqrt{\frac{3}{2}}s^+ & -\sqrt{2}r^+ & \frac{1}{\sqrt{2}}s & \sqrt{2}q & -p & 0 \\ -\sqrt{2}v & -u & -\sqrt{2}q & \frac{1}{\sqrt{2}}s^+ & \sqrt{2}r & \sqrt{\frac{3}{2}}s & 0 & -p \end{bmatrix},$$

where

$$\begin{aligned} e &= e_{11} + e_{22} + e_{33}, \\ p &= a_v e, \\ q &= b\left[e_{33} - \frac{1}{2}(e_{11} + e_{22})\right], \\ r &= \frac{\sqrt{3}}{2}b(e_{11} - e_{22}) - ide_{12}, \\ s &= -d(e_{13} - ie_{23}), \\ u &= \frac{1}{\sqrt{3}}P_0\sum_{j=1}^{3} e_{3j}k_j, \\ v &= \frac{1}{\sqrt{6}}P_0\sum_{j=1}^{3}(e_{1j} - ie_{2j})k_j, \end{aligned}$$

where a_c and a_v are the conduction and valence band hydrostatic deformation potentials, respectively, b and d are the uniaxial and shear deformation potentials.

2.4.3 The solution of 8-band k · p method for bulk semiconductors

The aims of this section is to use the 8-band **k** · **p** method to calculate the electronic band structure and electrical properties of bulk semiconductor, which is periodic, by starting from solving equations:

$$\left(\hat{H}_k(\mathbf{k}) + \hat{H}_s(\mathbf{k})\right) F(\mathbf{k}) = E(\mathbf{k}) F(\mathbf{k})$$

$$\left\{ \begin{bmatrix} A & 0 & V^{+} & 0 & \sqrt{3}V & -\sqrt{2}U & -U & \sqrt{2}V^{+} \\ 0 & A & -\sqrt{2}U & -\sqrt{3}V^{+} & 0 & -V & \sqrt{2}V & U \\ V & -\sqrt{2}U & -P+Q & -S^{+} & R & 0 & \sqrt{\frac{3}{2}}S & -\sqrt{2}Q \\ 0 & -\sqrt{3}V & -S & -P-Q & 0 & R & -\sqrt{2}R & \frac{1}{\sqrt{2}}S \\ \sqrt{3}V^{+} & 0 & R^{+} & 0 & -P-Q & S^{+} & \frac{1}{\sqrt{2}}S^{+} & \sqrt{2}R^{+} \\ -\sqrt{2}U & -V^{+} & 0 & R^{+} & S & -P+Q & \sqrt{2}Q & \sqrt{\frac{3}{2}}S^{+} \\ -U & \sqrt{2}V^{+} & \sqrt{\frac{3}{2}}S^{+} & -\sqrt{2}R^{+} & \frac{1}{\sqrt{2}}S & \sqrt{2}Q & -P-\Delta & 0 \\ \sqrt{2}V & U & -\sqrt{2}Q & \frac{1}{\sqrt{2}}S^{+} & \sqrt{2}R & \sqrt{\frac{3}{2}}S & 0 & -P-\Delta \end{bmatrix} + \begin{bmatrix} a_c e & 0 & -v^{+} & 0 & -\sqrt{3}v & \sqrt{2}u & u & -\sqrt{2}v^{+} \\ 0 & a_c e & \sqrt{2}u & \sqrt{3}v^{+} & 0 & v & -\sqrt{2}v & -u \\ -v & \sqrt{2}u & -p+q & -s^{+} & r & 0 & \sqrt{\frac{3}{2}}s & -\sqrt{2}q \\ 0 & \sqrt{3}v & -s & -p-q & 0 & r & -\sqrt{2}r & \frac{1}{\sqrt{2}}s \\ -\sqrt{3}v^{+} & 0 & r^{+} & 0 & -p-q & s^{+} & \frac{1}{\sqrt{2}}s^{+} & \sqrt{2}r^{+} \\ \sqrt{2}u & v^{+} & 0 & r^{+} & s & -p+q & \sqrt{2}q & \sqrt{\frac{3}{2}}s^{+} \\ u & -\sqrt{2}v^{+} & \sqrt{\frac{3}{2}}s^{+} & -\sqrt{2}r^{+} & \frac{1}{\sqrt{2}}s & \sqrt{2}q & -p & 0 \\ -\sqrt{2}v & -u & -\sqrt{2}q & \frac{1}{\sqrt{2}}s^{+} & \sqrt{2}r & \sqrt{\frac{3}{2}}s & 0 & -p \end{bmatrix} \right\} \begin{bmatrix} F_1(\mathbf{k}) \\ F_2(\mathbf{k}) \\ F_3(\mathbf{k}) \\ F_4(\mathbf{k}) \\ F_5(\mathbf{k}) \\ F_6(\mathbf{k}) \\ F_7(\mathbf{k}) \\ F_8(\mathbf{k}) \end{bmatrix} = E(\mathbf{k}) \begin{bmatrix} F_1(\mathbf{k}) \\ F_2(\mathbf{k}) \\ F_3(\mathbf{k}) \\ F_4(\mathbf{k}) \\ F_5(\mathbf{k}) \\ F_6(\mathbf{k}) \\ F_7(\mathbf{k}) \\ F_8(\mathbf{k}) \end{bmatrix} \tag{2.100}$$

The Hamiltonian matrix is a function of the wavevector **k**. These equations are solved by diagonalizing the Hamiltonian matrix. The result of doing so is that one will get 8 eigenenergies and 8 coefficients of the basis, in Eq.(2.96), of the wavefunctions. These wavefunctions correspond to 2 wavefunctions in the conduction bands and 6 the in valence bands:

$$E_{n\mathbf{k}} \Leftrightarrow \begin{bmatrix} F_{n1}(\mathbf{k}) \\ F_{n2}(\mathbf{k}) \\ F_{n3}(\mathbf{k}) \\ F_{n4}(\mathbf{k}) \\ F_{n5}(\mathbf{k}) \\ F_{n6}(\mathbf{k}) \\ F_{n7}(\mathbf{k}) \\ F_{n8}(\mathbf{k}) \end{bmatrix} \tag{2.101}$$

Then, the band nth wavefunction at wavevector **k** is expressed as:

$$\Psi_{n\mathbf{k}}(\mathbf{r}) = \left(\sum_{j=1}^{8} F_{n\mathbf{k}j} \left| \right\rangle_j \right) e^{i\mathbf{k}\cdot\mathbf{r}}$$

where $\left| \right\rangle$ is the basis function in Eq.(2.96).

2.4.4 The solution of 8-band k · p method for heterostructure semiconductors

Similarly, the aims of this section is to modify the 8-band **k** · **p** method to be able to calculate the electronic band structure and electrical properties of heterostructure semiconductors, such as quantum wells, wires and dots, which do not have periodicity. According to this reason, the idea of an envelope function has been introduced. The whole heterostructure will be treated as a large periodic system.

- **Quantum dots**. The energies and wave functions are computed by replacing the wavevector **k** with derivatives with respect to spatial coordinates, i.e. $k_z \Rightarrow -\frac{\partial}{\partial z}$, $k_y \Rightarrow -\frac{\partial}{\partial y}$ and $k_x \Rightarrow -\frac{\partial}{\partial x}$, the terms of the type

$\gamma k_z^2 \Rightarrow k_z\gamma k_z$, $\gamma k_y^2 \Rightarrow k_y\gamma k_y$ and $\gamma k_x^2 \Rightarrow k_x\gamma k_x$. The diagonal elements of the Hamiltonian are amended with the potential, including the valence band offset, external electric field and self-consistent space-charge electrostatic potential. The coefficients of the basis then have turned into envelope functions:

$$E_{n\mathbf{k}} \Leftrightarrow \begin{bmatrix} F_{n1}(\mathbf{r}) \\ F_{n2}(\mathbf{r}) \\ F_{n3}(\mathbf{r}) \\ F_{n4}(\mathbf{r}) \\ F_{n5}(\mathbf{r}) \\ F_{n6}(\mathbf{r}) \\ F_{n7}(\mathbf{r}) \\ F_{n8}(\mathbf{r}) \end{bmatrix} \qquad (2.102)$$

Finally the Eq.(2.100), turned to be a system of differential equations, have to be solved. Then, the band nth wavefunction at wavevector **k** is expressed as:

$$\Psi_{n\mathbf{k}}(\mathbf{r}) = \left(\sum_{j=1}^{8} F_{n\mathbf{k}j}(\mathbf{r})\,|\rangle_j\right)$$

where $|\rangle$ is basis function in Eq.(2.96).

- **Quantum wells.** Similarly to quantum dots, the wavevector **k** in Eq.(2.100) will be replaced with derivatives with respect to spatial coordinate, i.e. $k_z \Rightarrow -\frac{\partial}{\partial z}$, but k_x, k_y will not be changed. The envelope functions are only functions of z:

$$\begin{bmatrix} \cdots & & \\ k_z \Rightarrow -\frac{\partial}{\partial z} & & \\ & k_x, k_y & \\ & & \cdots \end{bmatrix} \begin{bmatrix} F_1\left(z,\mathbf{k}_{xy}\right) \\ F_2\left(z,\mathbf{k}_{xy}\right) \\ F_3\left(z,\mathbf{k}_{xy}\right) \\ F_4\left(z,\mathbf{k}_{xy}\right) \\ F_5\left(z,\mathbf{k}_{xy}\right) \\ F_6\left(z,\mathbf{k}_{xy}\right) \\ F_7\left(z,\mathbf{k}_{xy}\right) \\ F_8\left(z,\mathbf{k}_{xy}\right) \end{bmatrix} = E\left(\mathbf{k}_{xy}\right) \begin{bmatrix} F_1\left(z,\mathbf{k}_{xy}\right) \\ F_2\left(z,\mathbf{k}_{xy}\right) \\ F_3\left(z,\mathbf{k}_{xy}\right) \\ F_4\left(z,\mathbf{k}_{xy}\right) \\ F_5\left(z,\mathbf{k}_{xy}\right) \\ F_6\left(z,\mathbf{k}_{xy}\right) \\ F_7\left(z,\mathbf{k}_{xy}\right) \\ F_8\left(z,\mathbf{k}_{xy}\right). \end{bmatrix} \tag{2.103}$$

Then, the band nth wavefunction at wavevector $\mathbf{k}_{xy}$ is expressed as:

$$\Psi_{n\mathbf{k}_{xy}}\left(\mathbf{r}\right) = \left\{ \begin{array}{c} F_{n1\mathbf{k}_{xy}}\left(z\right)|\rangle_1 + F_{n2\mathbf{k}_{xy}}\left(z\right)|\rangle_2 + F_{n3\mathbf{k}_{xy}}\left(z\right)|\rangle_3 + \\ \cdots + F_{n8\mathbf{k}_{xy}}\left(z\right)|\rangle_8 \end{array} \right\} \cdot e^{i(k_x x + k_y y)}.$$

2.4.5 The strain distribution

The aim of this section will be to describe how strain can actually be calculated in quantum dots. Due to a large difference in lattice constants of Sn (dots) and the matrix (Si, Ge) there is a considerable strain built into the system, which strongly affects the electronic structure, and can be calculated by using two groups of models [30].

- **Atomistic model**. In this model, all atoms in the nanostructures (quantum dots and surrounding matrix) are considered and the total elastic energy of the structure is expressed as a sum of interaction energies between atoms, represented by a sum of classical $n-$body interaction potentials

  $$W = \sum_{i,j} V^{(2)}(\boldsymbol{r}_i - \boldsymbol{r}_j) + \sum_{i,j,k} V^{(3)}(\boldsymbol{r}_i - \boldsymbol{r}_j, \boldsymbol{r}_i - \boldsymbol{r}_k) + \cdots \tag{2.104}$$

  The energy can be expressed in terms of the displacements of each individual atom from its equilibrium position. The relaxed positions of every atom in the system then can be calculated by using a minimization of the energy.

- **Continuum mechanical (CM) model.** In the continuum mechanical model, the quantum dot structure is modelled by an elastic classical continuum medium whose elastic energy is given by

$$W = \frac{1}{2}\sum_{ijkl}\int d\boldsymbol{r}\lambda_{ijkl}e_{ij}e_{kl}, \qquad (2.105)$$

where λ_{ijkl} is the elastic tensor relating the stress and strain tensor by Hooke's law

$$\sigma_{ij} = \sum_{kl}\lambda_{ijkl}e_{kl}. \qquad (2.106)$$

In crystals with the diamond structure (only the α-Sn dots were considered) the elastic tensor is of the form

$$\lambda_{ijkl} = C_{12}\delta_{ij}\delta_{kl} + C_{44}\left(\delta_{ik}\delta_{jl} + \delta_{il}\delta_{jk}\right) + C_{an}\sum_{p=1}^{3}\delta_{ip}\delta_{jp}\delta_{kp}\delta_{lp} \qquad (2.107)$$

where C_{12}, C_{44} and $C_{an} = C_{11} - C_{12} - 2C_{44}$ are the elastic constants.

Throughout this work, the continuum model is adopted as the strain distribution calculation model with a nonuniform rectangular grid, denser in the quantum dot area than the matrix area as illustrated in Fig. 2.5, because from the computer point of view it is less computational demanding. For example, one can choose a suitable size of grid, equaling the lattice constant or bigger. In the minimization of an atomistic model, in contrast, one inevitably has to solve a system of nonlinear equations for atom displacements; while only linear equations in the continuum model system. The strain is calculated by the finite element method, as described in more detail in Ref. [31].

2.4.6 Static electric fields

According to one of the main interests of this work, electric field modulation in antisymmetric double quantum wells, an external electric field will be applied to the system, so it will cause the changes in the quantum wells energy levels and wavefunctions. The external electric field, however, can be simply taken into account by considering it as additional potential $V_F(r) = |e|\mathbf{F}\cdot\mathbf{r}$. In the

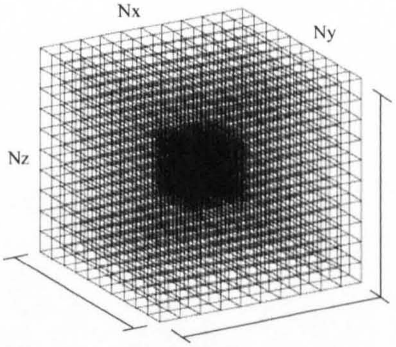

Figure 2.5: Nonuniform rectangular grids, used in the continuum model.

k · p Hamiltonian, the electric field can be included by adding $V_F(\mathbf{r})$ to all diagonal elements of the Hamiltonian.

2.4.7 Methods for solving the k · p Hamiltonian

There are two main methods that can accordingly solve the **k · p** Hamiltonian:

- **Finite-difference method (FDM).** Within this method [32–35], the real space of the system will be divided into small grids and the wavefunction will be represented by points on a discrete three dimensional grid of size $N_xN_yN_z$, and partial derivatives are also turned into finite differences. One therefore obtains an eigenvalue problem of a very large matrix. However, with specialized algorithms for the digitalization of sparse matrices and highly efficient computers nowadays, it can solved [36].

- **Wavefunction expansion methods (WEM).** Within the wavefunction expansion methods [37], the envelope functions, $\psi_j(\mathbf{r})$, will be expressed as a linear combination of a certain set of orthonormal basis functions, $a_l(\mathbf{r})$:

$$\psi_j(\mathbf{r}) = \sum_l A_{jl} a_l(\mathbf{r}), \tag{2.108}$$

where A_{jn} is the coefficients in the expansion. After substituting Eq. (2.108) into the Hamiltonian eigenvalue problem,

$$\sum_j \hat{H}_{ij}\psi_j(\mathbf{r}) = E\psi_i(\mathbf{r}), \tag{2.109}$$

one gets

$$\sum_{jn} \mathcal{H}_{ij}(m,n)A_{jn} = EA_{im}, \tag{2.110}$$

where

$$\mathcal{H}_{ij}(m,n) = \int \mathrm{d}\mathbf{r} a_m(\mathbf{r})^* \hat{H}_{ij} a_n(\mathbf{r}). \tag{2.111}$$

Therefore, the eigenvalue problem (2.110) can be solved by diagonalized the matrix $\mathcal{H}$. One, moreover, can obtain the correct eigenvalues by employing a relatively small basis set by choosing the suitable basis functions. In order to make a right decision, one has to compromise between the simple basis function where the expressions for $\mathcal{H}_{ij}(m,n)$ are fully analytical, such as the plane waves, and the complicated basis functions where required the smallest basis set. There are several different choices of orthonormal basis functions that have been used in the literature. These include plane waves [38–42], the eigenfunctions of the particle in a cylinder with infinite walls (referred to as cylindrical basis in what follows) [43,44], and eigenfunctions of a harmonic oscillator [45]. Throughout the **k** · **p** calculation, this method to calculate electronic and optical properties of the nanostructure has been chosen because the number of necessary basis functions in WEM is small in order to get the accuracy of eigenenergies of several meV. In addition after the wavefunctions are calculated, other relevant physical quantities, such as for example optical matrix elements, can be expressed from the coefficients in the expansion, rather than by calculating three dimensional numerical integration again. One can also chose cylindrical basis functions. Although the expressions for $\mathcal{H}_{ij}(m,n)$ are not fully analytical, these can be calculated efficiently with a small number of basis set functions. It can also exploit the symmetry in dots with cylindrical symmetry.

2.4.8 The eight-band k·p method in cylindrical coordinates

The Γ-valley electronic structure and interband optical matrix elements of Sn quantum dots were calculated using the eight-band **k**·**p** method. It describes simultaneously the conduction band Γ_7^- and the valence bands Γ_8^+ (heavy hole and light hole band) and Γ_7^+ (spin-orbit band), shown in Fig.1.1, including the strain dependent coupling and shifts of these bands. In particular, the form given by Bahder [28] was employed. The Hamiltonian is given as $H = H_k + H_s$, where H_s is the strain part and H_k the kinetic part (that also includes the modulated potential $V_0(\mathbf{r})$ and the spin-orbit interaction H_{so}. The state of the system is described as a linear combination of a multiple of the bulk Bloch functions $|i\rangle$ and slowly varying envelope functions which satisfy the following system of coupled partial differential equations:

$$\sum_{j=1}^{8} H_{ij}\psi_j(\mathbf{r}) = E\psi_i(\mathbf{r}), \tag{2.112}$$

The orthonormal wavefunction expansion method was used to find the size-quantized states (eigenenergies and wavefunctions) in quantum dots. Due to the cylindrical symmetry of the dots considered here, these are taken to be embedded in an outer cylinder of radius R_t and height H_t, with hard walls. Therefore, the envelope function corresponding to band i was written as a linear combination of expansion basis functions

$$\psi_i(\mathbf{r}) = \sum_{nl} A_{inl} f_{nm(i)}(r)\, g_l(z)\, \Phi_m(\phi), \tag{2.113}$$

where

$$f_{nm}(r) = \frac{\sqrt{2}}{R_t}\frac{J_m(k_{nm}r)}{\left|J_{|m|+1}(k_{nm}R_t)\right|}, \tag{2.114}$$

$$g_l(z) = \frac{1}{\sqrt{H_t}}\exp\left(i\frac{2\pi l z}{H_t}\right), \tag{2.115}$$

$$\Phi_m(\phi) = \frac{1}{\sqrt{2\pi}}\exp(im\phi), \tag{2.116}$$

where l and m are integers and n a positive integer, and J_m is the Bessel function of order m and $k_{nm}R_t$ is its n-th zero. Furthermore, $m(i) = m_f -$

$m_j(i)$, where $m_j(i)$ is the z-component of angular momentum of the Bloch function $|i>$, and quantum number m_f is the z-component of the total angular momentum, which is a good quantum number and is the sum of the angular momentum of the Bloch function and that of the envelope function. The states can therefore be labelled as ne_{m_f} (nh_{m_f}), denoting that an electron (hole) is in the n-th state among the states with the z-component of the total angular momentum m_f. After it is substituted into Eq.(2.112), one has arrived at

$$\sum_{i'n'l'} H_{inm(i)l,i'n'm(i')l'} A_{i'n'l'} = EA_{inl}, \tag{2.117}$$

where

$$H_{inm(i)l,i'n'm(i')l'} = \int b^*_{nml} H_{ii'} b_{n'm'l'} r dr dz d\phi. \tag{2.118}$$

It has been evaluated in the terms of T$_1$-T$_{10}$, shown in the appendix part of Ref. [31].

2.4.9 Interaction with external electromagnetic radiation

The aim of this section is to describe the theory which explains the interaction between the active region of the semiconductor devices and electromagnetic radiation because it can describe optical properties of semiconductor devices, such as the photon absorption coefficient. The radiation is described classically by the magnetic vector potential **A** in the Coulomb gauge [46] by substitution of $\hat{\mathbf{p}}$ in the Hamiltonian [46] with

$$\hat{\mathbf{p}} \rightarrow \hat{\mathbf{p}} + |e|\mathbf{A}. \tag{2.119}$$

The Hamiltonian representing the interaction of electrons with electromagnetic radiation then is obtained as

$$\hat{H}' = \frac{(\hat{\mathbf{p}} + |e|\mathbf{A})^2}{2m_0} - \frac{\hat{\mathbf{p}}^2}{2m_0}. \tag{2.120}$$

Throughout this work, one has neglected the quadratic terms in **A** because one mainly focuses on the linear response to external electromagnetic field.

Moreover, the dipole approximation, assuming that the magnetic vector potential $\mathbf{A}$ is not spatially dependent, has been adopted, due to the fact that the wavelengths of interest will be those in the mid-infrared region of the spectrum which is much larger than the size of the nanostructures. Within these approximations, the Hamiltonian of interaction finally is simplified as

$$\hat{H}' = \frac{|e|}{m_0}\hat{\mathbf{p}} \cdot \mathbf{A}. \tag{2.121}$$

From Fermi's Golden rule, the transition probability from an initial state $|i\rangle$ to a final state $|f\rangle$ due to the interaction with electromagnetic radiation of angular frequency ω is given by

$$W_{if} = \frac{2\pi}{\hbar}\left|\left\langle i\left|\hat{H}'\right|f\right\rangle\right|^2 \delta\left(E_f - E_i \mp \hbar\omega\right), \tag{2.122}$$

where the '-' sign corresponds to absorption and '+' to emission, and E_f and E_i are the energies of the final and initial state, respectively.

According to the dipole approximation in which $\mathbf{A}$ does not depend on the coordinate, one can calculate only the momentum operator in the evaluation of the matrix elements between states. After letting the envelope function representations of the initial states $|i\rangle$ and final states $|f\rangle$ as

$$\begin{aligned} \Psi^{(i)}(\mathbf{r}) &= \sum_n \psi_n^{(i)}(\mathbf{r})u_n(\mathbf{r}), \qquad (2.123) \\ \Psi^{(f)}(\mathbf{r}) &= \sum_m \psi_m^{(f)}(\mathbf{r})u_m(\mathbf{r}), \end{aligned}$$

the matrix element of the momentum operator between is then given by

$$\mathcal{P}_{if} = \int \mathrm{d}\mathbf{r}\Psi^{(i)*}(\mathbf{r})\hat{\mathbf{p}}\Psi^{(f)}(\mathbf{r}), \tag{2.124}$$

or

$$\mathcal{P}_{if} = \sum_{mn}\int \mathrm{d}\mathbf{r}\psi_n^{(i)*}u_n^*\left[u_m\hat{\mathbf{p}}\psi_m^{(f)} + \psi_m^{(f)}\hat{\mathbf{p}}u_m\right]. \tag{2.125}$$

From this equation, it has been assumed that the envelope functions $F(\mathbf{r})$ are slowly varying function compared to the rapidly varying Bloch functions, so the envelope function will feel only the average value over the unit cell of the Bloch functions. It can mathematically be expressed as:

$$\int \mathrm{d}\mathbf{r}F(\mathbf{r})u(\mathbf{r}) = \int \mathrm{d}\mathbf{r}F(\mathbf{r})\langle u(\mathbf{r})\rangle, \tag{2.126}$$

where $\langle u(\mathbf{r})\rangle$ is the average value over unit cell of a rapidly varying function. After exploiting this relation and using the condition of orthonormality of the Bloch functions, the equation has been simplified as

$$\mathcal{P}_{if} = \sum_{mn} \int d\mathbf{r}\psi_n^{(i)*} \left(\delta_{nm}\hbar\hat{\mathbf{k}} + \mathbf{p}_{nm}\right) \psi_m^{(f)}, \tag{2.127}$$

where $\hat{\mathbf{k}} = \hat{\mathbf{p}}/\hbar$. Comparing the expression in brackets in (2.127) with the $\mathbf{k}\cdot\mathbf{p}$ Hamiltonian h given in Eq. (2.93), one gets

$$\mathcal{P}_{if} = \frac{m_0}{\hbar}\sum_{mn} \int d\mathbf{r}\psi_n^{(i)*} \left(\frac{\partial h}{\partial \mathbf{k}}\right)_{nm} \psi_m^{(f)}, \tag{2.128}$$

or

$$\mathcal{P}_{if} = \frac{m_0}{\hbar}\langle i|\frac{\partial h}{\partial \mathbf{k}}|f\rangle. \tag{2.129}$$

Finally, the optical cross section of the transition from an initial state $|i\rangle$ to a final state $|f\rangle$ is given as

$$\sigma_{if}^{\varepsilon}(\omega) = \frac{2\pi}{\overline{n}\varepsilon_0 c\omega} \left|\mathcal{M}_{if}^{\varepsilon}\right|^2 g(E_f - E_i \mp \hbar\omega, 2\sigma), \tag{2.130}$$

where $\overline{n}$ is the refraction index. $\mathcal{M}_{if}^{\varepsilon} = \left\langle i\left|\hat{H}'\right|f\right\rangle/A$ is the matrix element which depends only on the direction ε of light polarisation and not on the amplitude of A, related to $\mathcal{P}_{if}$ by

$$\mathcal{M}_{if}^{\varepsilon} = \frac{|e|}{m_0}\mathcal{P}_{if}\cdot\varepsilon, \tag{2.131}$$

and $g(x, 2\sigma)$ is the Gaussian distribution function. According to realistic devices, the quantum dots size in an ensemble is not uniform. In order to account for the spread of sizes of self-assembled quantum dots, and various other sources of line broadening, the lineshape function g in Eq. (2.130) was taken as the Gaussian distribution function, i.e.

$$g\left(E_f - E_i - \hbar\omega, 2\sigma\right) = \frac{1}{\sigma\sqrt{2\pi}} \exp\left[\frac{(E_f - E_i - \hbar\omega)^2}{2\sigma^2}\right], \tag{2.132}$$

where σ is the standard deviation of the Gaussian, which typically amounts to 10% of the transition energy for bound-to-bound transitions. The selection rules for the transitions are $|\Delta m| = 0$ for absorption of z-polarized radiation and $|\Delta m| = 1$ for in-plane-polarized radiation. The computer code according to this method, written by Dr. N. Vukmirović, was used in calculations.

Chapter 3

Band structure calculations of SiGeSn alloys: achieving direct band gap materials

3.1 Introduction

Although still waiting for clear experimental confirmation, the binary GeSn and ternary SiGeSn alloys are considered to be very prospective materials for infrared detectors, as pointed at by Soref and Perry [6], who used linear interpolation scheme to calculate the electronic band structure and optical properties of $Ge_{1-x-y}Si_xSn_y$ alloys and concluded that these will be tunable direct band gap semiconductors. Furthermore, both the direct and indirect band gap in Ge decrease with tensile strain, but the former (initially 140 meV above) does so faster, eventually delivering a direct gap material. Therefore, one can use strained Ge, grown on ternary $Ge_{1-x-y}Si_xSn_y$ alloys [5,47]. There have since been a number of theoretical investigations of the electronic structure of SiGeSn alloys and the influence of composition fluctuations. For instance, using the tight-binding method within the virtual crystal approximation (VCA), the bowing parameter b_{GeSn} value of 0.30 eV [48] for $Ge_{1-x}Sn_x$ was calculated, while another, pseudopotential based calculation [49] gave the value of -0.40 eV. The latter also predicted that $Ge_{1-x}Sn_x$ alloys become direct gap materials, with $0.55 > E_g > 0$ eV for $0.2 < x < 0.6$. The results for b_{GeSn} are quite remote from each other (even in sign), and both grossly deviate from the experimental value, $b_{GeSn}= 2.8$ eV [4,50]. This clearly indicates that VCA cannot explain the behaviour of disordered $Ge_{1-x}Sn_x$ alloys [51], although it is considered reasonably accurate for $Si_{1-x}Ge_x$. In order to take into account the alloy disorder effects, the Coherent Potential Approximation (CPA) was employed for $Si_{1-x}Ge_x$ alloys. According to Chibane *et al.* [52], who used the model developed by Zunger *et al.* [22], the calculated optical band gap gap bowing is in good agreement with experiment for small Sn content. However, so far there is no theoretical model which properly describes the optical properties of GeSiSn alloys in a wide range of compositions. The aim of this chapter is to theoretically explore various possibilities of achieving tunable direct gap semiconductors based on group IV materials, and to investigate the composition dependence of their electronic and optical properties.

In this chapter, the band structure of Si-Ge-Sn alloys is explored in search of new direct bandgap semiconductors. In Sec. 3.2 the theoretical framework is presented. Moreover, the model which explains the behaviour of the alloys and the validity of the models is also given in Sec. 3.3. In order to search for a direct band gap semiconductor, the results of calculation of composition dependence of energy band structure of relaxed $Ge_{1-x}Sn_x$ and strained Ge on relaxed $Ge_{1-x-y}Si_xSn_y$ alloys, strained $Ge_{1-x}Sn_x$ on relaxed $Ge_{1-y}Sn_y$ and relaxed $Si_{1-x}Sn_x$ alloys are presented in Sec. 3.4. Finally, the conclusions are presented in Sec. 3.5.

3.2 Computational method

For band structure calculation of SiGeSn alloys the charge self-consistent pseudopotential $X\alpha$ method is used. It finds the self-consistent solution of the Schrödinger equation, with the lattice constituents described by ionic pseudopotential formfunctions. Compared to the first-principles density functional theory in the local density approximation [7, 8], which perform the total energy minimization, the $X\alpha$ method is able to reproduce the electronic structure (i.e. the band gaps, or optical properties of semiconductors) with very good accuracy, without any additional schemes like GW approximation or "scissors correction" as are employed in total energy approaches. On the other hand, this method would not deliver the ground state properties (e.g. the atomic coordinates relaxation, or lattice constant bowing) very accurately, though these can be externally supplied to the calculation. Since the electronic properties are interested, the $X\alpha$ method was adopted, and experimentally obtained lattice parameters were used where available.

The calculation starts with the construction of the effective potential, including the pseudopotential, the Hartree potential and the exchange-correlation potential

$$V_{\text{eff}}(\mathbf{r}) = V_{ps} + V_{\text{Hartree}}(\mathbf{r}) + V_{\text{xc}}(\mathbf{r}), \tag{3.1}$$

where $V_{Hartree}(\mathbf{r}) = \int \frac{e^2 n(\acute{\mathbf{r}})}{|\mathbf{r}-\acute{\mathbf{r}}|} d\acute{\mathbf{r}}$, and $n(\mathbf{r})$ is the real-space electron density. The Hartree potential is evaluated in momentum space

$$V_{\text{Hartree}}(\mathbf{q}) = 4\pi e^2 \frac{n(\mathbf{q})}{q^2}, \tag{3.2}$$

where $\mathbf{q}$ is the wave vector and $n(\mathbf{q})$ are the Fourier coefficients of charge density. This is evaluated in two steps. First, the density was computed on a 16 × 16 × 16 grid of the simple unit cell in real space. Second, a fast Fourier transform was used to transform from $n(\mathbf{r})$ to $n(\mathbf{q})$. The exchange-correlation potential was evaluated in a similar manner. The local exchange-correlation potential of the Slater type has been chosen, defined as

$$V_{xc}(\mathbf{q}) = -\alpha \frac{3}{2} e^2 \left(\frac{3}{\pi}\right)^{\frac{1}{3}} \left[n^{\frac{1}{3}}(\mathbf{q})\right], \tag{3.3}$$

where $\left[n^{\frac{1}{3}}(\mathbf{q})\right]$ are the Fourier coefficients of the cube root of the charge density. Based on the approximation of Slater [13], α is a constant which Schlüter *et al.* [53] have set to 0.79. The calculation of this potential was similar to the calculation of $n(\mathbf{q})$, except that the cube root of $n(\mathbf{r})$ on the cubic grid was taken before transforming from $[n(\mathbf{r})]^{\frac{1}{3}}$ to $\left[n^{\frac{1}{3}}(\mathbf{q})\right]$ by fast Fourier transform. The $V_{xc}(\mathbf{q})$ was then evaluated using Eq. (3.3). As for the pseudopotential, the same form as Srivastava [15] has been used,

$$V_{ps}(q) = \left(\frac{b_1}{q^2}\right)(\cos(b_2 q) + b_3)\exp(-b_4 q^4), \tag{3.4}$$

with the parameters for Si, Ge, and Sn given in Table 3.1. These are slightly readjusted values from those given in Ref. [15], as dictated by a larger energy cutoff, and a different method of integration over the Brillouin zone, used in this work.

Parameter	Si	Ge	Sn
b_1(Ry)	-1.213	-1.032	0.401
b_2	0.785	0.758	1.101
b_3	-0.335	-0.345	0.041
b_4	0.020	0.024	0.018

Table 3.1: Parameters of the pseudopotential of Si, Ge and α-Sn

The electronic structure is found by solving the Kohn-Sham equation (in atomic units $\hbar = 2m_e = \frac{e^2}{2} = 1$):

$$\left[-\nabla^2 + V_{eff}(\mathbf{r})\right] \psi_n(\mathbf{k};\mathbf{r}) = \epsilon_n(\mathbf{k};\mathbf{r})\, \psi_n(\mathbf{k};\mathbf{r}), \tag{3.5}$$

which is done using the self-consistent pseudopotential plane waves method [9], with a kinetic energy cutoff of 24 Ry, the value which gives good convergence of the calculation. The improved linear tetrahedron method [17] was used for integration over the Brillouin zone, with 34 k-points in the irreducible wedge. The linear mixing scheme was adopted and the convergence of the self-consistent calculation was considered to be adequate when the total energy of the system was stable to within 10^{-3} Ry. The diagram of self-consistent pseudopotential plane waves method is shown in Fig. 3.1.

In these calculations the spin-orbit coupling is not included because it would double the size of the problem while not being essential for the aim of this work, which is to find whether the smallest band gap is direct or indirect (and this is determined only by the behaviour of the conduction band).

Including the spin-orbit coupling would bring slight quantitative corrections in the calculated values of band gaps (with the ionic pseudopotential

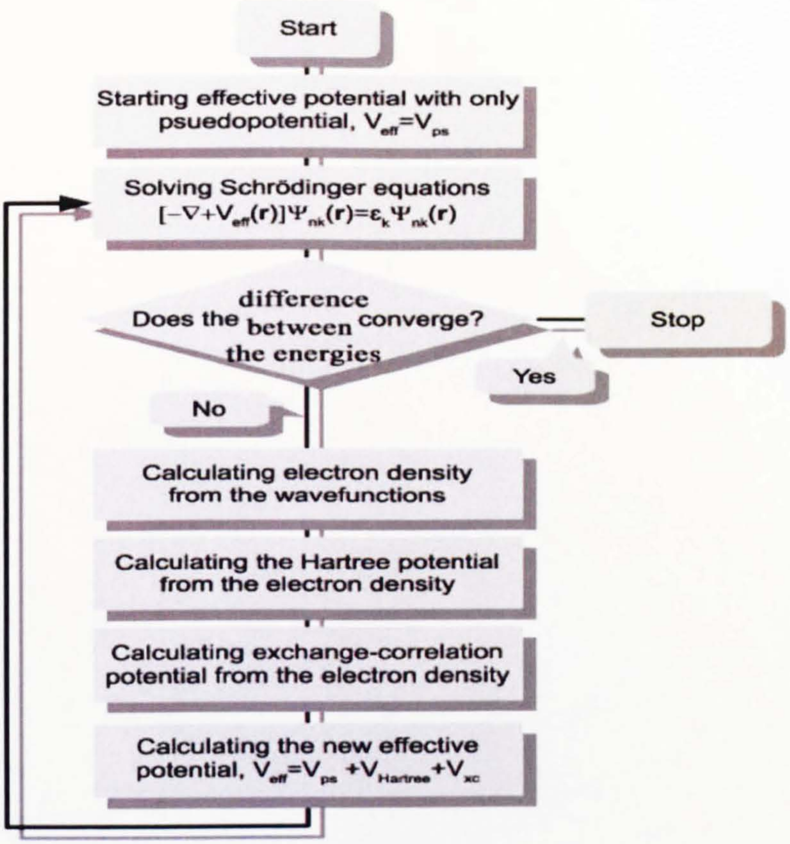

Figure 3.1: Diagram shows the algorithm of the self-consistent pseudopotential plane waves method.

formfunctions re-fitted to reproduce the known experimental values for elemental Si, Ge and Sn in this case), but this would not affect the predicted direct-indirect crossover points.

Similar conclusion on a relatively small influence of spin-orbit coupling on the topic of interest here has been drawn in [54], based on empirical pseudopotential calculations in the Ge-Sn alloy.

The calculated band structures of bulk Si, Ge, and α-Sn are given in Fig.3.2, with the band gap of Si (Ge) being 1.2 eV (0.71 eV), while α-Sn has a negative direct band gap. The longitudinal (m_l) and transverse effective mass (m_t)

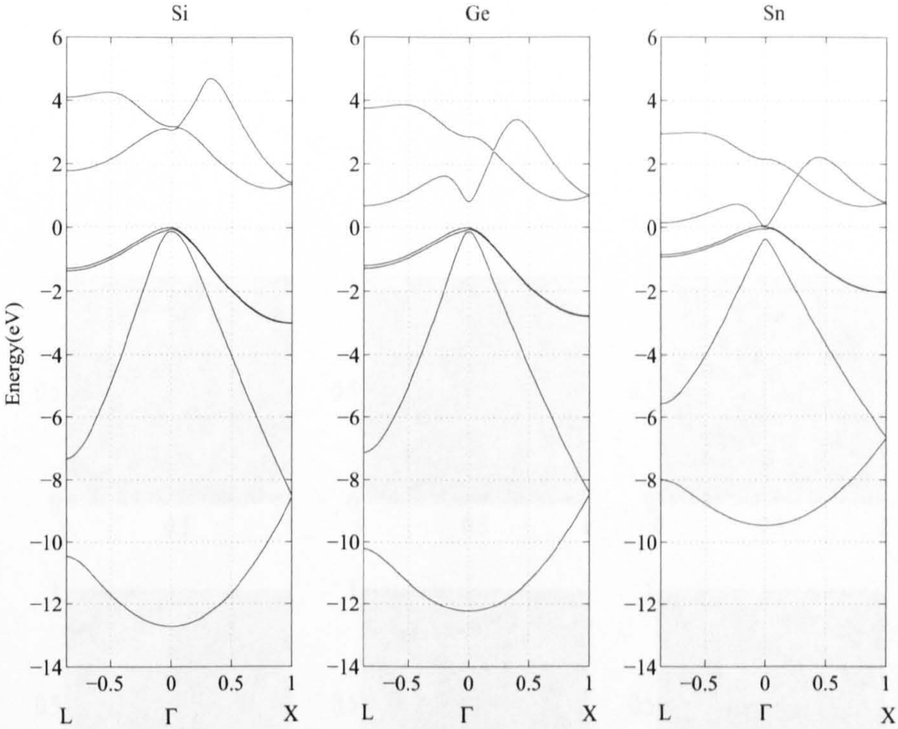

Figure 3.2: Electronic band structure of Si, Ge, and α-Sn.

for the X-valley in Si are $0.87m_0$ and $0.22m_0$. Similarly, the L-valley in Ge has m_l =$1.68m_0$ and m_t =$0.16m_0$. In order to check the reliability of these parameters, the resulting electron density plots for silicon, germanium and tin are shown in Fig. 3.3, 3.4, 3.5 and 3.6. All these are in very good agreement with the published values, indicating that the parameters can be reliably used for further calculations.

3.3 Alloy models and their validity

Alloy properties can be evaluated either within the virtual crystal approximation (VCA) with identical, average-composition atoms populating the lattice sites of the minimum-volume crystalline unit cell, or by populating individual lattice sites only with pure element atoms, in proportion to the alloy composition ("mixed atom method"), in which case one has to use a supercell, with increased volume. In the latter case one can optionally include atomic relax-

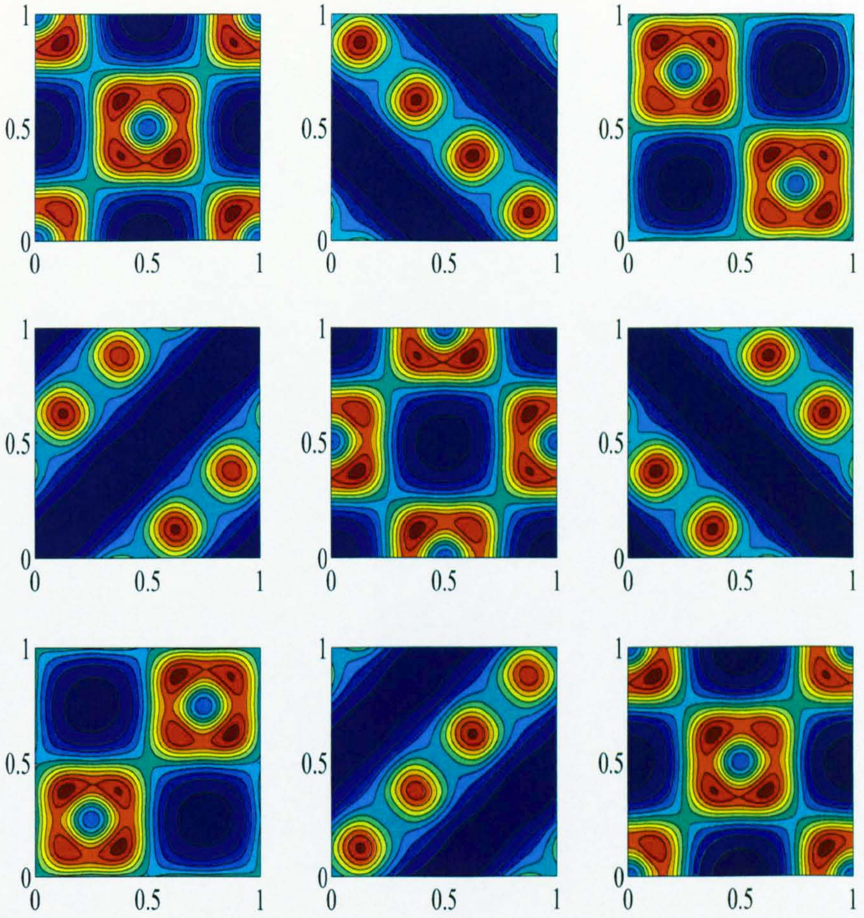

Figure 3.3: Electron density plots between 2 basal (001) planes from $z = 0$ to $z = A_0$ of silicon. Starting from the top left, each subsequent figure in the normal reading order is displaced by Δz=0.125A_0 along the (001) direction where A_0 is the lattice constant of silicon.

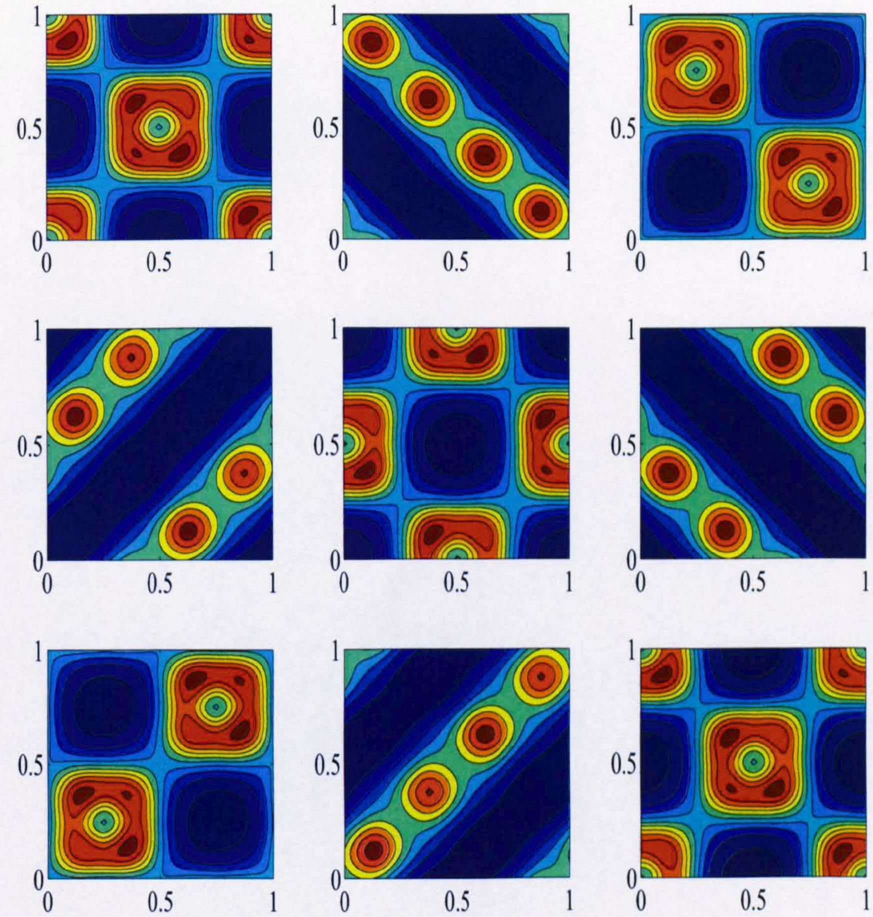

Figure 3.4: Same as in Fig. 3.3, but for germanium.

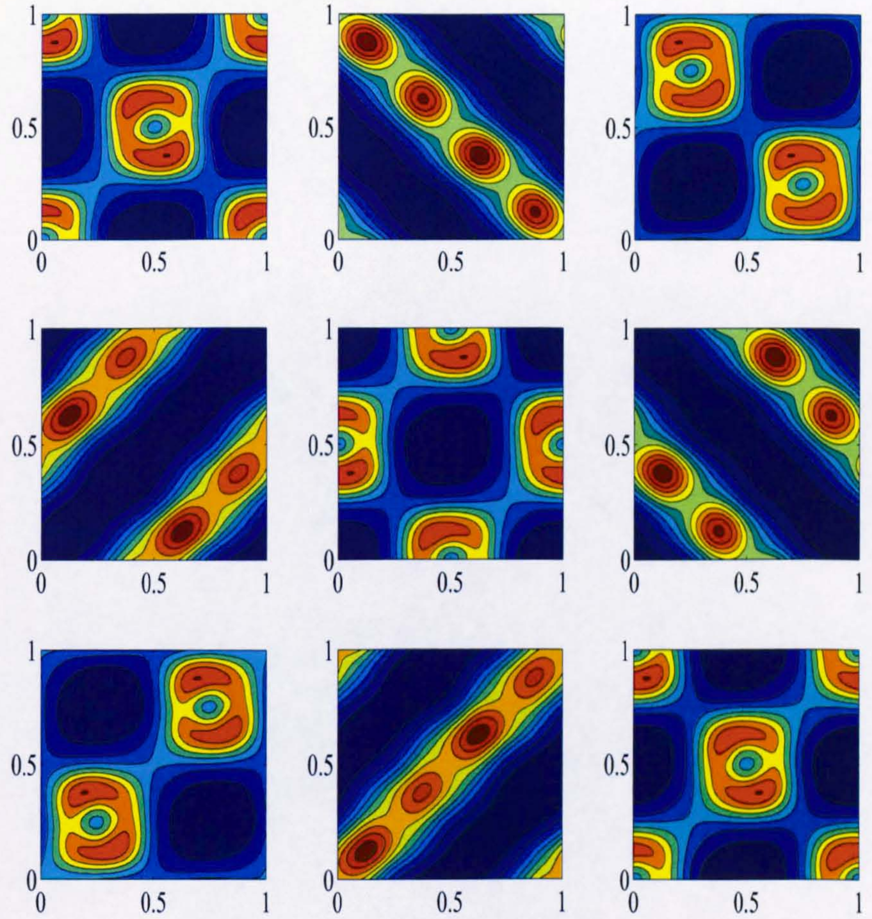

Figure 3.5: Same as in Fig. 3.3, but for α-tin

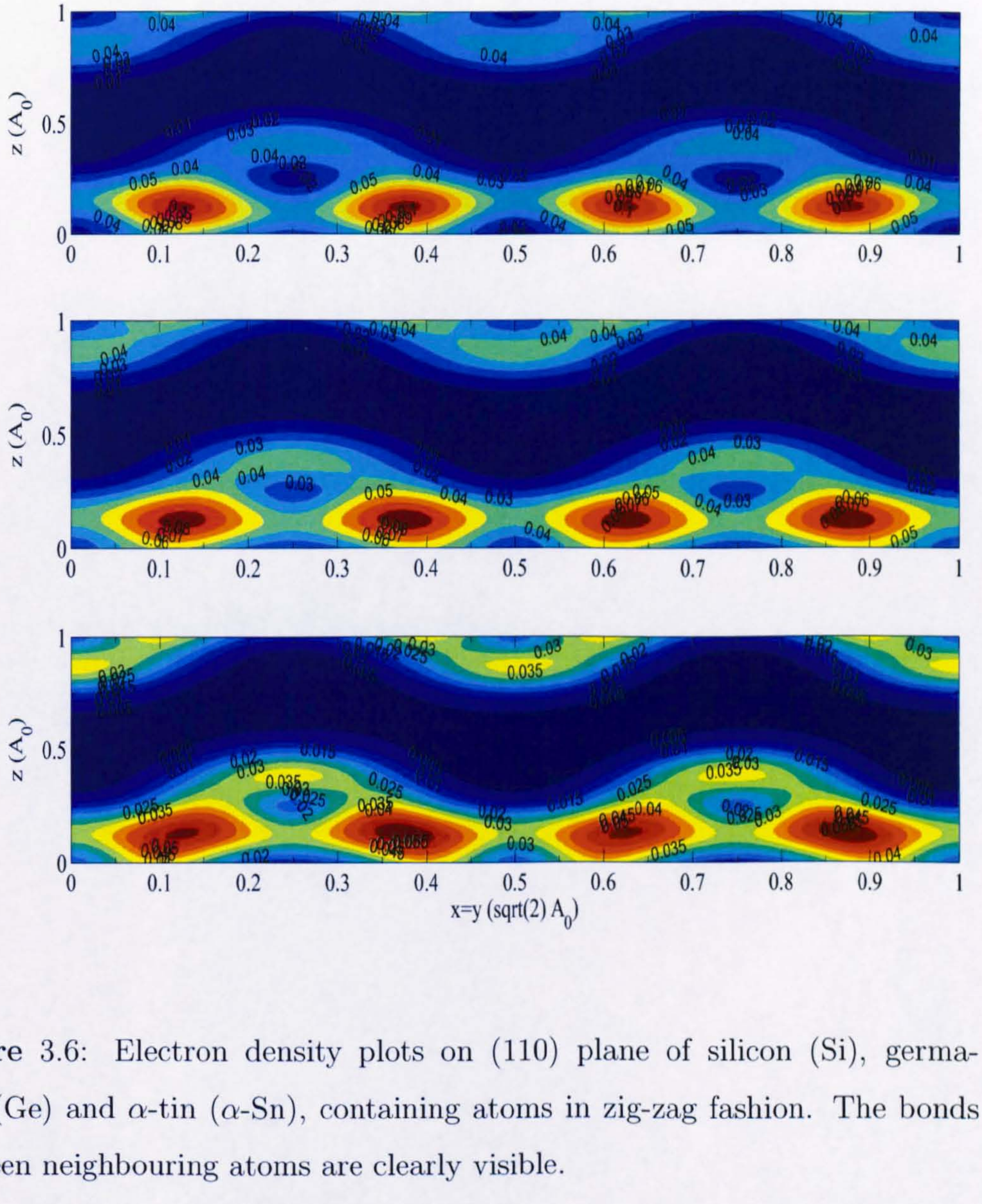

Figure 3.6: Electron density plots on (110) plane of silicon (Si), germanium(Ge) and α-tin (α-Sn), containing atoms in zig-zag fashion. The bonds between neighbouring atoms are clearly visible.

ation, i.e. shifts of different types of atoms from their idealised positions (those occupied by average-composition atoms), which obviously influences the bond lengths between neighbouring atoms. Relaxed atomic coordinates can be found either independently of the band structure (using e.g. empirical interatomic potentials), or together with it (by methods minimising the total energy). In this thesis, however, the relaxation of atomic coordinates was not accounted for. The former (VCA) approach is simpler but may be grossly inaccurate in some cases. The latter approach is more realistic, accounting for the effects of disorder and composition fluctuations, but becomes computationally very demanding as the supercell size increases. It will be discussed in the next section.

3.3.1 Supercell and the reciprocal lattice vectors

According to Z. Ikonić (unpublished), consider a unit cell of a superlattice (supercell) grown in the [001] crystallographic direction, having a total of N crystalline monolayers per period. The monolayer here denotes a half of a cubic lattice constant thick layer. The material composition may vary arbitrarily along the period. For example the superlattice period has a total of n layers, each of them has n_i $(i = 1, \ldots, n)$ monolayers (so $\sum_{i=1}^{n} n_i = N$ - the total number of monolayers). The height of the whole period, c, will be

$$c = \frac{1}{2}\sum_{i=1}^{n} n_i c_i \tag{3.6}$$

where c_i is the lattice constant in the growth direction (in the unstrained case, the lattice constant, a, of the alloy). Allowing for an enlarged supercell with n_{cell} minimum-volume supercells stacked side-by-side (i.e. parallel to the (001) growth plane), the elementary translation vectors $\mathbf{a}_1$, $\mathbf{a}_2$, and $\mathbf{a}_3$, of the minimum-volume supercell for this superlattice for n_{cell} =1, 2, 4, 8, 16, ..., may then be chosen as:

$$\mathbf{a}_1 = +\frac{\ell a}{2}\mathbf{i} + \frac{\ell a}{2}\mathbf{j}, \tag{3.7}$$

$$\mathbf{a}_2 = -\frac{\ell a}{2}\mathbf{i} + \frac{\ell a}{2}\mathbf{j}, \tag{3.8}$$

$$\mathbf{a}_3 = \frac{a \cdot mod(N,2)}{2}\mathbf{j} + c\mathbf{k}, \tag{3.9}$$

for $n_{cell} = 1, 4, 16, \ldots$, and

$$\mathbf{a}_1 = \ell a\mathbf{i}, \tag{3.10}$$

$$\mathbf{a}_2 = \ell a\mathbf{j}, \tag{3.11}$$

$$\mathbf{a}_3 = \frac{a \cdot mod(N,2)}{2}\mathbf{j} + c\mathbf{k}, \tag{3.12}$$

for $n_{cell} = 2, 8, \ldots$, where

$$\ell = \begin{cases} \sqrt{n_{cell}}, & \text{for } n_{cell} = 1, 4, 16, \ldots \\ \sqrt{\frac{n_{cell}}{2}}, & \text{for } n_{cell} = 2, 8, \ldots \end{cases}.$$

Therefore, the elementary reciprocal lattice vectors $\mathbf{g}$ in the two cases are

$$\mathbf{g}_1 = 2\pi\left(+\frac{1}{\ell a}\mathbf{i} + \frac{1}{\ell a}\mathbf{j} - \frac{mod(N,2)}{2\ell c}\mathbf{k}\right), \tag{3.13}$$

$$\mathbf{g}_2 = 2\pi\left(-\frac{1}{\ell a}\mathbf{i} + \frac{1}{\ell a}\mathbf{j} - \frac{mod(N,2)}{2\ell c}\mathbf{k}\right), \tag{3.14}$$

$$\mathbf{g}_3 = \frac{2\pi}{c}\mathbf{k}, \tag{3.15}$$

for $n_{cell} = 1, 4, 16, \ldots$, and

$$\mathbf{g}_1 = \frac{2\pi}{\ell a}\mathbf{i}, \tag{3.16}$$

$$\mathbf{g}_2 = 2\pi\left(\frac{1}{\ell a}\mathbf{j} - \frac{mod(N,2)}{2\ell c}\mathbf{k}\right), \tag{3.17}$$

$$\mathbf{g}_3 = \frac{2\pi}{c}\mathbf{k}, \tag{3.18}$$

for $n_{cell} = 2, 8, \ldots$.

The reciprocal lattice vectors are then constructed as all linear combinations of the elementary vectors, i.e.

$$\mathbf{g} = n_1\mathbf{g}_1 + n_2\mathbf{g}_2 + n_3\mathbf{g}_3, \quad n_1, n_2, n_3 = 0, \pm 1, \pm 2, \ldots \tag{3.19}$$

In this work the cubic unit cell (supercell) with 4 minimum-volume zinc-blende unit cells is used. With this choice, the X point at the boundary of the first Brillouin zone folds to the Γ point of the supercell Brillouin zone, but the L point does not change. Furthermore, this choice enables the binary compositions with a 12.5% composition step to be investigated, e.g. the $A_{0.25}B_{0.75}$ alloy is obtained by putting 2 atoms of A and 6 atoms of B in lattice sites. There are different ways for placement of these 8 atoms, each having somewhat different band structure, and the alloy band structure is calculated by averaging over all the possibilities. Within the mixed-atom supercell approach, some care is necessary when "unfolding" the band structure to identify (resolve) the energies at the Γ and X points of the Brillouin zone in the minimum-volume unit cell representation (both are folded onto the supercell Γ point), as shown in Fig. 3.7.

The lattice constant of an alloy can be estimated from Vegard's law [55]

$$a_0(x)^{AB} = (1-x)a_0^A + xa_0^B, \tag{3.20}$$

where a_0^A and a_0^B are the lattice constants of elemental crystals of atoms A and B respectively, and a more accurate expression (with bowing) was taken where available.

The first set of test calculations, using both methods, was done for the $Si_{1-x}Ge_x$ alloy. In the case of the VCA, the pseudopotential was taken to vary linearly between the two constituents [18], i.e.

$$V(q)^{SiGe} = (1-x)V(q)^{Si} + xV(q)^{Ge} \tag{3.21}$$

where $V(q)^{Si}$ and $V(q)^{Ge}$ are the pseudopotentials of elemental Si and Ge. By the same token, the energy band gap between the top of the valence band at Γ and point $g = X, L, \Gamma$ in the conduction band of a binary alloy within the VCA may be expected to be $E_g^{SiGe} = (1-x)E_g^{Si} + xE_g^{Ge}$, but the alloy disorder and other effects make this just the first approximation, and a more accurate dependence is

$$E_g^{SiGe} = (1-x)E_g^{Si} + xE_g^{Ge} + b_{SiGe}x\,(1-x), \tag{3.22}$$

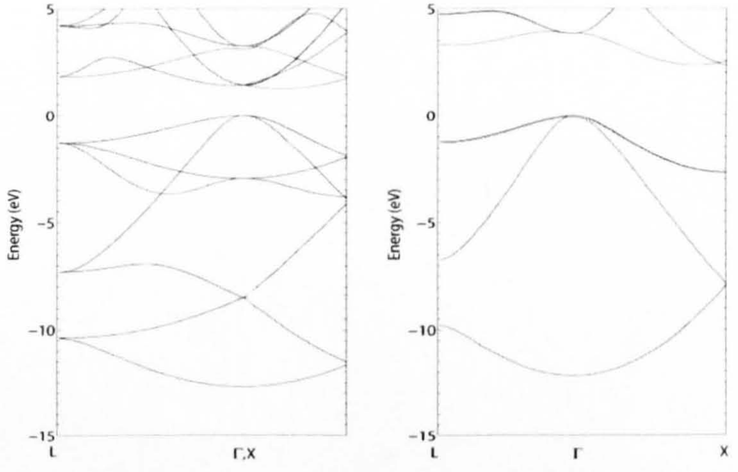

(a) Silicon

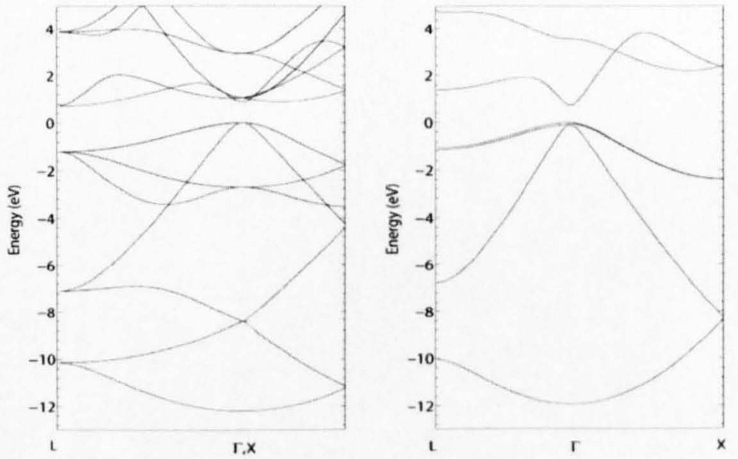

(b) Germanium

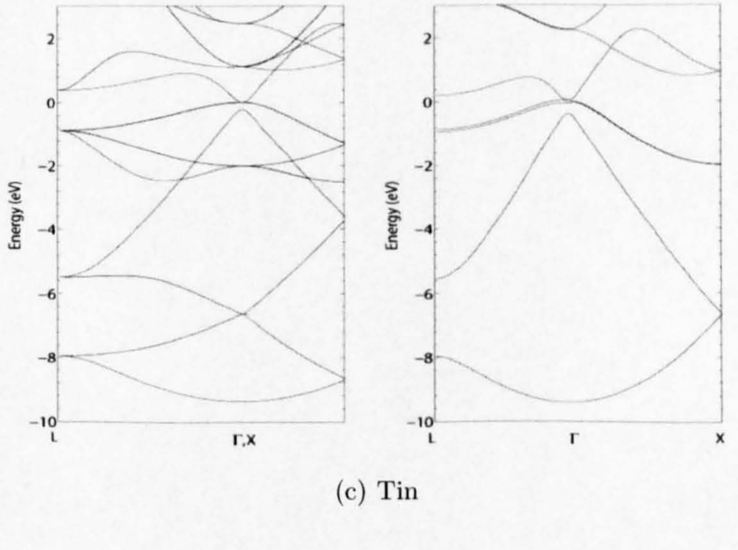

(c) Tin

Figure 3.7: The band structure of a) Silicon, b) Germanium and c) Tin calculated by the mixed-atom supercell approach with 8 atoms in a cell (left) and by the virtual crystal approximation (right).

where b_{SiGe} is a bowing parameter, and the VCA and the mixed-atom method may give quite different values.

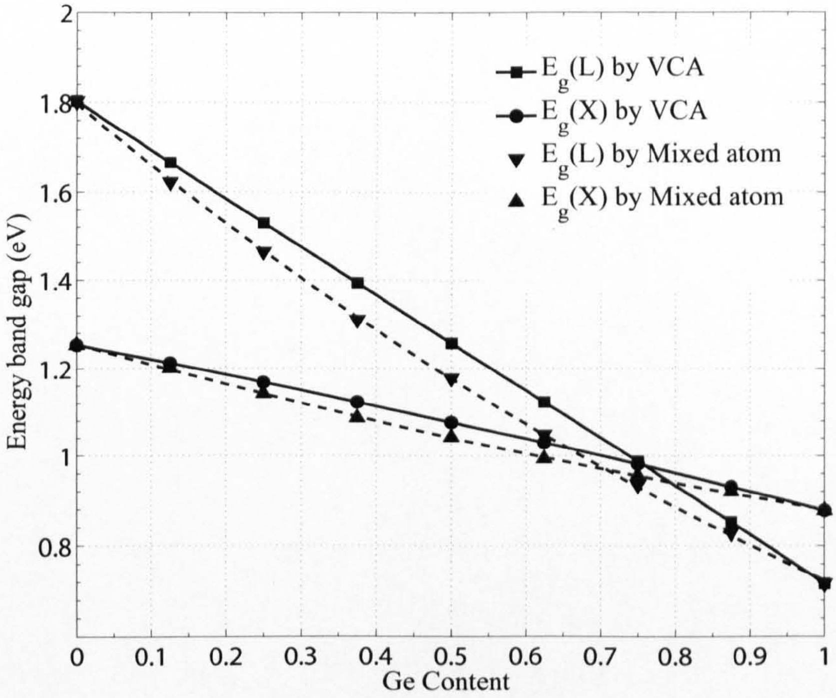

Figure 3.8: The band gaps of $\mathrm{Si}_{1-x}\mathrm{Ge}_x$ at X and L points, calculated within the VCA and the mixed-atom method.

The calculated band gaps of $\mathrm{Si}_{1-x}\mathrm{Ge}_x$ are shown in Fig. 3.8. The gaps for the X and L valleys, calculated by the mixed atom method, are fitted to expression: $E_X = 0.108x^2+0.267x+0.881$ eV and $E_L = 0.335x^2+0.738x+0.724$ eV. Therefore, the bowing parameter of this alloy is 0.33 eV for the Ge content x >0.70 (where the L valley is the lowest), and 0.11 eV for x <0.70 (where the X valley is the lowest). These values are in good agreement with the calculations of S. Krishnamurthy and A. Sher [56]. On the other hand, the VCA predicts 0.01 eV for $x > 0.75$ and -0.04 eV otherwise.

Calculations for the (100)-tetragonally distorted (biaxially strained) $\mathrm{Si}_{1-x}\mathrm{Ge}_x$ alloys, i.e. grown on a relaxed $\mathrm{Si}_{1-y}\mathrm{Ge}_y$ substrate have also been performed . The lateral lattice constant $a_{\|}(x)$ equals that of the substrate, and in the perpendicular direction, $a_\perp$ or c_i, it is [57]

$$a_\perp(x) = a_0(x)\left(1 - 2\frac{c_{12}(x)}{c_{11}(x)}\frac{a - a_0(x)}{a_0(x)}\right), \tag{3.23}$$

where c_{11} and c_{12} are the elastic constants [58, 59], given in Table 3.2 for Si, Ge, and α-Sn, and are approximated by Vegard's law for the alloys,

	Si	Ge	Sn
c_{11}(Mbar)	1.67	1.32	0.69
c_{12}(Mbar)	0.65	0.494	0.29

Table 3.2: Elastic constants c_{11} and c_{12} of Si, Ge, and α-Sn.

$$c(x)^{AB} = (1 - x)c^A + xc^B, \tag{3.24}$$

where c represents either c_{11} or c_{12}.

Strain causes a change of some properties of the alloy unit cells. For instance, the biaxial strain typical for lattice-mismatched layer grown on a [001] oriented substrate changes the lattice type from cubic to tetragonal, and similarly the volume of the unit cell also changes, which is taken into account in calculations.

The results of the calculation for strained $\mathrm{Si}_{1-x}\mathrm{Ge}_x$ grown on relaxed $\mathrm{Si}_{1-y}\mathrm{Ge}_y$, Fig. 3.9, show that the minimum energy gap (of the X valleys parallel to the interface, region B on figures) can be written as $E_{X_\parallel}(x, y) = 1.069 - 0.425x + 0.533y - 0.152x^2 - 0.324y^2$, and for the perpendicular X valley (region A on figures) as $E_{X_\perp}(x, y) = 1.056 + 0.250x - 0.087y - 0.208x^2 - 0.316y^2$, whereas the energy gap for the L valley (region C) is $E_L(x, y) = 1.532 - 0.739x + 0.185y - 0.075x^2 - 0.417y^2$. These results are in good agreement with the work of Rieger and Vogl [59], which are generally considered reasonably accurate when compared to experiment, justifying the applicability of the present method for both strained and unstrained alloys.

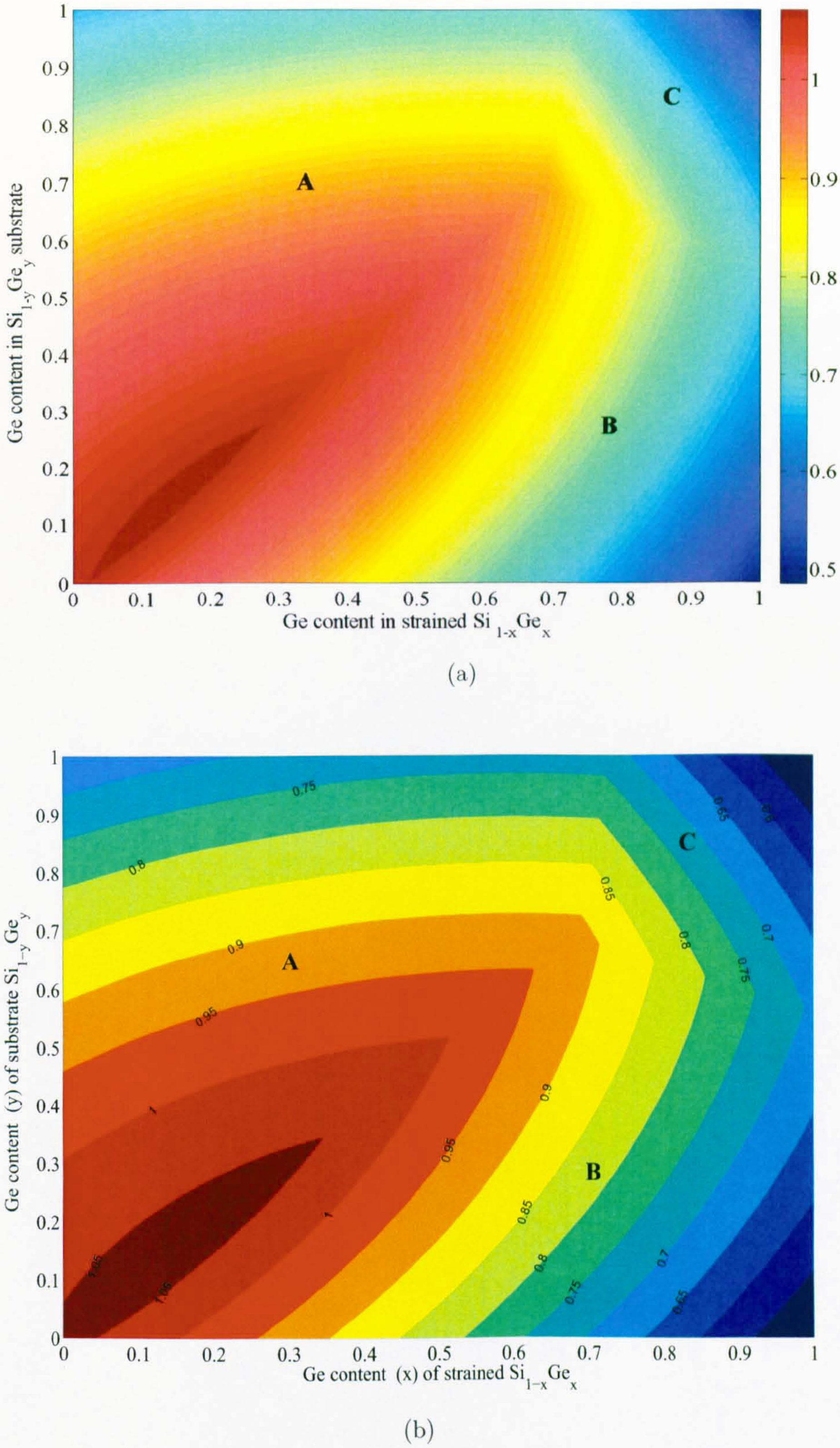

(a)

(b)

Figure 3.9: The minimum band gap, in eV, in the X valleys parallel to the interface (region B), in the X valleys perpendicular to the interface (region A) and L valleys (region C) of strained Si$_{1-x}$Ge$_x$ grown on relaxed Si$_{1-y}$Ge$_y$.

3.4 Results and discussion

In search for direct tunable gap semiconductors, in this section the relaxed $Ge_{1-x}Sn_x$ alloy, strained Ge grown on relaxed $Ge_zSi_xSn_y$ substrate, where $z = 1 - x - y$, strained $Ge_{1-x}Sn_x$ grown on relaxed $Ge_{1-y}Sn_y$, and the relaxed $Si_{1-x}Sn_x$ alloy were considered.

3.4.1 Relaxed $Ge_{1-x}Sn_x$ alloys

In studying of the composition dependence of the band structure of unstrained $Ge_{1-x}Sn_x$ alloy, it is important to note the strong bowing effect in the lattice constant of this alloy, that should be taken into account, even though the size of this effect is not very well known. According to the experimental data for $Ge_{1-x}Sn_x$ from Ref. [60], the lattice constant is given by

$$a_{GeSn}(x) = a_{Sn}x + \theta_{SnGe}x + a_{Ge}(1 - x), \tag{3.25}$$

where $\theta_{SnGe} = 0.166$ Å, although its validity has been experimentally established only for the Sn content ≤ 0.2 [60].

From Fig. 3.10, which shows the results obtained within the VCA, the Sn content dependence of the band gap for the L valley is $E_L = 0.34x^2 - 0.91x + 0.71$, and for the Γ valley it is $E_\Gamma = 0.78x^2 - 2.00x + 0.87$. The optical (band gap) bowing parameters are clearly much smaller than the above experimental value [4,50], again showing that the VCA cannot properly predict the composition dependence of the electronic structure of $Ge_{1-x}Sn_x$ alloys. On the other hand, the results presented Fig. 3.10, obtained within the mixed atom method, show that the relaxed $Ge_{1-x}Sn_x$ has the indirect-to-direct band gap transition at a Sn content of approximately 0.17, with the band gaps for the L and Γ valleys given by $E_L = 2.28x^2 - 2.85x + 0.72$ and $E_\Gamma = 2.49x^2 - 3.76x + 0.88$, respectively. The bowing parameter of relaxed $Ge_{1-x}Sn_x$ alloys is thus 2.49 eV, in good agreement with experiment [4]. The Sn content of 17% for the indirect-to-direct gap transition is also in general agreement with (i.e. in between) the values reported elsewhere, of 15% [62] and 20% [54].

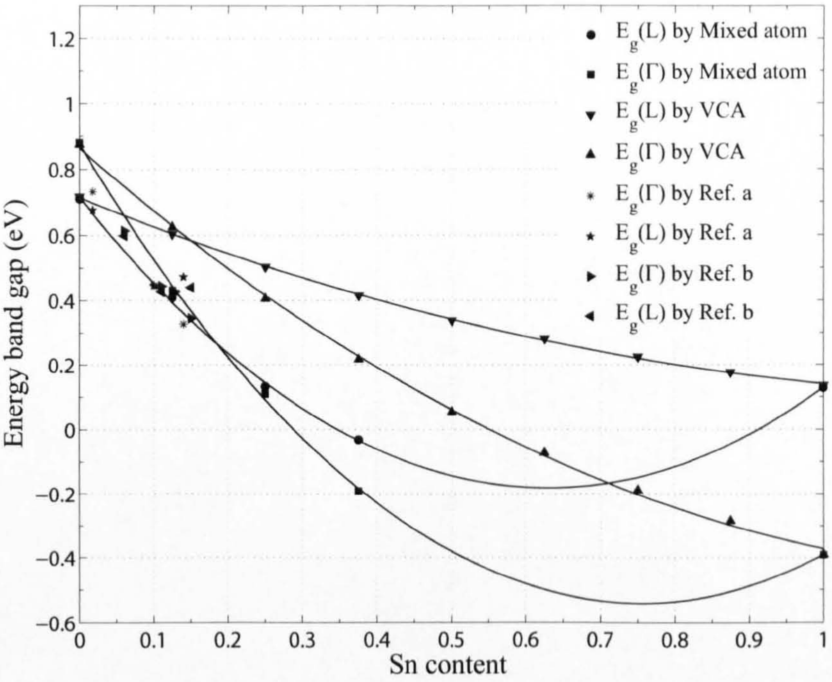

Figure 3.10: The minimum band gap of relaxed $\mathrm{Ge}_{1-x}\mathrm{Sn}_x$ for Γ and L valleys, calculated within the VCA and within the mixed atom method. A couple of available experimental values are also displayed, i.e. Ref.a is Ref. [61] and Ref.b is Ref. [4].

3.4.2 Strained Ge on relaxed $\mathrm{Ge}_{1-x-y}\mathrm{Si}_x\mathrm{Sn}_y$ alloys

The lattice constant of $\mathrm{Ge}_{1-x-y}\mathrm{Si}_x\mathrm{Sn}_y$ alloys was taken to depend on the Si content (x) and Sn content (y) as [60]

$$\begin{aligned} a_{GeSiSn}(x,y) &= a_{Ge} + \triangle_{SiGe}x + \theta_{SiGe}(1-x) \\ &\quad + \triangle_{SnGe}y + \theta_{SnGe}(1-y), \end{aligned} \tag{3.26}$$

where $\triangle_{SiGe} = a_{Si} - a_{Ge}$, $\triangle_{SnGe} = a_{Sn} - a_{Ge}$, and $\theta_{SiGe} = -0.026$ Å.

The band gap for the L valley was now found to be described as $E_L(x,y) = 0.723 + 0.564x - 2.352y + 0.189xy - 0.074x^2 + 0.068y^2$, while the band gap for Γ valley is $E_\Gamma(x,y) = 0.880 + 0.929x - 3.807y - 0.160xy - 0.078x^2 + 0.937y^2$, where x and y denote the content of Si and Sn, respectively. The line defined

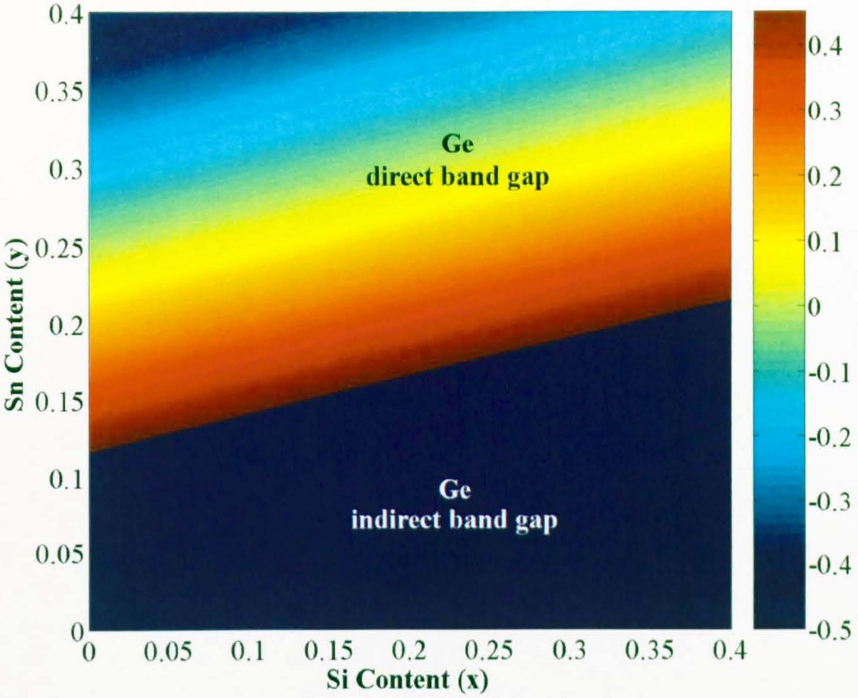

Figure 3.11: Band gap energy (in eV) of strained Ge grown on relaxed $Ge_{1-x-y}Si_xSn_y$ alloys.

by $E_L = E_\Gamma$ in the x-y plane is the boundary between regions where the band gap of strained Ge is direct or indirect. A direct band gap is achieved for sufficiently large tensile strain of Ge, achievable by growing it on appropriate $Ge_{1-x-y}Si_xSn_y$ alloy substrate, as given in Fig. 3.11.

3.4.3 Strained $Ge_{1-x}Sn_x$ on relaxed $Ge_{1-y}Sn_y$ alloys

For this calculation one needs the elastic constants for the GeSn alloy. This was estimated by linear interpolation, since no quadratic correction parameter for this alloy is known. The band gap for the L valley is now found to be described by $E_L(x, y) = 0.672 - 1.794x - 1.181y + 8.780xy - 2.958x^2 - 3.925y^2$, and for the Γ valley by $E_\Gamma(x, y) = 0.782 - 1.483x - 2.577y + 8.216xy - 1.653x^2 - 1.866y^2$, where x and y denote the Sn content in strained $Ge_{1-x}Sn_x$ layer and in relaxed $Ge_{1-y}Sn_y$ substrate, respectively. Here again the region in the parameter space that corresponds to a direct band gap semiconductor is found, achieved by the combined influence of material composition and tensile strain, Fig. 3.12.

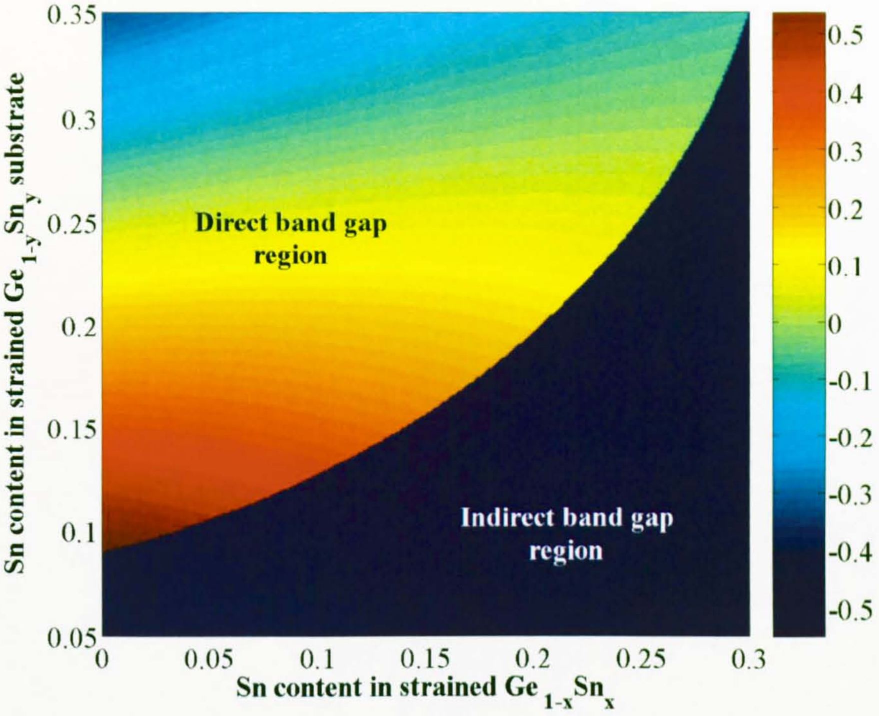

Figure 3.12: The minimum band gap (in eV) of strained $\mathrm{Ge}_{1-x}\mathrm{Sn}_x$ grown on relaxed $\mathrm{Ge}_{1-y}\mathrm{Sn}_y$ alloys.

3.4.4 Relaxed $\mathrm{Si}_{1-x}\mathrm{Sn}_x$ alloys

In this calculation the lattice bowing parameter of the alloy lattice constants of SiSn alloys was set to zero.

Its value has not been experimentally determined, and (although it may seem a bit surprising in view of a very large difference in atomic radii) the very recent LDA calculations [63] predict a negligible deviation of SiSn alloy lattice constant from Vegard's law.

Within the mixed atom method, the band gaps for the L and X valleys in relaxed $\mathrm{Si}_{1-x}\mathrm{Sn}_x$ alloy were found to be given by $E_L(x) = 1.837 - 4.860x + 3.124x^2$ and $E_X(x) = 1.281 - 1.399x + 0.772x^2$, respectively, while the band

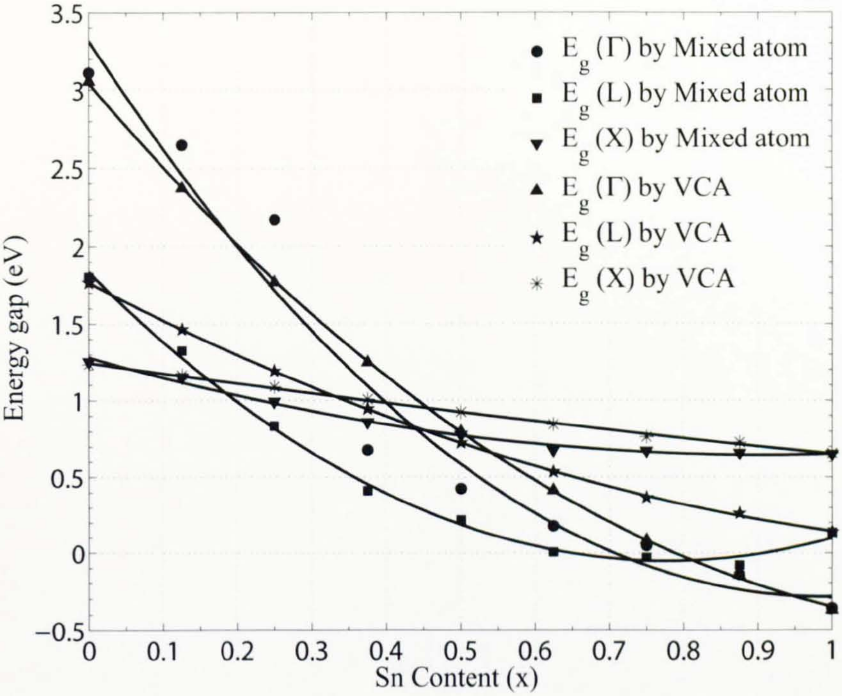

Figure 3.13: The minimum energy band gap (in eV) of relaxed $Si_{1-x}Sn_x$ alloy, calculated within the VCA and within the mixed atom method.

gap for the Γ valley is $E_\Gamma(x) = 3.315 - 7.316x + 3.715x^2$, where x is the Sn content (Fig. 3.13). On the other hand, the VCA calculation gives the band gaps for L, X and Γ valleys as $E_L(x) = 1.768 - 2.549x + 0.925x^2$, $E_X(x) = 1.244 - 0.691x + 0.100x^2$, and $E_\Gamma(x) = 3.042 - 5.588x + 2.193x^2$, respectively. Therefore, the VCA predicts the indirect-to-direct band gap transition in the relaxed $Si_{1-x}Sn_x$ when the Sn content exceeds approximately 0.55, while the (more accurate) mixed atom method does not show any such transition.

This finding may be contrasted to the indication given in the recent work [63] that the direct-indirect crossover in SiSn occurs at approx 25% Sn. This was reached using the LDA and (in contrast to the calculation, used in this chapter) accounting for the atomic position relaxation, but in order to overcome the well-known LDA shortcomming in the bandgap prediction the "scissors" correction [64] was employed, which itself brings in a degree of uncertainty. It is therefore fair to conclude that the question of the direct band gap in SiSn alloy is still open.

3.5 Conclusion

Using local density functional theory and the self-consistent pseudo-potential plane wave method some important properties of GeSiSn alloys, relevant for optoelectronic applications were explored. In particular, relaxed $Ge_{1-x}Sn_x$ alloys, strained Ge grown on relaxed $Ge_{1-x-y}Si_xSn_y$ alloys, strained $Ge_{1-x}Sn_x$ grown on relaxed $Ge_{1-y}Sn_y$ alloys and relaxed Sn_xSi_{1-x} alloys were studied. These were modelled by the mixed atom method, the accuracy of which proved to be far better than that of the virtual crystal approximation, using the available experimental data for comparison. Band structure calculations show that relaxed $Ge_{1-x}Sn_x$ alloys have an indirect-to-direct band gap cross-over at a Sn content of ≈ 0.17, with the bowing parameter equal to 2.49 eV. Furthermore, calculations for strained Ge on relaxed $Ge_{1-x-y}Si_xSn_y$ ternary alloys, and for strained $Ge_{1-x}Sn_x$ grown on relaxed $Ge_{1-y}Sn_y$ alloys, give the range of the substrate compositions and Sn content which lead to direct band gap materials. In contrast, within the mixed-atom approach the Sn_xSi_{1-x} alloys never show a finite direct band gap (while the VCA calculation does predict it).

Chapter 4

Electronic structure and optical properties of Sn and SnGe quantum dots

4.1 Introduction

Self-assembled Sn quantum dots embedded in Si have been successfully grown in recent years, and it was anticipated that these would also be important nanostructures for optoelectronic devices, because of their potential for synthesis of a Si-based direct bandgap semiconductor, a property not found in the more conventional Ge and SiGe quantum dots. Although bulk Sn is a direct zero band gap semiconductor, the gap at the Γ point is expected to increase, as a combined result of quantum confinement and strain. Growth of Sn/Si dots by temperature modulated molecular beam epitaxy has been reported. A few nanometres thick epitaxially-stabilized metastable $\mathrm{Sn}_x\mathrm{Si}_{1-x}$ alloy layer with $x = 0.05$ to 0.1 was first grown on Si (001) [65], and then annealed at temperatures between 550 and 800^o C, to form the Sn quantum dots. The process thus differs from the conventional Stranski-Krastanow growth of III/V dots, and is based on a very small equilibrium solubility of Sn in Si (or in Ge), which leads to clusterization of Sn atoms upon annealing the metastable alloy, leaving more or less pure Si around them. Using the Z-contrast cross-sectional high-resolution transmission electron microscopy, the sample was shown to contain dots with diameters in the range of 5-10 nm, located mostly in what was the $\mathrm{Sn}_x\mathrm{Si}_{1-x}$ alloy layer, and very few in Si spacer layer [66]. The shape of these dots was somewhat irregular, but generally cylindrical or lens-like, rather than the conventional pyramidal. However by the high-resolution Z-contrast tomography it was found that dots could be in either the cubic α-Sn (zero-gap semiconductor) or the tetragonal β-Sn (metallic) phase [67]. The α-Sn dots transform into the β-Sn phase, more elongated in one direction, when their diameter exceeds a critical value of about 8 nm. In order to investigate optical properties of the Sn-in-Si dots, the luminescence spectrum was measured by using Fourier Transform Infrared Spectroscopy. It was elucidated that the absorption spectrum starts from about 0.3 eV, with the absorption strength of 8×10^3 cm^{-1}, which was believed to be consistent with direct interband transitions [65]. In contrast, the absorption measurements by Karim *et al.* [68] show a relatively weaker broad spectrum at 0.7–1 eV, but no features around 0.3 eV. Similarly, the α-Sn quantum dots embedded in Ge were realized, with a diameter of 32 nm and 10% size distribution. Fitting the simulations to experimental transmittance spectra has lead to a conclusion that direct interband transitions in Sn dots were indeed observed, with an energy gap of 0.45 eV and an absorption coefficient of 3×10^3cm^{-1} near the bandgap edge [69]. On the other hand, theoretical studies of the electronic structure of Sn-based quantum dots, which should help in understanding the features observed in experiments, are missing. In this chapter, the single-particle states and interband absoprtion in this type of dots are calculated within the framework of envelope function theory. In Sec. 4.2 the theoretical framework is presented. Due to the lack of some of the material parameters for Sn, these were extracted from empirical nonlocal pseudopotentials, as described in Sec. 4.2.3. The results are presented in Sec. 4.3, with special attention devoted to the issue of the nature of the band gap of quantum dot material, which is relevant for optoelectronic devices. Finally, the conclusions are presented in Sec. 4.4.

4.2 Computational method and model

In this section the theoretical model used to calculate the electronic structure and optical properties of Sn and SnGe quantum dots is described. These were assumed to have cylindrical symmetry, being either cylindrical, lens or cone shaped, with diameter (d) and height (h), where $h = d$ was taken for cylindrical, and $h = d/2$ for lens shaped (i.e. hemispherical) dots, while $h = d/2$ and the base angle of 60^o were taken for cone shaped dots, as shown in Fig. 4.1. Although some papers report tetrakaidecahedron or truncated octahedron shapes [67], the simple cylindrically symmetric shapes should suffice in view of the irregularity present in all the observed dots. The strain distribution has been calculated by using the continuum mechanical model, discussed in Sec.2.4.5. The results of strain calculation for cylindrical, lens, and cone shaped Sn dots in Si matrix are shown in Fig.4.2. Clearly, the major part of the strain occurs in the dots, but a smaller amount of strain appears in the surrounding silicon as well. This is because Sn is "softer", i.e. has smaller values of elastic constants (c_{11} and c_{12}, Table 3.2) than silicon, hence the tin lattice deforms by a larger amount in order to accommodate the smaller lattice constant of the "stiffer" surrounding silicon. The calculated strain field components are used in the eight-band $\mathbf{k}\cdot\mathbf{p}$ calculation, already described in the Chapter 2.

The $\mathbf{k}\cdot\mathbf{p}$ calculation requires the parameters describing the bulk band structure of the constituent materials. In nonpolar (Si, Ge, Sn) zincblende crystals these are: Luttinger parameters $\gamma_{1,2,3}$, Kane energy E_p, band gap E_g, spin-orbit splitting Δ_{so}, hydrostatic (a_c and a_v), uniaxial (b) and shear (d) deformation potentials, and A' which describes the remote band effects on the conduction band. For Si and Ge all these are well tabulated in the literature, while the data for Sn are more scarce or completely missing. Therefore, the Sn parameters were extracted from the empirical pseudopotential method (EPM), and those of the values which have been reported previously could also be compared against the values obtained here, for improved reliability, as described

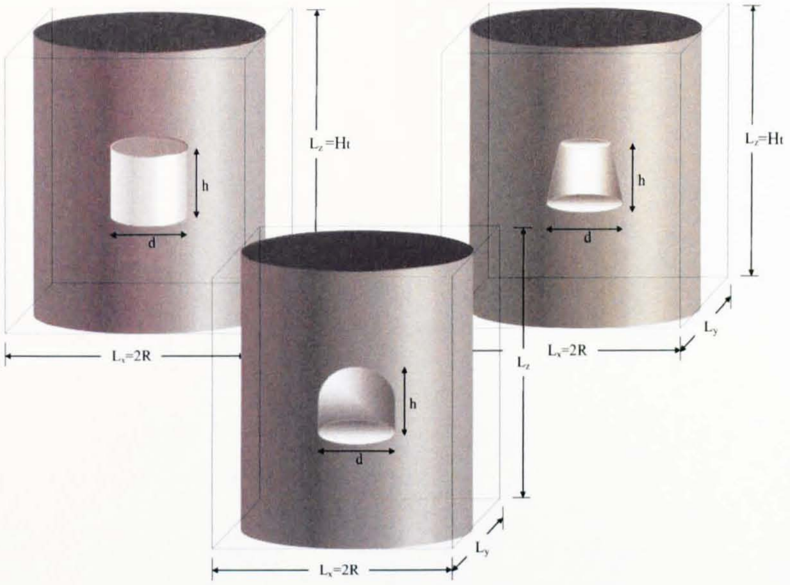

Figure 4.1: Cylindrical, lens and cone shaped quantum dots.

in the next section.

The highest valence band states in Sn dots (just as in almost all other semiconductors except lead chalcogenides) are derived from the Γ point of the bulk Brillouin zone. If the lowest conduction band state also turns out to be at Γ, the Sn dots would be a direct band gap material. The main 'competitor' to these are the states derived from the conduction band at L point, since it is much lower than the X point in Sn. The eight-band **k·p** method cannot *simultaneously* deliver states at the L (a much more elaborate, 30-band **k·p** method [70], or e.g. the pseudopotential calculation [71], would be required for that). In this work, however, the L-valley size-quantized states of Sn dots is found in an approximate manner, using a simple effective mass calculation. For this purpose the scalar, angle-averaged effective mass of the ellipsoidal L valleys is used, only the hydrostatic strain is included, while ignoring higher order effects, like intervalley interference [72] etc., which cannot be simply plugged into an effective mass type of calculation. While not of the same level of accuracy as the **k·p** calculation at Γ, this should still suffice for comparison of direct and indirect gaps in Sn dots. The parameters required were also

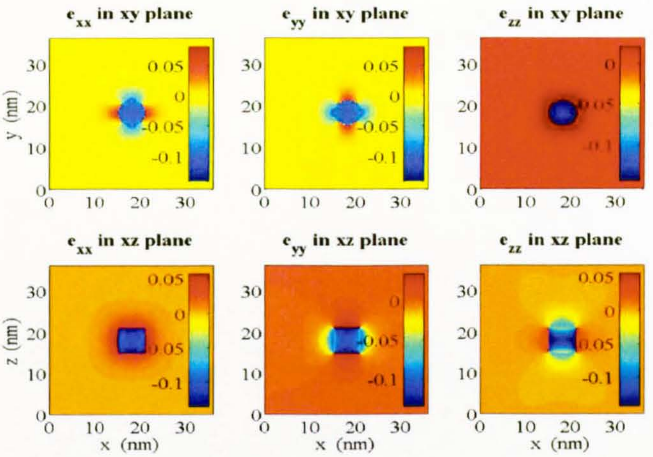

(a) Cylindrical shaped quantum dots

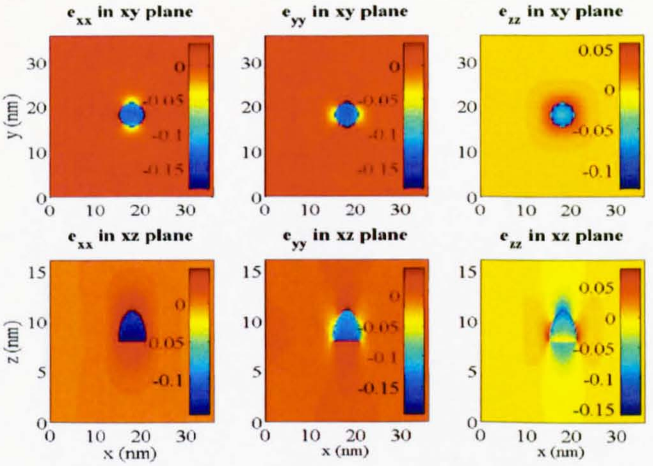

(b) Lens shaped quantum dots

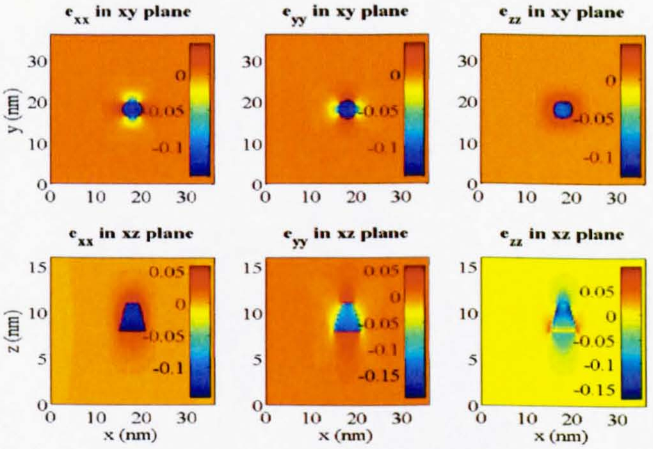

(c) Cone shaped quantum dots

Figure 4.2: Strain distribution in cylindrical, lens and cone shaped Sn quantum dots in Si matrix.

extracted from the EPM calculation described below.

4.2.1 The nonlocal empirical pseudopotential calculation

The band structure of bulk α-Sn was modelled by the nonlocal empirical pseudopotential method [3]. While requiring some experimental input, this method generally offers a better accuracy for various band structure parameters than does the first-principles density functional theory in the local density approximation without any additional schemes like the GW approximation ('G' comes from Green's function and 'W' comes from the screened interaction line) [73] or the "scissors correction", as are employed in total energy approaches (see e.g. Ref. [74] for comparison), and it is exactly these band-structure, rather than ground-state parameters which are of interest in the present work.

For bulk bandstructure calculations one usually uses the discrete set of local pseudopotential formfactors, at exactly those values of **G** which correspond to the equilibrium lattice constant. To extract the deformation potentials, however, one has to consider lattices deformed by uniaxial, shear, or hydrostatic strain, which requires either a continuous local pseudopotential form function $V_\alpha(q)$, or some means of interpolation. The same problem arises in EPM based supercell calculations for superlattices, quantum dots, etc. For Si and Ge, for instance, Friedel et al. [20] have devised such formfunctions, of a modified Falicov form:

$$V_\alpha(q) = \frac{1}{2}\left(\frac{a_1(q^2 - a_2)}{1 + e^{(a_3(q^2 - a_4))}}\right)\left[\tanh\left(\frac{a_5 - q^2}{a_6}\right) + 1\right], \qquad (4.1)$$

where q is the magnitude of the wavevector, and this form, with improved parameters, has subsequently been employed for various calculations, e.g. Refs. [21,75]. Starting with the formfactors for Sn [3], the corresponding formfunction for Sn was devised that reproduces the bandstructure data reported in this and other sources [76–79]. The parameters for Sn, using a cutoff of 8 Ry, which gives almost full convergence, are given in Table 4.1, along with those for Si and Ge, Ref. [21]. The nonlocal and the spin-orbit parts, on the other hand, are already given as continuous functions of the wavevector, and need no further modification for the present purpose.

Parameters	a_1	a_2	a_3	a_4	a_5	a_6
Si	0.1299	3.469	0.7618	3.574	5.0	0.3
Ge	0.2962	2.527	0.6813	1.159	5.0	0.3
Sn	0.1221	2.145	3.100	2.741	5.0	0.3

Table 4.1: Parameters of the pseudopotential of α-Sn (this work), and for Si and Ge, Ref. [21]. The normalization (lattice) volumes for Si, Ge, and Sn are 134.3, 151.8, and 230.5 a.u., respectively.

The band structure of bulk α-Sn along the $L-\Gamma-X$ lines, calculated with these parameters, is given in Fig. 4.4. Near the Γ-point the EPM bandstructure should coincide with that obtained by the $\mathbf{k}{\cdot}\mathbf{p}$ method (since it is the second order perturbation theory applied at the Γ point), with appropriately chosen material parameters, and this can be used to extract these parameters [80]. Fitting of the two band structures (including the cases with strain) was performed here by the simulated annealing algorithm [81], explained later in Fig. 4.3.

4.2.2 Strain effects in the empirical pseudopotential method

The effects of strain in the empirical pseudopotential method have been considered [82,83]. The effect of strain on the energy levels can be separated into hydrostatic and shear strains [84]. The first strain which will be discussed is the hydrostatic strain, corresponding to the deformation potential that is a combination of hydrostatic strain in conduction band (a_c) and hydrostatic strain in valence band (a_v). The hydrostatic strain is a measure of the volume change and causes the valence and the conduction band edge shifts. Hence, it is expressed as:

$$\frac{\Delta V}{V} = \epsilon_{xx} + \epsilon_{yy} + \epsilon_{zz}, \tag{4.2}$$

where $\Delta V/V$ is the relative change of the unit cell volume, and

$$\epsilon_{xx} = \frac{a_x - a_{0x}}{a_{0x}}, \tag{4.3}$$

$$\epsilon_{yy} = \frac{a_x - a_{0y}}{a_{0y}}, \tag{4.4}$$

$$\epsilon_{zz} = \frac{a_x - a_{0z}}{a_{0z}}, \tag{4.5}$$

when a_{0x}, a_{0y}, and a_{0z} are lattice constants at equilibrium in x, y and z direction, respectively. a_x, a_y, and a_z are lattice constants in x, y and z direction, respectively, when the unit cell has been shrunk or enlarged. The hydrostatic strain component leads to a shift of the average valence band energy $\mathrm{E}_{v,av}=(\mathrm{E}_{hh}+\mathrm{E}_{lh}+\mathrm{E}_{so})/3$, i.e. of the average of the energies of the heavy hole, light hole and spin-orbit split-off bands. When pseudomorphic growth of strained layers on a substrate was considered, that have lattice mismatch, it will have two strain components applied on the layers, a biaxial strain ($\epsilon_{\|}$) which is parallel to the plane of the interface and a uniaxial strain ($\epsilon_{\perp}$) which is perpendicular to it:

$$\epsilon_{\|,\perp} = \frac{a_{\|,\perp}}{a} - 1, \tag{4.6}$$

where $a_{\|}$ is the lattice constant of substrate layer in direction of parallel to the interface, a is the unstrained lattice constant, i.e. $\mathrm{a}_{\|}=\mathrm{a}_0$, and ($\epsilon_{\perp}$) which is perpendicular to it.

$$a_{\perp} = a[1 - D(\frac{a_{\|}}{a} - 1)], \tag{4.7}$$

where D is a parameter which depends on the elastic constants of the material and the interface orientation, such as (001), (110) and (111) plane. It is expressed as:

$$D^{001} = 2\frac{c_{12}}{c_{11}}, \tag{4.8}$$

$$D^{110} = \frac{c_{11} + 3c_{12} - 2c_{44}}{c_{11} + c_{12} + 2c_{44}}, \tag{4.9}$$

$$D^{111} = 2\frac{c_{11} + 2c_{12} - 2c_{44}}{c_{11} + 2c_{12} + 4c_{44}}. \tag{4.10}$$

Therefore, the energy level shifts in the conduction band ($\Delta E_c^{\mathrm{hydro}}$) and valence band ($\Delta E_{v,av}^{\mathrm{hydro}}$) are $a_c(2\epsilon_{\|}+\epsilon_{\perp})$ and $a_v(2\epsilon_{\|}+\epsilon_{\perp})$, respectively. The second strain effect is uniaxial strain. The uniaxial contribution couples to the spin-orbit interaction and leads to an additional splitting of the valence band energies. For example in (001) orientation, the energy splitting is expressed as,

$$\delta E^{001,\mathrm{uni}} = 2b(\epsilon_{zz} - \epsilon_{xx}). \tag{4.11}$$

where b is the uniaxial deformation potential parameter. Conduction bands at Γ point are not affected by the shear contribution to the strain. However, energies at L, X and generally around the Γ point are affected.

In pseudopotential calculations of the band structure of the strained system the atomic coordinates are scaled proportionally to the unit cell deformation, the reciprocal lattice vectors **G** are also changed accordingly, and finally the changed volume of the unit cell is used in scaling the pseudopotential form-function.

4.2.3 Extracting the k·p band structure parameters

It should be noted that the (almost) *full* congruence of the empirical pseudopotential method and **k**·**p** band structures can be obtained only in an infinitesimally small vicinity around the Γ-point, while a very good congruence can be achieved in a finite range of **k** vectors around Γ, say 8–10% of the full span of the Brillouin zone (the range where the **k**·**p** method is usually considered accurate), and in this work the latter choice was targeted. The set of parameters for Sn, obtained that way, is given in Table 4.2, together with those for Si and Ge (the later two adopted from Refs. [83, 85]). Finally, the A' parameter values of Si and Ge were found by using the relation for the conduction band effective mass m^* at the Γ point in Eq. 2.97 and the values of $0.528m_0$ and $0.038m_0$ for Si and Ge, respectively [85].

The Luttinger γ parameters are extracted here for Sn by fitting the band structure of Sn, calculated by the **k**·**p** method, and the one obtained by the nonlocal empirical pseudopotential method around the Γ point. The target of the fitting is to find the Luttinger parameters for which the two band structures are the most similar to each other. The "similarity" between the two band structures is quantified via finding the square difference of energies of the corresponding bands at a number of wavevectors in the above range, and adding them together to get a single scalar measure of "similarity". In other words, this process is the minimization of the difference of the band structures. The algorithm which was used is the simulated annealing method [81], based on Monte Carlo simulation, because it is an effective solution method of combinatorial optimization problems, i.e. finding global minimum point. Firstly the Luttinger parameters are set randomly. Each parameter then can be changed to a new value and this will be accepted if the difference between the band structures, calculated from the new values of the Luttinger parameters, is smaller. If the new values cause the difference to increase, then they still may be accepted with some probability, depending on the difference between the two band structures and on a global time-varying parameter T called the temperature. With this condition, the simulated annealing method can find the global minimum, not just local minimum. The procedure is illustrated in Fig. 4.3.

The parameters, shown in Table 4.2, are considerably different from those given in Ref. [76]. However, the effective masses for heavy holes which follow from the two sets are very similar (0.2 in the [001] direction, and 0.55–0.59 in the [111] direction). For light electrons these parameters give the effective masses of 0.018–0.019, and those from Ref. [76] are 0.035–0.039, i.e. differing by a factor of two. However, the experimental values for the latter (Table V in Ref. [76]) are around 0.024, which is much closer to calculated value (not unexpected, since a more empirical-related method of band structure calculation was used). Therefore, there are reasons to believe that the other parameters for Sn, reported here, are also reasonably reliable. It should also be noted that the conduction and valence band hydrostatic deformation

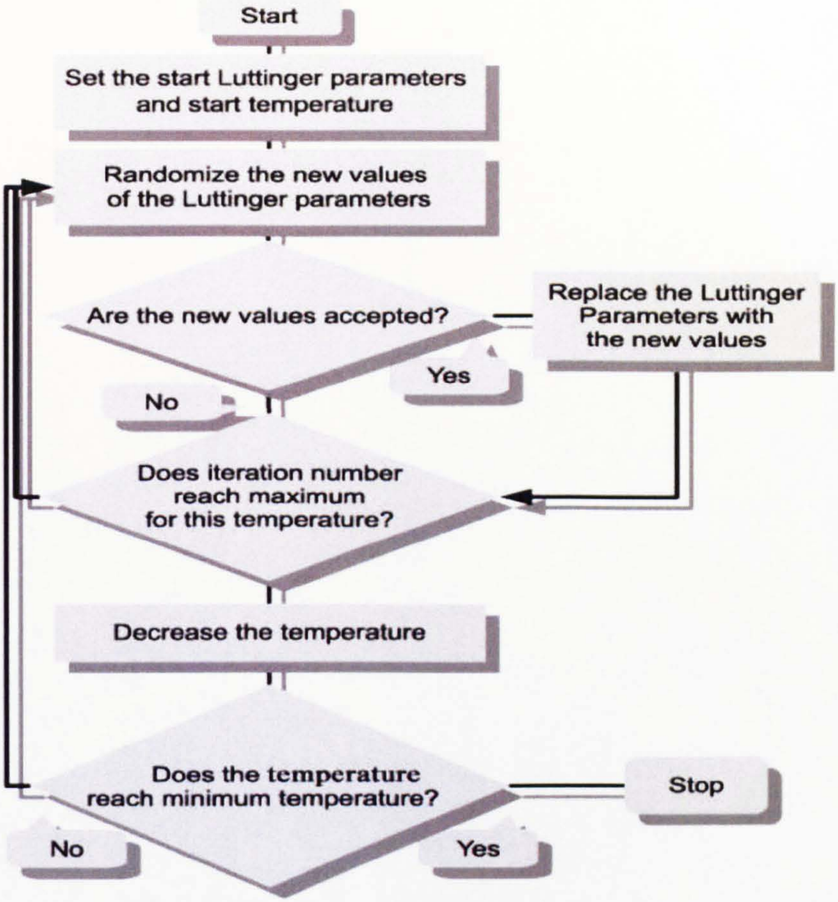

Figure 4.3: Diagram shows the algorithm of the simulated annealing method.

potentials, a_c and a_v, were individually determined by setting the energy at Γ_8^+ (heavy hole and light hole band) for zero value of the hydrostatic strain, $\epsilon = \epsilon_{xx} + \epsilon_{xx} + \epsilon_{xx} = 0$, as the constant reference energy, and then applying strain to find $a_c = \left(\Gamma_7^-(\epsilon) - \Gamma_8^+(\epsilon = 0)\right)/\epsilon$, and $a_v = \left(\Gamma_8^-(\epsilon) - \Gamma_8^-(\epsilon = 0)\right)/\epsilon$.

As for the L-valley parameters, the longitudinal (m_l) and transverse (m_t) effective mass are found to be $1.99m_0$ and $0.091m_0$, respectively, in good agreement with other published values $1.35m_0$, $1.48m_0$ and $0.072m_0$, $0.075m_0$, respectively [76, 89], and a value of -5.24 eV was extracted for the hydrostatic deformation potential.

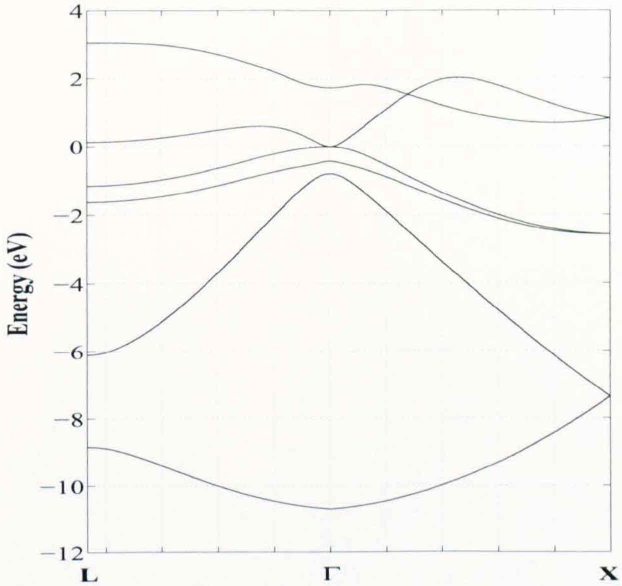

(a)

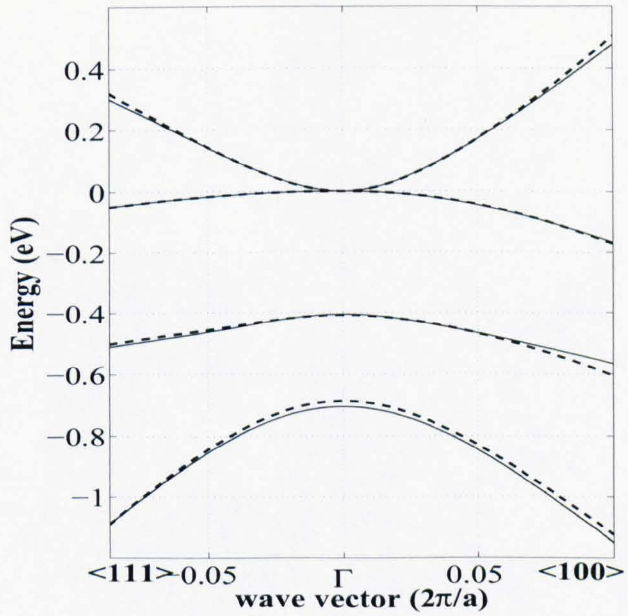

(b)

Figure 4.4: a) The EPM calculated band structure of bulk α-Sn, and (b) the band structure near the Γ point, calculated by the eight-band $\mathbf{k} \cdot \mathbf{p}$ method with the obtained parameters (dashed), compared to the band structure calculated by EPM (solid lines).

	Value(unit)			
Parameter	Sn (this work)	Sn (other sources)	Si	Ge
γ_1	-25.19	-12.0$^{a)}$,-14.97$^{b)}$,-19.2$^{c)}$	4.285	13.38
γ_2	-15.11	-8.45$^{a)}$,-10.61$^{b)}$,-13.2$^{c)}$	0.339	4.24
γ_3	-13.53	-6.84$^{a)}$,-8.52$^{b)}$,-9.0$^{c)}$	1.446	5.69
E_p	14.26 eV	23.8$^{b)}$ eV	21.60 eV	26.30 eV
A'	-3.25		-4.285	-7.519
a_c	-8.714 eV	$a_c + a_v$=-7.04$^{a)}$	1.98 eV	-8.24 eV
a_v	1.62 eV		2.46 eV	1.24 eV
b	-2.01 eV	-2.3$^{d)}$	-2.1 eV	-2.9 eV
d	-0.39 eV	-4.1$^{d)}$	-4.8 eV	-5.3 eV
Δ	0.70 eV	0.72$^{a)}$,0.77$^{b)}$ eV	0.044 eV	0.29 eV
E_g	-0.408 eV	-0.406$^{a)}$-0.413$^{b)}$ eV	4.185 eV	0.898 eV

Table 4.2: The $\mathbf{k}\cdot\mathbf{p}$ and deformation potential parameters for bulk α-Sn, Si and Ge. (*a*) - Ref. [76], *b*) - Ref. [86], *c*) - Ref. [87], *d*) - Ref. [88].)

The final ingredient required for the $\mathbf{k}\cdot\mathbf{p}$ calculations of heterostructures is the valence band offset at the interface. In the absence of any more reliable experimental data, for Sn grown on $\mathrm{Si}_x\mathrm{Ge}_y\mathrm{Sn}_{1-x-y}$ an expression in accordance to Jaros [90] has been used, i.e. $\Delta V_{v.b.} = 1.17 \cdot x + 0.69 \cdot y$ [eV]. The band energies on the absolute energy scale are not intrinsically contained in the pseudopotential formfactors, and therefore cannot be obtained within the EPM.

4.3 Results and discussion

Using the methods and materials parameters described above, the electronic and optical properties of the Sn-based quantum dots, in particular Sn quantum dots embedded in Si [91], and the $\mathrm{Ge}_{1-x}\mathrm{Sn}_x$ alloy dots were furthure investigated. To check the validity of the method test calculations for lens shaped

Ge quantum dots in Si, with the diameter and the height of about 100 and 15 nm, respectively, were first performed. The direct interband transition onset is about 1.3 eV, and the indirect transition (towards the L-point) onset is about 0.72 eV. This is in good agreement with the experimental results of absorption spectrum of the self-assembled Ge/Si quantum dots grown by a solid-source molecular beam epitaxy, in the Stranski-Kranstanov growth mode [92], where a broad peak at 0.7 to 1.0 eV was found.

4.3.1 Sn quantum dots

The electronic structure of Sn dots in Si was calculated assuming they were either cylindrical, lens or cone shaped. While the actually grown dots were approximately cylindrical, it is plausible to expect that the other two shapes might be achieved starting with a graded, rather than uniform-composition, Sn-Si alloy layer, which is then annealed. The Sn/Si interface has type-I band alignment, i.e. the Sn dot is the potential well for both electrons and holes at the Γ point. Examples of the wave functions of the lowest (topmost) three states in the conduction (valence) band at Γ are given in Fig. 4.5. The direct-transition absorption spectrum for a couple of dot sizes, for the three shapes, is shown in Fig. 4.6. As expected, the transition energy inversely depends on the dot size, and also depends on the dot shape in the expected manner, being shifted to somewhat higher energies for lens and cone dots. Interestingly, the dot shape determines whether the z-polarized or in-plane-polarized light would be more strongly absorbed.

The main feature from these calculations is that the direct absorption spectrum of Sn/Si dots peaks around 2–2.5 eV. This is larger than the indirect absorption onset in bulk Si (matrix), at about 1.1 eV, but since this absorption is relatively weak one can still expect that these direct transitions might be observed in very thin layers of Si containing Sn dots. It is quite a surprising result that the direct transition energies are so large. This is because of the very large strain in Sn, so large, in fact, that is has converted a zero-gap material

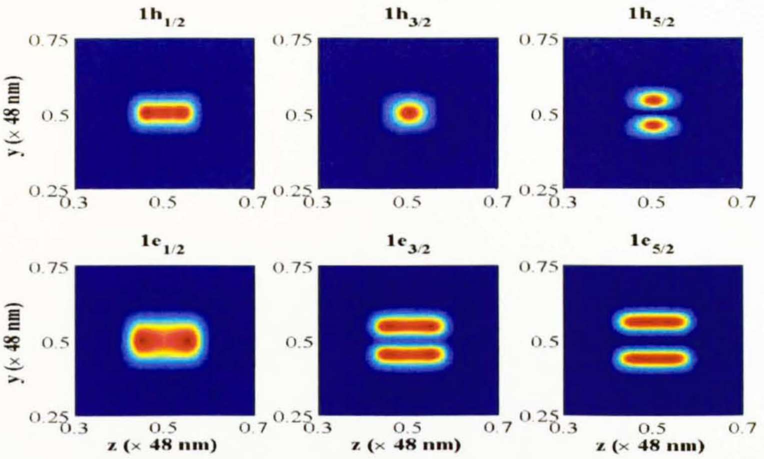

(a) Cylindrical shaped quantum dots

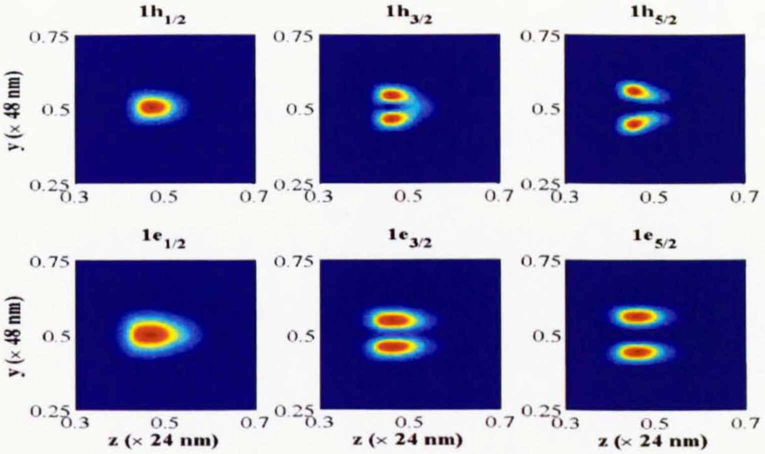

(b) Lens shaped quantum dots

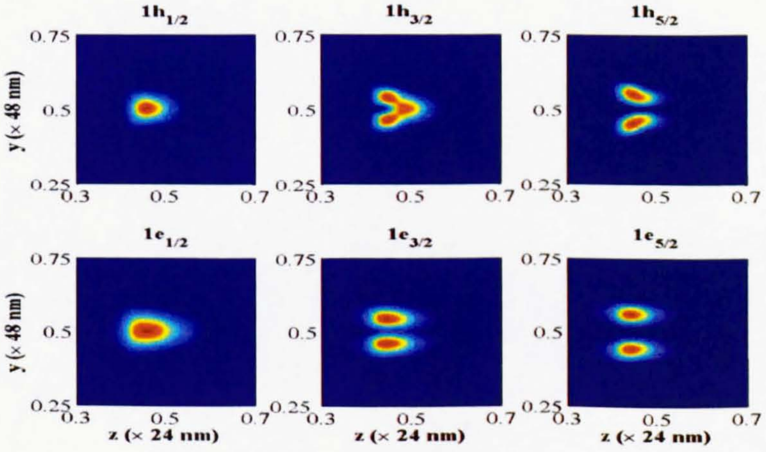

(c) Cone shaped quantum dots

Figure 4.5: The wavefunctions squared of a couple of conduction and valence quantized states in 8 nm diameter Sn/Si quantum dots of cylindrical, lens and cone shape.

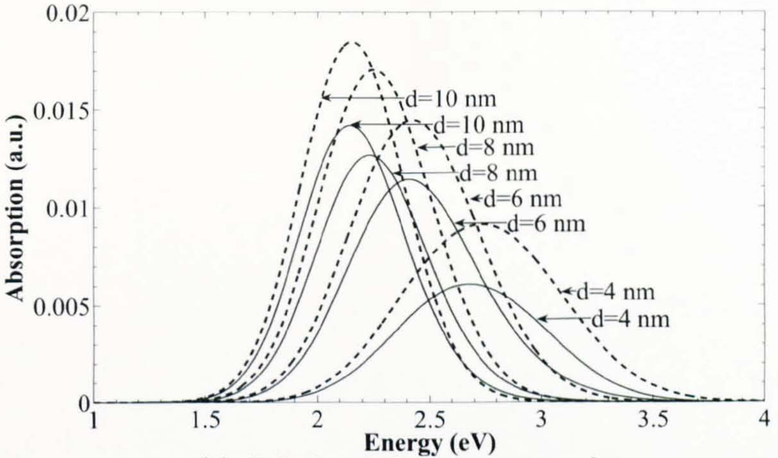

(a) Cylindrical shaped quantum dots

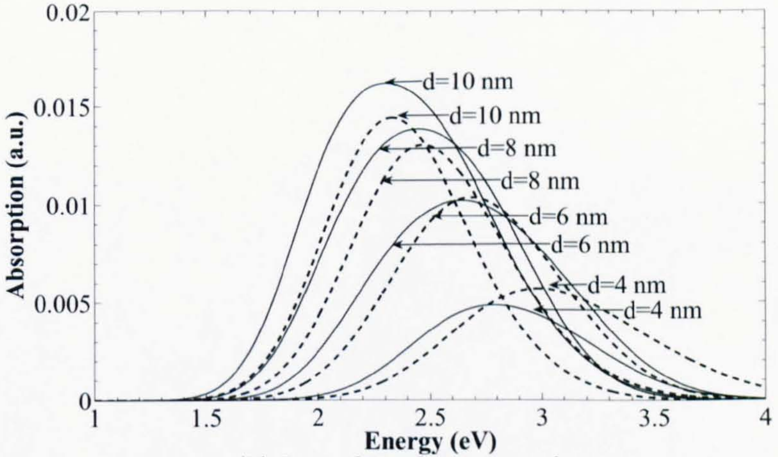

(b) Lens shaped quantum dots

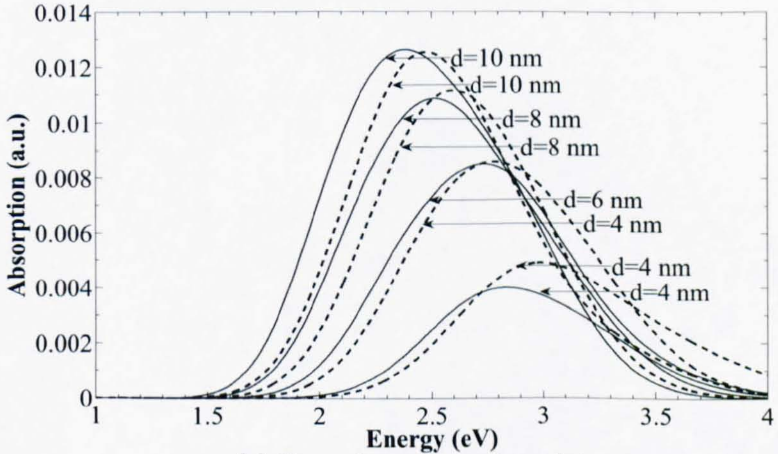

(c) Cone shaped quantum dots

Figure 4.6: The direct interband absorbtion spectra of Sn/Si quantum dots of cylindrical, lens and cone shape, for different dot diameters d. Solid lines correspond to z-polarized light (along the dot axis), and dashed lines to in-plane polarized light.

into an almost wide-bandgap semiconductor.

However, calculation of L-valley quantized states (the band alignment is here also type-I) shows that these states are much lower in energy than the conduction band states at Γ, as shown in Fig. 4.7, hence the Sn/Si quantum dots are not a direct gap material. This is a consequence of the fact that the absolute value of L-valey hydrostatic deformation potential is much smaller than that of the Γ valley. Therefore, the effects of strain change the arrangement of Γ and L-valley states. The photoluminescence peak at approx. 0.7 eV, observed in Ref. [68] in Sn dots with the diameter of about 5 nm, agrees very well with the indirect transition energy predicted here, which indicates that it is actually this (indirect and weak) transition that was observed. The likely mechanism for this was the photogeneration of electrons in the X valley of the Si matrix, followed by their capture into lower lying L states of Sn dots, and then by the indirect, phonon-assisted recombination.

4.3.2 Sn_xGe_{1-x} quantum dots

Previous studies of Si-Ge-Sn bulk alloys [4,50,66,93–95] show that a direct gap material can be obtained in a suitable range of $Ge_{1-x}Sn_x$ alloy compositions, so the electronic structure of $Ge_{1-x}Sn_x$ quantum dots embedded in Si was also calculated. Clearly, such dots cannot be grown in Si in the same way as Sn dots are, because Ge is completely soluable in Si, in contrast to Sn. However, growth of $Ge_{1-x}Sn_x$ quantum dots *on* [111] oriented Si substrate, rather than *in* Si matrix, has been recently reported [96,97]. The dots are approximately hemispherical in shape, they are covered by SiO_2, and are asserted to have a coherent interface with the underlying Si, and are therefore strained. It is less clear, however, what strain conditions apply towards the 'upper' interface with SiO_2, since it even has a different crystalline structure. The strain conditions are important in Sn based dots, as shown above, but are difficult to resolve in the case of Si/$Ge_{1-x}Sn_x$/SiO_2 dots. Furthermore, the different crystalline structures of Sn and SiO_2 would discourage one to use the $\mathbf{k}\cdot\mathbf{p}$ method at all, but the fact that the band discontinuities between Sn and SiO_2 are very large effectively makes it irrelevant what is on the other side of Sn, and the **k**·**p** method can still be used to a good accuracy. Overall, one can still expect that the calculation for $Ge_{1-x}Sn_x$ quantum dots fully embedded in Si, with their axis in the [001] direction, as was performed in this work, is an approximate description of the actual structure.

In these calculations the Luttinger parameters, deformation potentials and the spin-orbit splitting of $Ge_{1-x}Sn_x$ were estimated using Vegard's law, while the direct band gap and lattice constant were calculated by using the quadratic interpolation, with bowing parameters of 2.49 eV [4, 51, 93] and 0.166 Å [60], respectively. The results for the dot sizes between 4 and 12 nm, and for different compositions $0 \leq x \leq 1$, show that the indirect interband transitions (towards the L valley states) occur from 0.8 to 0.4 eV, while the direct interband transition occurs from 2.5 to 1.5 eV, as also shown in Fig. 4.7(b), implying that they are indirect gap materials. The direct energy band gap depends quadratically on the Sn composition, because the bowing parameter in the direct band gap of the alloy has a strong influence. Experimentally, for dots of small diameters (<10 nm) the absorption peaks between 1.5 eV and 2 eV were found [96], which agrees very well (perhaps surprisingly so, in view of the approximations involved) with the data for direct transitions given in Fig. 4.7(b). Nevertheless, these dots are (predicted to be) an indirect band gap material.

Finally, the calculations were also made for Sn dots embedded in Ge, which can be fabricated in the same manner as Sn/Si dots, due to the small solubility of Sn in Ge. Here one has the type-II alignment (after the strain), i.e. the dot is the potential well only for holes, but not for either Γ or L-valley electrons. The conduction band edge at L is well below that at Γ inside the Sn dot, since it is largely determined by strain, and this does not change too much when going from Si to Ge matrix. This in turn implies that Sn dots in a Si_xGe_{1-x} matrix (which presumably could also be grown by the same technique) cannot

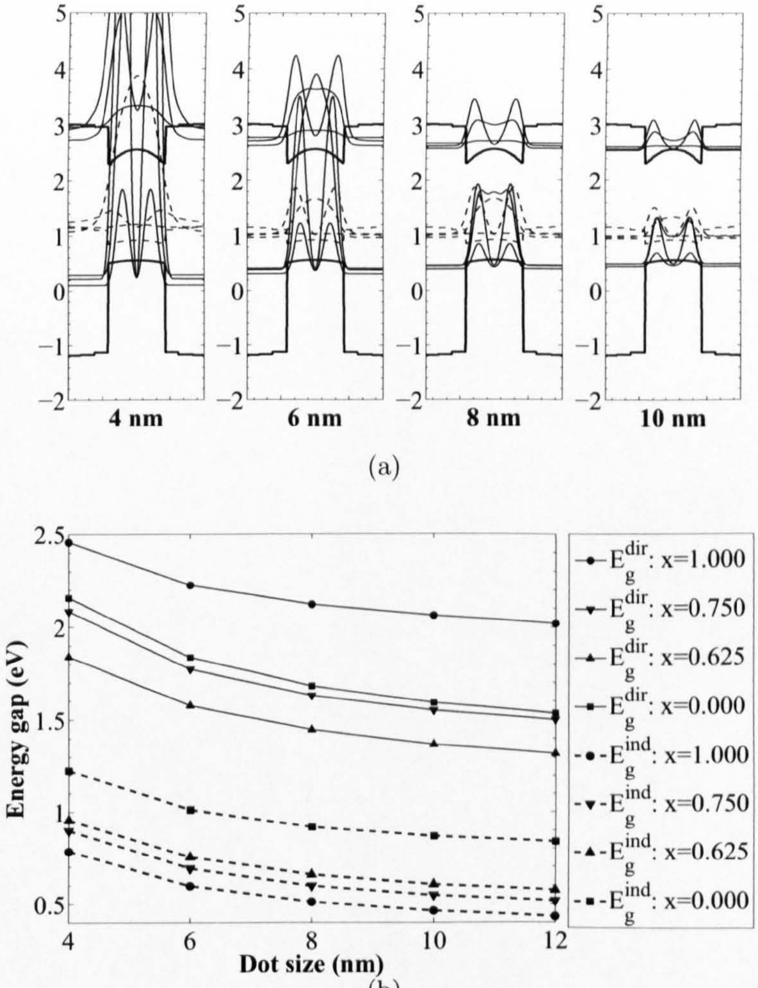

(a)

(b)

Figure 4.7: (a) The wavefunctions squared along the axis of Sn/Si dots with diameters from 4 to 10 nm, for the quantized states at Γ (solid) and at L point (dashed); (b) The dependence of the band gap of $Ge_{1-x}Sn_x$/Si dots on the diameter and composition x.

become a prominent direct gap material for any value of x.

4.4 Conclusion

Using the nonlocal empirical pseudopotential method to extract the $\mathbf{k}\cdot\mathbf{p}$ parameters and deformation potentials of bulk Sn, and the 8×8 $\mathbf{k}\cdot\mathbf{p}$ method to calculate the electronic structure and optical properties of quantum dots, the properties of self-assembled Sn dots embedded in Si, and $Ge_{1-x}Sn_x$ quantum dots in Si or in Ge, relevant for optoelectronic applications were explored in detail. Cylindrical, lens and truncated cone shaped dots were considered. The self-assembled Sn/Si dots of size between 4 nm and 12 nm were found to have indirect interband transitions (towards the L-valley size-quantized states) from 0.8 to 0.4 eV, and direct interband transitions from 2.5 to 2.0 eV. The indirect interband transition energies compare very well with the reported experimental absorption peaks [68]. However, the indirect nature of the lowest interband transition makes Sn or SnGe quantum dots in a Si matrix the unlikely candidates for optoelectronic devices, except perhaps for pure absorption applications, in contrast to some previous expectations.

Chapter 5

SnGe asymmetric quantum well electro-absorption modulators for long-wave silicon photonics

5.1 Introduction

The last two decades have witnessed the widespread use of optoelectronic devices in many areas, such as the telecommunications, computers and entertainment industries. In order to achieve the high speed of data transfer in electronic equipment, the idea of integration of optical and electronic devices, together on a silicon platform, was introduced and comprehensive experimental and theoretical investigations in this direction have been made. These include the possibility of using direct bandgap materials based on the alloys of group IV elements Si, Ge, and Sn (including the binary $\mathrm{Ge}_{1-x}\mathrm{Sn}_x$ and ternary $\mathrm{Ge}_{1-x-y}\mathrm{Si}_x\mathrm{Sn}_y$ material) which are cheap, atoxic, and generally compatible with silicon technology, e.g. [93–95, 98, 99]. For instance, by employing a special class of $\mathrm{Ge}_{1-x-y}\mathrm{Si}_x\mathrm{Sn}_y$ alloys on Ge buffered Si substrate, the lattice constant of the ternary can be tuned to be identical to that of Ge, and the system shows a tunable direct bandgap of 0.8-1.4 eV [100]. The system is promising for a range of applications, as diverse as high efficiency solar cells, interband injection lasers, intersubband quantum cascade lasers, etc. [100–102]. The $\mathrm{Ge}_{1-x-y}\mathrm{Si}_x\mathrm{Sn}_y$ ternary alloys moreover, can be used as higher-gap barrier layers in strain-free Ge/SiGeSn quantum well optical modulators [103].

This type of modulator offers a high modulation efficiency and small size. To achieve good performance this is likely to be based on asymmetric coupled double quantum wells (ADQWs) [104–108]. By increasing the amount of Sn in the GeSn alloy composition the direct band gap decreases, which is of interest in long wavelength silicon technology applications, such as for chemical and biological agents detector, infrared detector and Longwave Integrated Optoelectronics (LIO) [6]. The existing electro–optic (EO) modulators within Si technology, normally rely on the refractive index modulation by injection of free carriers in Si waveguide comprising a pin-diode or a MOS capacitor, e.g. [109] These are longer devices, usually in the Mach-Zehnder configuration, but can cover a broad range of wavelengths, including mid-infrared. In contrast, the Stark effect based EO or electro-absorption (EA) modulators are far more wavelength-specific but, if operated in the electro-absorption regime, can be very short, of the order of 1 μm, and potentially much faster. Alternatively, they can also be operated as EO modulators, below the absorption threshold, and then can accept a somewhat wider range of wavelengths, while requiring an increased length. In this chapter the possibilities of employing the SnGe alloy based multiple quantum well (MQW) structures for EA modulators in the mid-infrared wavelength range are considered. Therefore, theoretical studies of the electronic structure of $\mathrm{Ge}_{1-x}\mathrm{Sn}_x$ asymmetric double quantum wells, which should help in designing the structure of a desirable electronic modulation device, would be important and interesting area. In this work, the asymmetric double quantum well structures which have a strong electric field sensitivity, i.e. to have a large quantum confined Stark effect, are designed within the framework of the 8–band $\mathbf{k}\cdot\mathbf{p}$ method. Asymmetric double quantum wells (ADQWs) are optimized to exhibit maximum optical modulation sensitivity by varying the barrier width, barrier position, and well width. Desirable Sn compositions of each layer are investigated in order to have interband transition energies in the photon wavelength ranges of interest. The electronic structure, optical properties, i.e. the absorption coefficient, are calculated. In Sec. 5.2

the computational method and model are presented. In Sec. 5.3, the results of this study are shown. Finally, the conclusions are presented in Sec. 5.4.

5.2 Design considerations and calculation

The SnGe alloys have a relatively small band gap (less than that of Ge, and decreasing as the Sn content increases), and this can be modified by strain. In unstrained material the indirect gap, towards the L valley, is smaller than the direct gap for low tin content, the crossover taking place at ~15-20 % Sn. In tensilely strained material the crossover happens earlier, and for compressive strain it requires a larger content of Sn, but such alloys are progressively more difficult to make. In any case, the direct and indirect gaps do not differ too much, typically by 0.2 eV or less. Supercell based (i.e. without the virtual crystal approximation) calculations using the empirical pseudopotential method [99], give the (fitted polynomial) expression for the direct band gap of unstrained $\mathrm{Sn}_x\mathrm{Ge}_{1-x}$ in Sec. 3.4.1, and for strained $\mathrm{Sn}_x\mathrm{Ge}_{1-x}$ (grown on $\mathrm{Sn}_y\mathrm{Ge}_{1-y}$ substrate) in Sec. 3.4.3. The small band gap suggests the possibility of using these materials for mid-infrared EA modulators. A specific feature of the SnGe material system, when used with different Sn content for the well, barrier and substrate layers in quantum well type structures, is that the conduction band bottom and the valence band top are both positioned in the material with the largest content of Sn. Given that the well material has to be either tensilely strained or at most unstrained, in order to have a direct band gap, the content of Sn in the substrate would have to be equal to or larger than that in the well, and therefore even more so than the Sn content in the barrier. This in turn implies that: (i) with both the well and barrier layers being tensilely strained, it is not possible to achieve a strain-balanced structure with arbitrarily large number of layers; (ii) given that there is some size-quantization energy, for electrons and for holes, in the QW part, the effective band gap therein is somewhat larger than in the well material itself (although the tensile strain will decrease it from the value in relaxed material), and this is then larger than the band gap of the substrate. The former feature may not be detrimental if one needs just a few wells in the structure, below the critical thickness for this system. The latter is more difficult to accept because the substrate, having the lowest (and direct, at that) band gap will absorb the radiation that should be modulated by the quantum well stack. Since the substrate must be much thicker than the MQW, in order to enforce its own lattice constant across the structure, its absorption will also be large, considerably increasing the insertion loss of the modulator. Both the above issues can be circumvented if one uses compressively strained material for the wells, and tensilely strained for the barriers, so that the overall structure can be made strain-balanced by appropriate choice of the substrate composition in between the values in the well and the barrier. It then becomes possible to have a larger-bandgap, nonabsorptive substrate, provided the size–quantization energies are not too large. On the downside, the compressively strained well material is almost certain to have an indirect band gap. Overall, this type of structure is still potentially useful for EA modulators, because the indirect absorption is normally much smaller than the direct one. In single-crystal bulk Ge, for instance, the indirect absorption coefficient amounts to a few tens of cm^{-1} before the onset of a much stronger direct absorption of $\sim 10^4$ cm^{-1}, e.g. [110]. This should be fully acceptable because the EA modulator ideally switches on and off the (significant part of) the large direct interband absorption, hence is short and the indirect absorption losses are small. Indeed, the strain-balanced Ge/SiGe MQW modulator described in [111] operates on direct transitions in Ge wells, and tolerates the indirect absorption towards the lower-lying L-valley states. It should be noted, however, that the residual absorption, below the direct absorption threshold, in the MQW structure described in [111] was much larger than in the bulk (about 500 cm^{-1}), i.e. only (or still) one order of magnitude smaller than the direct absorption. It is not certain whether all of this comes from indirect transitions (or could perhaps be partly attributed to scattering etc., and would then exist even in direct-gap material), but even this larger residual absorption should not excessively degrade the EA modulator performance, although it does increase the insertion loss. The presence of L-valley states is much more important in the proposed Ge/SiGeSn interband lasers because of their ability to store a part of the electron population and make it optically inactive [101], but this is irrelevant for EA modulators.

Since the materials involved in an EA modulator have a relatively small band gap, a proper description of the electronic structure and optical properties requires the 8-band **k**·**p** method with the effects of strain included. Relying on the shift of subband spacing with varying external electric field, EA modulators can comprise either symmetric or asymmetric QW structures. However, in the former case the (always red) shift is initially slow, i.e. quadratic with the field strength. Although this can deliver useful modulation, as e.g. in [111], asymmetric structures are generally considered advantageous as being more (i.e. initially linearly) sensitive to the field. Within this latter class, asymmetric double coupled QWs are a very good choice, requiring just two different material compositions and offering a large shift of transition energy and sufficiently large optical transition matrix elements, which is why these are chosen for further consideration in this work. The alternative, asymmetric step QWs require three different material compositions, which is a setback for purely technological, rather than fundamental reasons. In this layered system there exists biaxial strain, with the lateral lattice constant $a_{\|}$ in all layers being equal to that of the relaxed $Ge_{1-z}Sn_z$ substrate, and the lattice constant in the perpendicular direction of each layers is calculated by Eq. 3.23.

The electron and hole states in the structure are calculated using the 8-band **k**·**p** method, which accounts for the conduction band Γ_7^- and the three valence bands Γ_8^+ (heavy hole and light hole band) Γ_7^+ (spin-orbit band), and includes the strain dependent coupling and shifts of these bands.

In calculating the absorption in layered structures, with the in-plane wave vector being a good quantum number, one normally defines a mesh in the $k_x -$

k_y plane and adds the contributions from all electron-hole transitions between size–quantization (subband) states having their (k_x,k_y) values at the chosen mesh points. Alternatively (although this does not appear to have actually been done in the literature), it is possible to use the plane wave type solutions in the cylindrical coordinate system, the state counters then being two quantum numbers that describe the in-plane free motion in cylindrical coordinates. the previously developed 8-band **k·p** code for cylindrical quantum dots [31] was appropriately modified, and the MQW structure was considered as a cylindrical quantum dot with a very large diameter d, and compositionmodulated in the z-direction, as shown in Fig. 5.1 for the case of asymmetric double coupled quantum well.

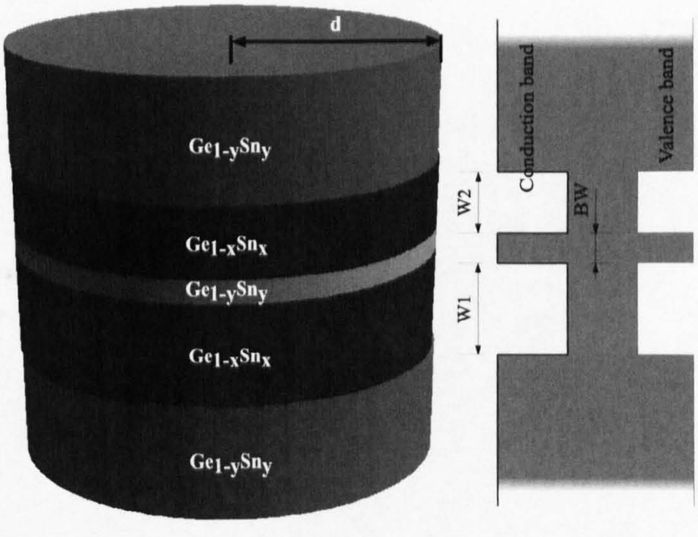

Figure 5.1: Asymmetric double quantum well structure, considered for computational purposes as a very large diameter cylindrical quantum dot, comprising two wells of widths W1 and W2, separated by a thin barrier of width BW, all embedded in a much thicker barrier material.

The summation over the dense in-plane spectrum of states was effectively performed as a summation over the radial and angular quantum numbers describing the in-plane states in the dot.

The **k·p** and strain parameters required for the calculation for Sn are given in Ref. [93], and were extracted by fitting to the energy band structure found by the nonlocal EPM [3], and the valence band discontinuity at heterointerfaces were taken in accordance with [90]. The material band gap was taken according to the expressions from Ref. [93]. The expression, $E_\Gamma(x, y) = 0.782 - 1.483x - 2.577y + 8.216xy - 1.653x^2 - 1.866y^2$, where x and y denote the Sn content in strained $Ge_{1-x}Sn_x$ layer and in relaxed $Ge_{1-y}Sn_y$ substrate, respectively, appears to describe the band gap at room temperature, although it was not derived for that purpose, because the limiting case of unstrained pure Ge (the direct gap of which shrinks from $\sim$ 0.88 eV at 0 K to $\sim$ 0.80 eV at 300 K) is reproduced quite well.

The quantity which naturally describes the optical absorption in a quantum dot structure is the absorption cross section of a transition, and the corresponding parameter for the MQW structure–the fractional absorption–is then obtained by dividing the optical cross section by the dot base area. (By further dividing this by whatever is considered to be the effective thickness of the structure, one can get the formal absorption coefficient, but the results in this work are given in terms of fractional absorption.) Finally, as usual in calculations of the continuum performed via discretization, the delta function in Fermi's Golden rule is replaced by a Gaussian with an appropriately chosen standard deviation, to overlap the neighbouring mesh points (here the typical spacing between various in-plane states).

Both the perpendicular (z-polarized) and in-plane (x- polarized) light can be absorbed, depending on the character of the subbands involved. The interband absorption, between the conduction and valence subbands, was calculated as described in [31].

5.2.1 Exciton energy calculation

Although more elaborate schemes for including the excitonic effects in calculations of the EO modulator absorption spectrum have been previously used, e.g. [107], a much simpler approximate method was used here: this handles the variational function that modulates the product of wavefunctions of the two size-quantized states involved [29, 112, 113]. Although sometimes perceived as being the effective mass approximation (which it frequently is, when considering the light-hole and heavy-hole excitons separately), the method can actually accept an arbitrary mixture of basis states in the two subbands, as found by the **k**·**p** method, but neglects the in-plane wave vector dependent basis state composition of the two subbands, as well as an admixing of more remote subbands. The variational approach [113] to the exciton energy calculation was implemented by using the trial function as follows:

$$\mathbf{\Psi}\left(\mathbf{r}, z_e, z_h\right) = \psi_e\left(z_e\right)\psi_h\left(z_h\right)\phi_{eh}\left(r\right), \tag{5.1}$$

$$\phi_{eh} = \sqrt{\frac{2}{\pi}\frac{1}{\lambda}}\exp\left(-\frac{r}{\lambda}\right), \tag{5.2}$$

$$r = \left|z_e - z_h\right|, \tag{5.3}$$

where $\phi_{eh}\left(r\right)$ is the two-dimensional exciton envelope function, $\psi_e\left(z_e\right)$ and $\psi_h\left(z_h\right)$ are electron and hole envelope functions, respectively, z_e and z_h are the coordinates, which are perpendicular to the quantum wells plane, of electrons and holes, respectively, and λ is variational parameter. Then, the binding energy of the exciton, including the kinetic energy and potential energy, is dependent on the variational parameter, which is expressed as [113]:

$$E_B = E_{KE} + E_{PE}, \tag{5.4}$$

where

$$E_{KE} = \frac{\hbar}{2\mu^*}\frac{1}{\lambda^2}, \tag{5.5}$$

$$E_{PE} = \frac{1}{4\pi\varepsilon_0}\frac{e^2}{2\pi\epsilon^*\lambda}\int dz_e\int dz_h\left|\psi_e\left(z_e\right)\right|^2\left|\psi_h\left(z_h\right)\right|^2 G\left(r\right), \tag{5.6}$$

$$G\left(r\right) = \frac{2r}{\lambda}\left[\frac{\pi}{2}\left[H_1\left(\frac{2r}{\lambda}\right) - N_1\left(\frac{2r}{\lambda}\right)\right] - 1\right] \tag{5.7}$$

where $H_1(x)$ is the first-order Struve function and $N_1(x)$ is the first-order Neumann function, μ^* is the effective reduced mass for exciton and ϵ^* is the effective dielectric constant. Therefore, the exciton binding energy can be calculated by varying the variational parameter λ in order to minimize E_B, as displayed in Fig.5.2.

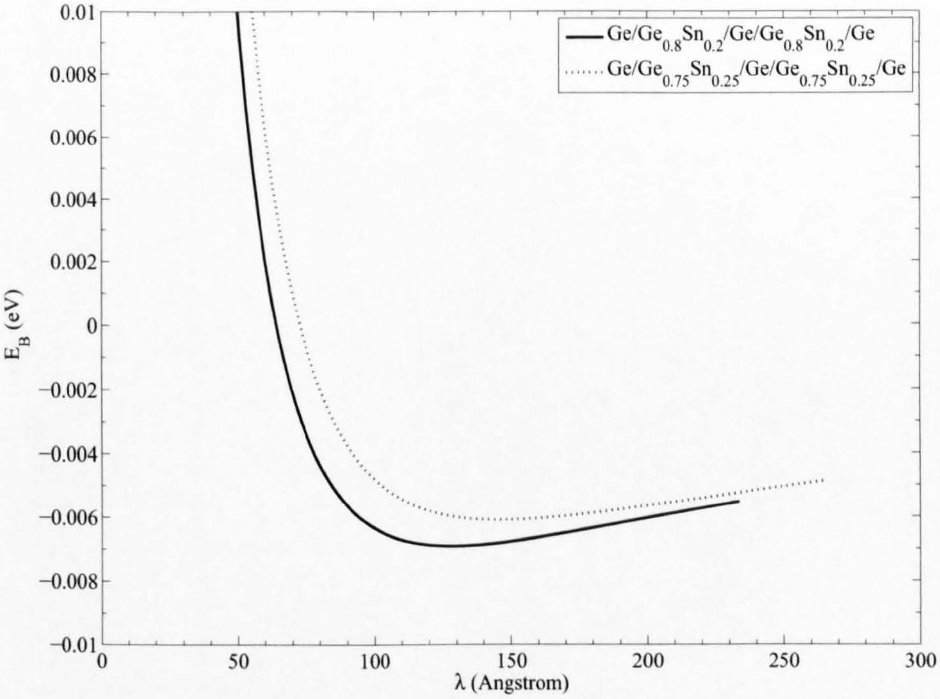

Figure 5.2: Minimization of the exciton binding energy by varying the variational parameter for Ge/Ge$_{0.80}$Sn$_{0.20}$/Ge/Ge$_{0.80}$Sn$_{0.20}$/Ge quantum wells (solid line) and Ge/Ge$_{0.75}$Sn$_{0.25}$/Ge/Ge$_{0.75}$Sn$_{0.25}$/Ge quantum wells (dotted line).

Within this picture the excitonic contribution to absorption, in terms of its amplitude and polarization properties, can be related to the interband absorption via [29]

$$\alpha_{exc}(\omega) = \frac{2\alpha_{2D}\hbar^2}{\mu^*}\frac{2}{\pi\lambda^2}L(\hbar\omega - \Delta E, \Gamma), \tag{5.8}$$

where α_{2D} is the plateau absorption between the two subbands, [29, 112, 113], ΔE is the exciton resonant transition energy and L the normalized Lorentzian with full width Γ. The (somewhat arbitrary, but roughly realistic) exciton linewidth of $\Gamma = 4$ meV (FWHM) was assumed. This is then added to the interband absorption. The influence of higher excitonic bound states and of the exciton unbound spectrum (above the interband threshold) was neglected. Common wisdom, derived from the wide-gap III/V EO modulators, would suggest that the strain–balanced SnGe structures are also polarization sensitive so that the absorption of in-plane, x-polarized light (the TE mode, in the usual waveguide notation) appears at lower energies, coming from the electron-heavy hole transition, while the z-polarized absorption appears at higher energies, coming from electron-light hole transitions. This is because, with the compressively strained wells, the heavy-hole band edge in wells shifts upwards and the light hole band edge downwards (while the opposite happens in the barriers). However, due to the small band gap the SnGe system behaves differently-the valence subbands therein have a strong admixture of the conduction band, S-like states, and the conduction subbands have a large contribution of P-like states, which strongly influences the polarization properties of the absorption spectrum.

5.3 Results and discussion

Test calculations were first performed for simple structures, i.e. single quantum wells without any electric field. Their electronic structure and optical absorption was calculated, with a couple of results shown in Figs. 5.3 and 5.4. One can notice that the absorption spectrum for the well in Fig. 5.4 is contributed from two transitions of energy states in the valence band, the first and second states from the top valence band. The first state is mostly P-like which mostly gives the absorption for the x-polarization and also gives some absorption for the z-polarization. The second energy transition, shown in Fig. 5.4(b), is between from the second state of the valence band, which is mostly S-like, and the first state of the conduction band, and gives rise to strong absorption for the z-polarization.

In the numerical investigations of EA modulators, the double coupled quan-

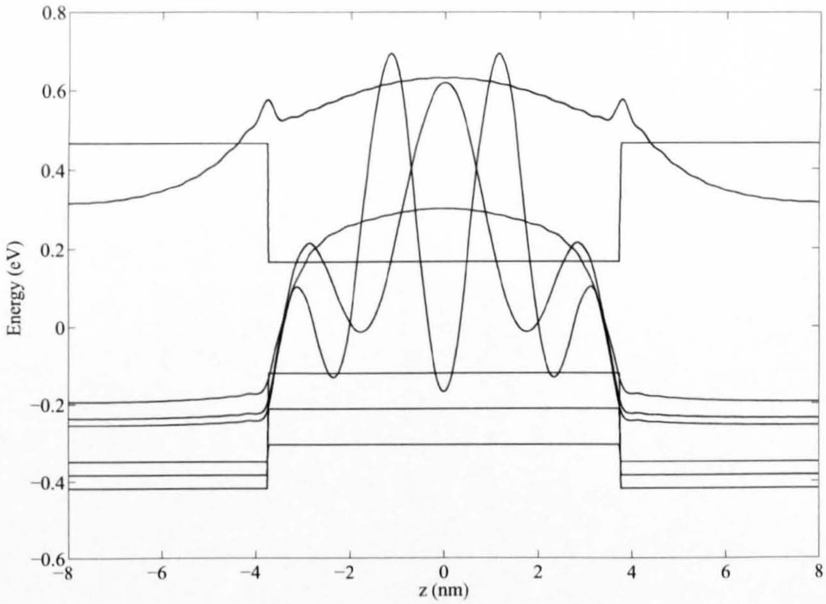

Figure 5.3: (a) Band edge profiles and wavefunctions in a $Ge_{0.95}Sn_{0.05}/Ge_{0.80}Sn_{0.20}/Ge_{0.95}Sn_{0.05}$ quantum well, of width 7.5 nm.

tum well system with pure Ge barriers was chosen, and the $Ge_{0.95}Sn_{0.05}$ alloy was chosen for the substrate. Different wavelength ranges, where EA modulation can be performed, can be accessed by using different values of the Sn mole fraction x in the wells, made of Sn_xGe_{1-x} alloy (via varying the bulk band gap), and to some extent also by tuning the well widths. The values of Sn content in the wells were set to $x = 0.20$, 0.25 and 0.28, so they are compressively strained, and the whole MQW structure can be made strain balanced, by inserting appropriate Ge barrier (buffer) layers between individual double-well units. The ratio of the wider and narrower well widths was varied in order to get as large a shift in the absorption threshold energy with the applied field as possible. The individual well widths were chosen to fit into a somewhat arbitrarily chosen, total thickness of 12 nm. The best results were obtained in structures with this ratio of about 3:2, in full agreement with the findings of Ref. [106]. Since the structures are asymmetric, a red shift is obtained for one, and a blue shift for the other polarity of the field, which in

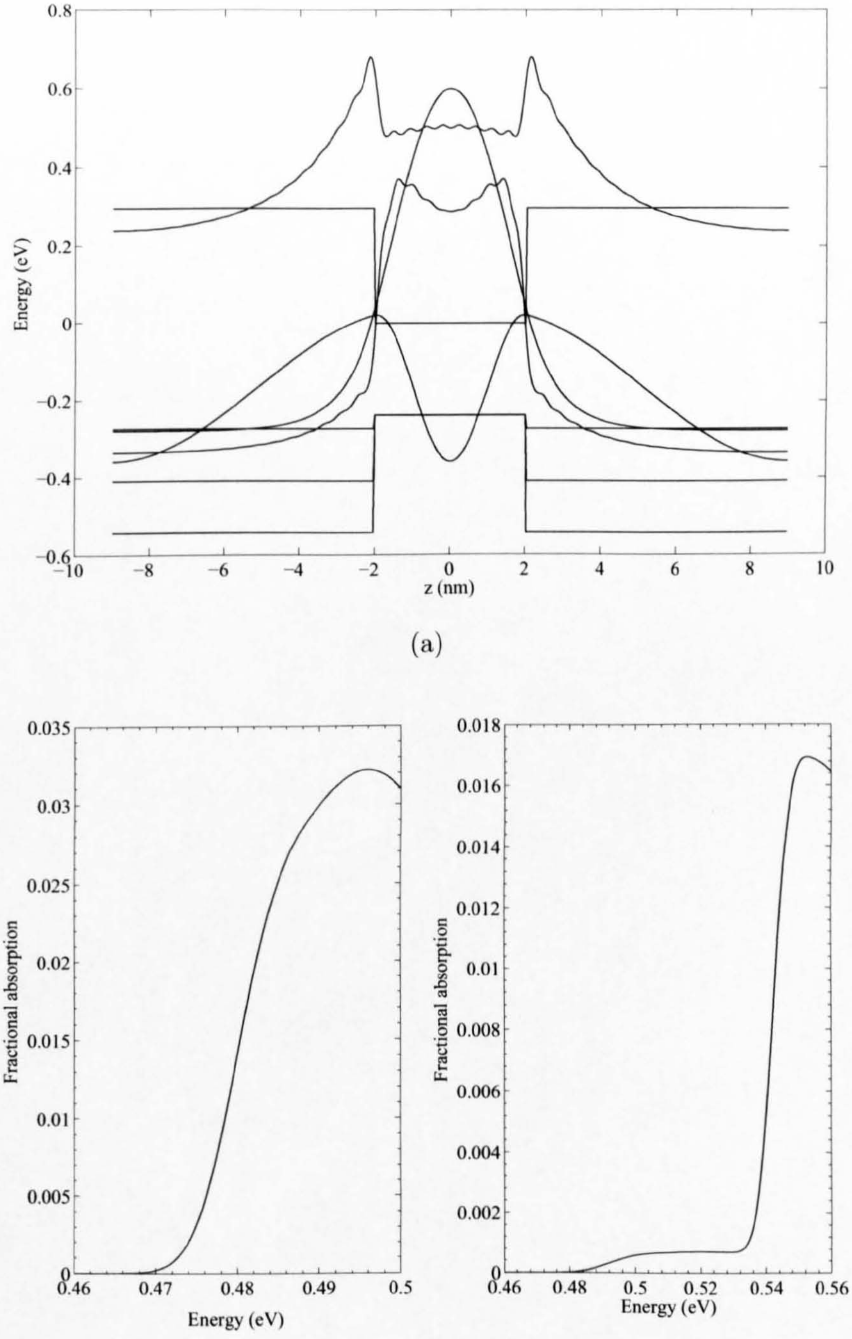

(a)

(b)

Figure 5.4: (a) Band edge profiles and wavefunctions in a Ge/$\mathrm{Ge_{0.80}Sn_{0.20}}$/Ge quantum well, of width 4 nm. (b) fractional absorption for x-polarization (left down) and in z-polarization (right down) fact extends the useful range of wavelengths that can be modulated (in symmetric structures only the red shift occurs). The calculated absorption spectra for z and x-polarization, in three structures designed for different wavelengths are shown in Figs. 5.5, 5.6 and 5.7. The convention used for the sign of the electric field F is that it is negative if directed from the narrower towards the wider well. In a MQW structure comprising a number of such unit cells, the thickness of a unit cell is 22 nm (only one of the outer barriers is assigned to a particular cell), and the fractional absorption of 0.01 (=1%) corresponds to the absorption coefficient of 4550 cm^{-1}.

The most interesting feature in all the examples is that the absorption for both the x- and z- polarization sets in at the same energy (which varies from one structure to another), meaning that both come from the same transition, the latter being a few times larger, which is unexpected in this, compressively strained well system. Inspection of the basis state content in subband wave functions shows that this is due to the fact that both the lowest conduction and the highest valence subbands have strong contributions of S states. The photon coupling between the S components, or between the two like P components, in the two subbands clearly gives rise to z-polarized absorption: a finite value of the transition matrix element there appears only because the envelope wavefunctions of basis states are modulated along the z-axis, while there is no dipole associated with the underlying basis states in this case (which is why this can be loosely called 'intraband-like process'). On the other hand, the coupling between the S component in one and the P components in the other subband gives rise to either x- or z-polarized absorption, with the dipole matrix element there coming from the basis states, and only being modulated by the overlap of envelope wavefunctions (hence this can be called 'interband-like process'). It is also worth noting that, in the opposite case of structures with tensilely strained wells, the absorption strengths for the two polarizations may be quite different. While such structures cannot be made as strain-balanced, as discussed above, this still indicates that it might be possible to achieve an

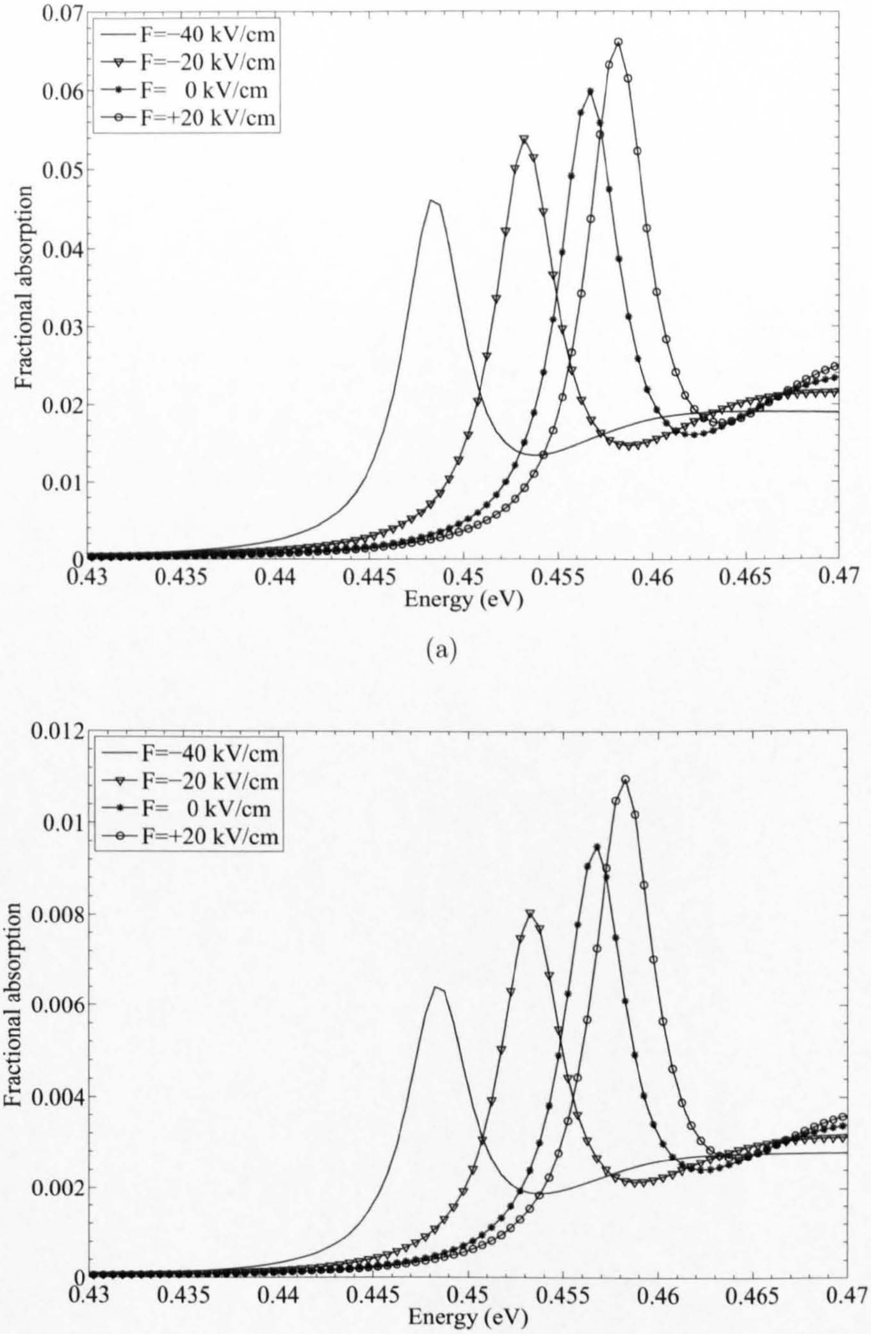

(a)

(b)

Figure 5.5: The dimensionless fractional absorption for a range of bias values of a strained double quantum well structure $Ge/Ge_{0.80}Sn_{0.20}/Ge/Ge_{0.80}Sn_{0.20}/Ge$, grown on a relaxed $Ge_{0.95}Sn_{0.05}$ substrate, with layer widths 8.0/4.5/2.0/7.5/8.0 nm, for (a) z- and (b) x-polarization.

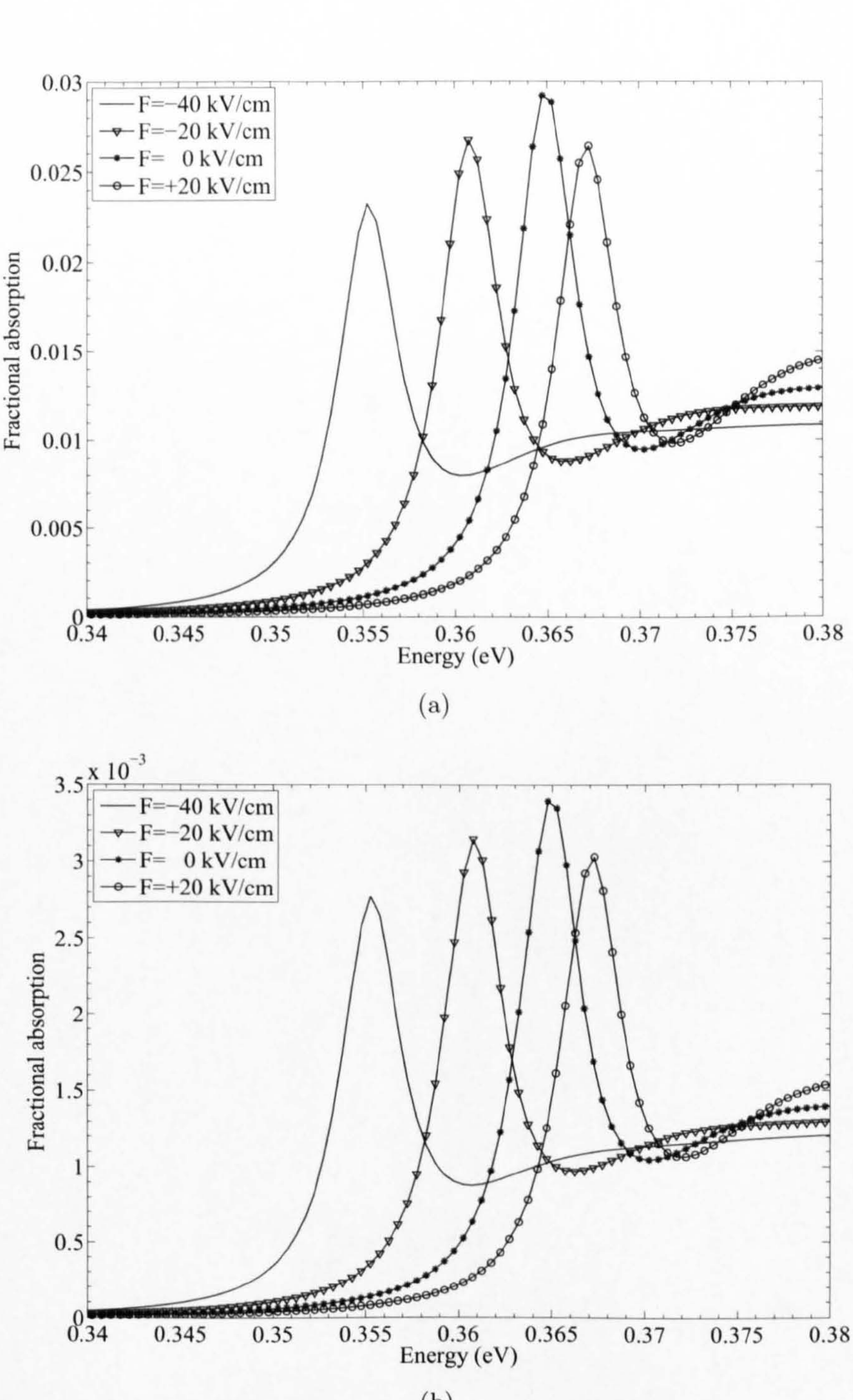

(a)

(b)

Figure 5.6: Same as in Fig.5.5, but for the Ge/Ge$_{0.75}$Sn$_{0.25}$/Ge/Ge$_{0.75}$Sn$_{0.25}$/Ge structure with layer widths 8.0/4.5/2.0/7.5/8.0 nm.

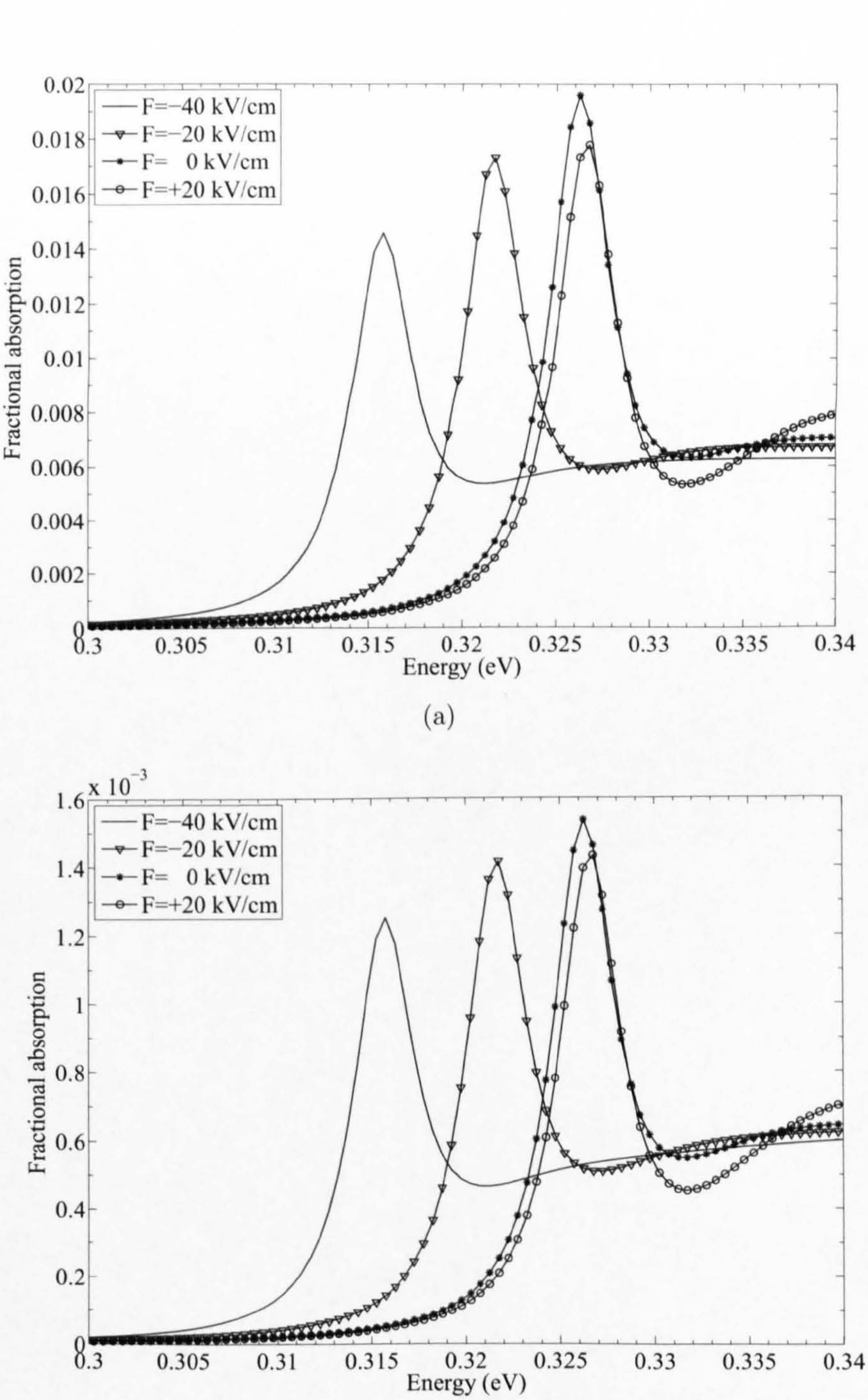

(a)

(b)

Figure 5.7: Same as in Fig.5.5, but for the Ge/Ge$_{0.72}$Sn$_{0.28}$/Ge/Ge$_{0.72}$Sn$_{0.28}$/Ge structure with layer widths 8.0/4.5/2.0/7.5/8.0 nm.

almost polarization-insensitive EA modulator by a more careful band structure engineering.

On the more practical side, the absorption in this system is technically quite significant: while the peak values due to excitonic enhancement may decrease somewhat, if the exciton linewidth comes out to be larger than assumed here, the values following the peaks are still large. In MQW structures with 22 nm wide unit cells (each comprising an ADQW) the absorption coefficients for the z-polarized light would be 9000 cm^{-1}, 4500 cm^{-1}, and 3000 cm^{-1} for the structures described in Figs. 5.5, 5.6 and 5.7, respectively. Although no calculations were performed for the indirect absorption in this system, these direct absorption coefficients would be well in excess of the background absorption if it has a similar value (500 cm^{-1}) as that reported for Ge/SiGe MQWs [111]. This should enable a good on/off transmission ratio, even more so if the excitonic peaks are used. In the range of fields shown in Figs. 5.5-5.7, the absorption remains large and only the threshold energy is tuned, but for fields away from this range the absorption starts to decrease due to a reduced overlap of electron and hole wavefunctions, which is a common feature of all EA modulators. By appropriately choosing the alloy composition of the wells one can tune the absorption wavelength, e.g. in the range of 0.31 eV to 0.46 eV (i.e. λ = 2.7 - 4 μm) in the examples given in Figs. 5.5, 5.6 and 5.7. It is likely that this range can be made somewhat wider, towards shorter wavelengths by lowering the Sn content in the wells (a constraint being that the barrier height must remain sufficient to confine the wavefunctions, otherwise the ternary SiGeSn would have to be employed), and towards longer wavelengths by using wider wells (a constraint being the presently unknown single-layer critical thickness of strained GeSn material), however this was not explored in detail. Interestingly, the absorption is not very sensitive to the exact value of strain in the wells and barriers. For instance, changing the Sn content in the substrate from 5% to 15% has hardly any effect on the absorption onset energy, which is most likely due to the basis state composition of subbands as it is in these structures, and is again different from the behaviour encountered in wider band gap systems.

Attempt was also made to design structures which are direct bandgap structures in order to enhance the efficiency of the devices. According to Ref. [93], $Ge_{1-x}Sn_x$ will be a direct bandgap semiconductor if tensile strain has been applied. In order to engineer double quantum wells to have a direct bandgap, the system is assumed grown on a substrate that can apply a suitable tensile strain to the quantum wells. This implies using $Ge_{1-y}Sn_y$, with $y \geq x$, as a substrate. The results of fractional absorption in one such structure are shown in Fig. 5.8. However this system can not be useful because the bandgap of the substrate is smaller than that of the active region and the width of the substrate layer is also wider. This causes the photon absorption efficiency in substrate to dominate. However, this problem can be overcome by choosing another substrate, which is also compatible with $Ge_{1-x}Sn_x$, and can apply tensile strain to the system by having larger lattice constant. The last requirement is to have a larger bandgap compared to $Ge_{1-x}Sn_x$ to behave like a barrier. Such a substrate is $Ge_{1-x-y}Si_ySn_x$, by adjusting the Ge, Si and Sn composition.

Finally, the'numerical experiments' were performed in which all the layers were attributed a 10% smaller band gap, while all other band structure parameters were kept constant. This led to a decrease of the absorption threshold by respectively 10% and 5% for any value of the field for the structures described in Figs. 5.5 and 5.6, which roughly indicates the temperature sensitivity and/or the temperature tuning capabilities of the modulator, by heating or cooling. On the other hand, the lowest-energy structure, Fig. 5.7, was quite insensitive (to within 2%, the transition energy changing between -3 meV and +6 meV, depending on the field). In narrow gap systems the absorption threshold is determined by the direct contribution of the band gap itself, and by the narrow-gap enhanced state mixing effects, wherefrom comes this unusual behaviour.

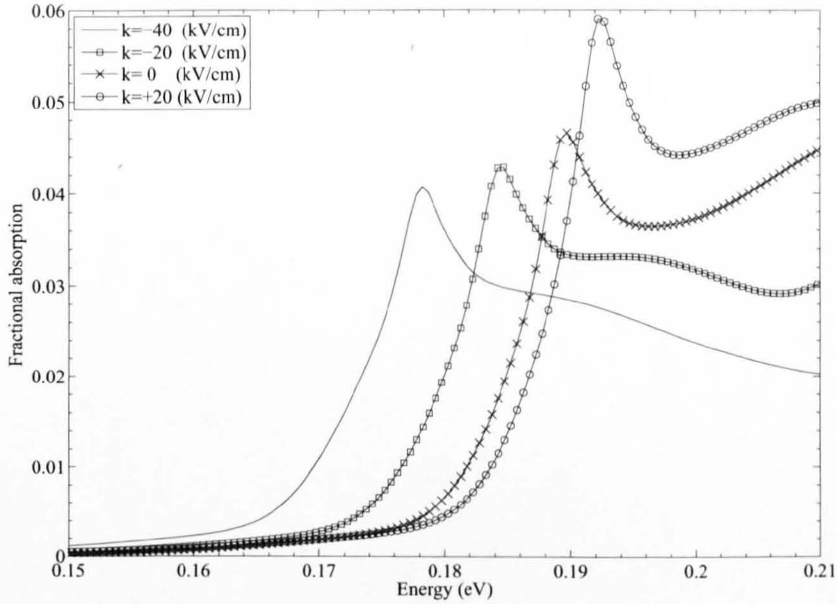

(a)

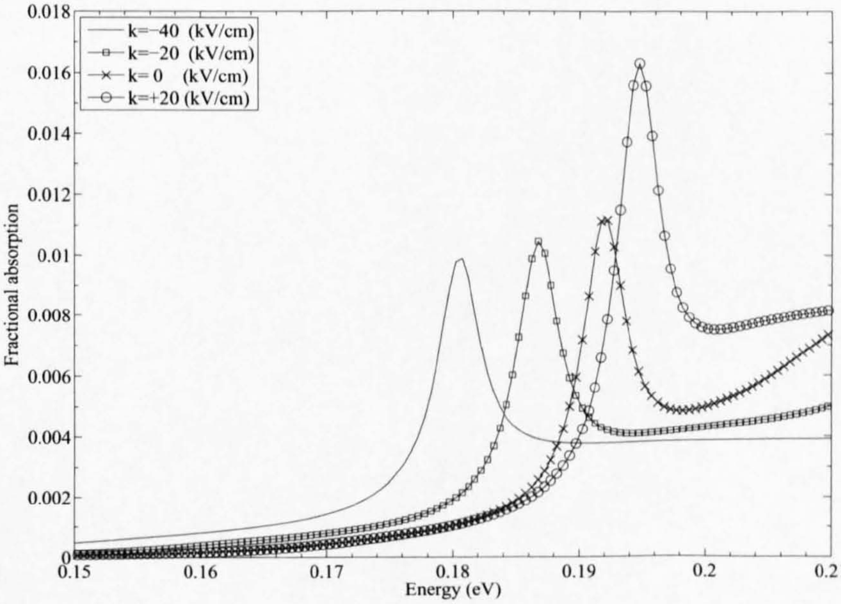

(b)

Figure 5.8: The dimensionless fractional absorption for a range of bias values of a strained barrier and relaxed well double quantum well structure $Ge_{0.95}Sn_{0.05}/Ge_{0.72}Sn_{0.28}/Ge_{0.95}Sn_{0.05}/Ge_{0.72}Sn_{0.28}/Ge_{0.95}Sn_{0.05}$, grown on a relaxed $Ge_{0.72}Sn_{0.28}$ substrate, with layer widths 8.0/4.5/2.0/7.5/8.0 nm, for (a) z- and (b) x-polarization. The well material has a direct band gap.

5.4 Conclusion

Using the 8-band **k·p** method asymmetric double quantum well structures based on SnGe alloys were designed, applicable for EA modulators in the mid-infrared spectral range. They show interesting polarization properties, different from what is usually encountered in the more conventional, wide bandgap III/V counterparts, and are predicted to offer practically useful performance as EA modulators.

Chapter 6

Conclusions and suggestions for future work

Throughout this concluding chapter, additional emphasis will be put into underlying the broader nature of the achievements presented as follows.

Alloys of silicon (Si), germanium (Ge) and tin (Sn) are continuously attracting research attention as possible direct band gap semiconductors with prospective applications in optoelectronics. The direct gap property may be brought about by the alloy composition alone or combined with the influence of strain, when an alloy layer is grown on a virtual substrate of different composition. In search for direct gap materials, the electronic structure of relaxed or strained $Ge_{1-x}Sn_x$ and $Si_{1-x}Sn_x$ alloys, and of strained Ge grown on relaxed $Ge_{1-x-y}Si_xSn_y$, was calculated in Chapter 3 by the self-consistent pseudo-potential plane wave method, within the mixed-atom supercell model of alloys, which was found to offer a much better accuracy than the virtual crystal approximation. Expressions are given for the direct and indirect band gaps in relaxed $Ge_{1-x}Sn_x$, strained Ge grown on relaxed $Si_xGe_{1-x-y}Sn_y$, and for strained $Ge_{1-x}Sn_x$ grown on a relaxed $Ge_{1-y}Sn_y$ substrate, and these constitute the criteria for achieving a direct band gap semiconductor, by using appropriate tensile strain. In particular, strained Ge on relaxed $Si_xGe_{1-x-y}Sn_y$ has a direct gap for $y > 0.12 + 0.20x$, while strained $Ge_{1-x}Sn_x$ on relaxed $Ge_{1-y}Sn_y$ has a direct gap for $y > 3.2x^2 - 0.07x + 0.09$. On the other hand, relaxed Sn_xSi_{1-x} alloys do not show a finite direct band gap.

Self-assembled quantum dots in the Si-Ge-Sn system attract research attention as possible direct band gap material, compatible with Si-based technology, with potential applications in optoelectronics. In Chapter 4, the electronic structure near the Γ-point and interband optical matrix elements of strained Sn and SnGe quantum dots in Si or Ge matrix are calculated using the eight-band $\mathbf{k} \cdot \mathbf{p}$ method, and the competing L-valley conduction band states were found by the effective mass method. The strain distribution in the dots was found with the continuum mechanical model. The parameters required for the $\mathbf{k} \cdot \mathbf{p}$ or effective mass calculation for Sn were extracted by fitting to the energy band structure calculated by the nonlocal empirical pseudopotential method (EPM). The calculations show that the self-assembled Sn/Si dots, sized between 4 nm and 12 nm, have indirect interband transition energies between 0.8 to 0.4 eV and direct interband transitions between 2.5 to 2.0 eV. In particular, the actually grown, approximately cylindrical Sn dots in Si with a diameter and height of about 5 nm are calculated to have an indirect transition (to the L valley) of about 0.7 eV, which agrees very well with experimental results. Similar good agreement with experiment was also found for SnGe dots grown on Si. However, neither of these are predicted to be direct band gap materials, in contrast to some earlier expectations.

A similar strategy was applied in Chapter 5. In order to extend the suite of Si-based optoelectronic devices, electroabsorption modulators based on SnGe asymmetric double quantum wells were considered. Structures strongly sensitive to electric field were disigned, by using the framework of $\mathbf{k} \cdot \mathbf{p}$ method. Asymmetric double quantum wells (ADQWs) are optimized to exhibit maximum optical modulation sensitivity by varying the barrier width, barrier position, and well width. In order to have interband transition energy ranges in the photon wavelength range of interest (mid-infrared), suitable Sn compositions of each layer were determined. Then, the electronic structure and optical properties, (absorption coefficient) were calculated. With 2 nm barrier and 12 nm total well width, a strong electric field sensitivity was achieved in structures with a ratio of wider well width and the narrower well width of about 3:2 which is in good agreement with other published values. They show interesting polarization properties, different from what is usually encountered in the more conventional, wide bandgap III/V counterparts. The optical absorption coefficient also illustrates that the Ge/$Ge_{0.8}Sn_{0.2}$/Ge/$Ge_{0.8}Sn_{0.2}$/Ge, grown on relaxed $Ge_{0.95}Sn_{0.05}$, can be used for an optical modulator for photon energy about 0.46 eV (corresponding to wavelength about 2.7 μm). The photon energy range 0.35 eV can be covered by the double quantum wells with 25% of Sn composition in the two well layers, while that with 28% of Sn composition can be used at 0.31 eV, corresponding to 4 μm.

6.1 Suggestions for future work

An investigation of properties of binary and ternary Si-Ge-Sn alloys is still in its infancy and also need time, research and money to achieve the main purpose. This milestone is an understanding of both mechanical and electrical properties of these alloys and an ability to produce optoelectronic device from these alloys. The most important reason for this is that they are perfectly compatible with silicon technology, widely used nowdays. A thorough understanding of these alloys in terms of theory and experiment is necessary. The work presented in this thesis gives a comprehensive theory of electronic structure and optical properties calculations for interband SiGeSn semiconductor devices, and also opens many other research directions in view of improving the existing models, applying them to different devices, as well as the development of calculation methodology. Some of these directions are described next.

- **Improving the existing model to increase the accuracy of calculations.** This should be done by using total energy density functional calculation and more accurate exchange-correlation potential. Moreover, in order to improve the reality of the model, the size of super cell which is considered should be expanded. With the new methods of calculation, the dielectric function, composition dependence of electronic and physical properties, phonon and elastic constants should be calculated.

- **SiGeSn quantum cascade laser.** The quantum cascade laser (QCL) is another research direction in view of applying SiGeSn alloys to different devices. An interssubband semiconductor laser, consisting of periodically repeated carefully engineered multiple quantum wells that direct the electronic transport along the desired path, may produce gain in the mid- and far-infrared (THz) region.

- **A whole SiGeSn semiconductor device simulation, such as p-i-n laser diode.** Semiconductor device modeling involves diffusion processes for hole and electron concentrations, as well as electric potential distribution. Thermal effects are also a factor. Semiconductor models often include multiphysics couplings and have highly nonlinear material properties, making them difficult to solve. Whole SiGeSn semiconductor devices can be considered by using a finite element simulation software as a new calculation methodology development.

Appendix A

Material parameters

Material parameters used in this work are summarized in this Appendix.

Table A.1: Material parameters of Si, Ge and some bowing parameters of $Si_{1-x}Ge_x$ which relevant for bandstructure calculations

Parameter		Si	Ge	bowing
Lattice constant [Å]	a	5.4310	5.6577	-0.027
Energy gap [eV]	E_g	4.185	0.898	
Spin-orbit splitting [eV]	Δ_{so}	0.044	0.297	
Effective mass at Γ point [m_0]	m^*	0.156	0.038	
Luttinger parameters	γ_1^L	4.285	13.38	
	γ_2^L	0.339	4.24	
	γ_3^L	1.446	5.69	
Interband matrix element [eV]	E_P	21.60	26.30	
Chemical valence band offset [eV]	VBO	1.17	0.69	
Deformation potentials [eV]	a_c	1.98	-8.24	
	a_v	2.46	1.24	
	b	-2.1	-2.9	
	d	-4.85	-5.3	
Elastic stiffness constants [GPa]	C_{11}	1657	1285	
	C_{12}	640	483	
	C_{44}	796	668	

Table A.2: Material parameters of Ge, Sn and some bowing parameters of $Ge_{1-x}Sn_x$ which relevant for bandstructure calculations

Parameter		Ge	Sn	bowing
Lattice constant [Å]	a	5.6577	6.4892	-0.166
Energy gap [eV]	E_g	0.898	-0.408	-2.49
Spin-orbit splitting [eV]	Δ_{so}	0.297	0.705	
Effective mass at Γ point [m_0]	m^*	0.038		
Luttinger parameters	γ_1^L	13.38	-25.19	
	γ_2^L	4.24	-15.10	
	γ_3^L	5.69	-13.53	
Interband matrix element [eV]	E_P	26.30	26.30	
Chemical valence band offset [eV]	VBO	0.69	0.00	
Deformation potentials [eV]	a_c	-8.24	-8.71	
	a_v	1.24	1.62	
	b	-2.9	-2.01	
	d	-5.3	-0.39	
Elastic stiffness constants [GPa]	C_{11}	1285	690	
	C_{12}	483	293	
	C_{44}	668	362	

References

[1] S. R. M. Levinstein and M. Shur, *Handbook Series on Semiconductor Parameters* (London: World Scientific, 1999).

[2] L. Pavesi and D. J. Lockwood, *Silicon photonics* (Berlin: Springer-Verlag, 2004).

[3] J. R. Chelikowsky and M. L. Cohen, Phys. Rev. B **14**, 556 (1976).

[4] G. He and H. A. Atwater, Phys. Rev. Lett. **79**, 1937 (1997).

[5] R. A. Soref and C. H. Perry, Journal of Applied Physics **69**, 539 (1991).

[6] R. A. Soref and L. Friedman, Superlattices and microstructures **14**, 189 (1993).

[7] W. Kohn and L. J. Sham, Phys. Rev. **140**, A1133 (1965).

[8] R. M. Martin, *Electronic Structure: Basic Theory and Practical Methods* (Cambridge University Press, 2004).

[9] E. Kaxiras, *Atomic and Electronic Structure of Solids* (Cambridge: Cambridge University Press, 2003).

[10] J. Thijssen, *Computational Physics* (Cambridge University Press, 2007).

[11] P. Moontragoon, Ground state energy of solid metallic hydrogen by the Wigner-Seitz method and APW, Master's thesis, Chulalongkorn University, Thailand, 2003.

[12] M. Born and J. R. Oppenheimer, Ann. Physik. **84**, 457 (1927).

[13] J. C. Slater, *Self-consistent Field for Molecules and Solids; Quantum Theory of Molecules and Solids* (New York: McGraw-Hill, 1974).

[14] P. Hohenberg and W. Kohn, Phys. Rev. **136**, B864 (1964).

[15] G. P. Srivastava, Journal of Physics C: Solid State Physics **15**, 707 (1982).

[16] J. C. Slater, Phys. Rev. **34**, 1293 (1929).

[17] P. E. Blöchl, O. Jepsen, and O. K. Andersen, Phys. Rev. B **49**, 16223 (1994).

[18] P. Harrison, *Quantum Wells, Wires and Dots; Theoritical and Computational Physics* (Chichester: Wiley, 2005).

[19] L. M. Falicov and P. J. Lin, Phys. Rev. **141**, 562 (1966).

[20] P. Friedel, M. S. Hybertsen, and M. Schlüter, Phys. Rev. B **39**, 7974 (1989).

[21] M. V. Fischetti and S. E. Laux, Journal of Applied Physics **80**, 2234 (1996).

[22] J. E. Bernard and A. Zunger, Phys. Rev. B **36**, 3199 (1987).

[23] T. K. B. S. Bloom, physica status solidi (b) **42**, 0370 (1970).

[24] N. Vukmirovic, *Physics of intraband quantum dot optoelectronic devices*, Dissertation, University of Leeds, 2007.

[25] J. M. Luttinger, Phys. Rev. **102**, 1030 (1956).

[26] J. M. Luttinger and W. Kohn, Phys. Rev. **97**, 869 (1955).

[27] C. R. Pidgeon and R. N. Brown, Phys. Rev. **146**, 575 (1966).

[28] T. B. Bahder, Phys. Rev. B **41**, 11992 (1990).

[29] G. Bastard, *Wave Mechanics Applied to Semiconductor Heterostructures* (Les editions de physique, Les Ulis, 1992).

[30] J. Stangl, V. Holý, and G. Bauer, Rev. Mod. Phys. **76**, 725 (2004).

[31] N. Vukmirovic, Z. Gacevic, Z. Ikonic, D. Indjin, P. Harrison, and V. Milanovic, Semiconductor Science and Technology **21**, 1098 (2006).

[32] O. Stier, M. Grundmann, and D. Bimberg, Phys. Rev. B **59**, 5688 (1999).

[33] C. Pryor, Phys. Rev. B **57**, 7190 (1998).

[34] T. Nakaoka, T. Saito, J. Tatebayashi, and Y. Arakawa, Phys. Rev. B **70**, 235337 (2004).

[35] H. Jiang and J. Singh, Phys. Rev. B **56**, 4696 (1997).

[36] O. Stier, *Electronic and Optical Properties of Quantum Dots and Wires* (Wissenschaft & Technik Verlag, Berlin, 2000).

[37] G. A. Baraff and D. Gershoni, Phys. Rev. B **43**, 4011 (1991).

[38] M. A. Cusack, P. R. Briddon, and M. Jaros, Phys. Rev. B **54**, R2300 (1996).

[39] S.-S. Li, J.-B. Xia, Z. L. Yuan, Z. Y. Xu, W. Ge, X. R. Wang, Y. Wang, J. Wang, and L. L. Chang, Phys. Rev. B **54**, 11575 (1996).

[40] A. D. Andreev and E. P. O'Reilly, Phys. Rev. B **62**, 15851 (2000).

[41] S. Tomić, A. G. Sunderland, and I. J. Bush, J. Mater. Chem. **16**, 1963 (2006).

[42] S. Tomić, Phys. Rev. B **73**, 125348 (2006).

[43] V. Mlinar, M. Tadić, and F. M. Peeters, Phys. Rev. B **73**, 235336 (2006).

[44] M. Tadić, F. M. Peeters, and K. L. Janssens, Phys. Rev. B **65**, 165333 (2002).

[45] M. Roy and P. A. Maksym, Phys. Rev. B **68**, 235308 (2003).

[46] J. D. Jackson, *Classical Electrodynamics* (John Wiley & Sons, 1999).

[47] J. Menéndez and J. Kouvetakis, Applied Physics Letters **85**, 1175 (2004).

[48] D. W. Jenkins and J. D. Dow, Phys. Rev. B **36**, 7994 (1987).

[49] K. A. Mader, A. Baldereschi, and H. von Knel, Solid State Communications **69**, 1123 (1989).

[50] M. R. Bauer, J. Tolle, C. Bungay, A. V. G. Chizmeshya, D. J. Smith, J. Menndez, and J. Kouvetakis, Solid State Communications **127**, 355 (2003).

[51] V. R. D'Costa, C. S. Cook, A. G. Birdwell, C. L. Littler, M. Canonico, S. Zollner, J. Kouvetakis, and J. Menéndez, Phys. Rev. B **73**, 125207 (2006).

[52] B. B. M. F. Y. Chibane, physica status solidi (b) **240**, 116 (2003).

[53] M. Schlüter, J. R. Chelikowsky, S. G. Louie, and M. L. Cohen, Phys. Rev. B **12**, 4200 (1975).

[54] J. D. Sau and M. L. Cohen, Phys. Rev. B **75**, 045208 (2007).

[55] L. Vegard, Zeitschrift fr Physik A Hadrons and Nuclei **5**, 17 (1921).

[56] S. Krishnamurthy, A. Sher, and A.-B. Chen, Applied Physics Letters **47**, 160 (1985).

[57] S. C. Jain, J. R. Willis, and R. Bullough, Advances in Physics **39**, 127 (1990).

[58] N. Bouarissa and F. Annane, Materials Science and Engineering B **95**, 100 (2002).

[59] M. M. Rieger and P. Vogl, Phys. Rev. B **48**, 14276 (1993).

[60] P. Aella, C. Cook, J. Tolle, S. Zollner, A. V. G. Chizmeshya, and J. Kouvetakis, Applied Physics Letters **84**, 888 (2004).

[61] H. P. L. de Guevara, A. G. Rodríguez, H. Navarro-Contreras, and M. A. Vidal, Applied Physics Letters **84**, 4532 (2004).

[62] M. Bauer, J. Taraci, J. Tolle, A. V. G. Chizmeshya, S. Zollner, D. J. Smith, J. Menendez, C. Hu, and J. Kouvetakis, Applied Physics Letters **81**, 2992 (2002).

[63] J. Tolle, A. V. G. Chizmeshya, Y.-Y. Fang, J. Kouvetakis, V. R. D'Costa, C.-W. Hu, J. Menéndez, and I. S. T. Tsong, Applied Physics Letters **89**, 231924 (2006).

[64] V. Fiorentini and A. Baldereschi, Journal of Physics: Condensed Matter **4**, 5967 (1992).

[65] R. Ragan, K. S. Min, and H. A. Atwater, Materials Science and Engineering B **87**, 204 (2001).

[66] Y. Lei, P. Möck, T. Topuria, N. D. Browning, R. Ragan, K. S. Min, and H. A. Atwater, Applied Physics Letters **82**, 4262 (2003).

[67] I. Arslan, T. J. V. Yates, N. D. Browning, and P. A. Midgley, Science **309**, 2195 (2005).

[68] A. Karim, G. Hansson, W.-X. Ni, P. Holtz, M. Larsson, and H. Atwater, Optical Materials **27**, 836 (2005).

[69] R. Ragan, *Direct Energy Bandgap Group IV Alloys and Nanostructures*, Dissertation, California Institute of Technology, 2002.

[70] S. Richard, F. Aniel, and G. Fishman, Phys. Rev. B **70**, 235204 (2004).

[71] L.-W. Wang, A. Franceschetti, and A. Zunger, Phys. Rev. Lett. **78**, 2819 (1997).

[72] D. Ahn, Journal of Applied Physics **98**, 033709 (2005).

[73] K. Ohno, K. Esfarjani, and Y. Kawazoe, *Computational materials science: from ab initio to Monte Carlo methods* (Springer, 1999).

[74] H. Lopez, A. N. Chantis, J. Sune, and X. Cartoixa, Journal of Computational Electronics **6**, 195 (2007).

[75] P. Yu, J. Wu, and B.-F. Zhu, Phys. Re. B **73**, 235328 (2006).

[76] T. Brudevoll, D. S. Citrin, M. Cardona, and N. E. Christensen, Phys. Rev. B **48**, 8629 (1993).

[77] S. Adachi, Journal of Applied Physics **66**, 813 (1989).

[78] H. U. Middelmann, L. Sorba, V. Hinkel, and K. Horn, Phys. Rev. B **35**, 718 (1987).

[79] G. P. Srivastava, Journal of Physics C: Solid State Physics **16**, 1649 (1983).

[80] D. J. Dugdale, S. Brand, and R. A. Abram, Phys. Rev. B **61**, 12933 (2000).

[81] W. H. Press, S. A. Teukolsky, W. T. Vetterling, and B. P. Flannery, *Numerical Recipes in Fortran 77* (Cambridge:Cambridge University Press, 1992).

[82] M. P. C. M. Krijn, Semiconductor Science and Technology **6**, 27 (1991).

[83] C. G. Van de Walle, Phys. Rev. B **39**, 1871 (1989).

[84] S. Birner, T. Zibold, T. Andlauer, T. Kubis, M. Sabathil, A. Trellakis, and P. Vogl, IEEE Transactions on Electron Devices **54**, 2137 (2007).

[85] S. Ridene, K. Boujdaria, H. Bouchriha, and G. Fishman, Phys. Rev. B **64**, 085329 (2001).

[86] P. Lawaetz, Phys. Rev. B **4**, 3460 (1971).

[87] B. L. Booth and A. W. Ewald, Phys. Rev. **168**, 805 (1968).

[88] B. J. Roman and A. W. Ewald, Phys. Rev. B **5**, 3914 (1972).

[89] M. Cardona and F. H. Pollak, Phys. Rev. **142**, 530 (1966).

[90] M. Jaros, Phys. Rev. B **37**, 7112 (1988).

[91] P. Mock, Y. Lei, T. Topuria, N. D. Browning, R. Ragan, K. S. Min, and H. A. Atwater, Physical Chemistry of Interfaces and Nanomaterials **4807**, 71 (2002).

[92] Z. Yang, Y. Shi, J. Liu, B. Yan, R. Zhang, Y. Zheng, and K. Wang, Materials Letters **58**, 3765 (2004).

[93] P. Moontragoon, Z. Ikonic, and P. Harrison, Semiconductor Science and Technology **22**, 742 (2007).

[94] J. Kouvetakis, J. Menendez, and A. Chizmeshya, Annual Review of Materials Research **36**, 497 (2006).

[95] J. Kouvetakis and A. V. G. Chizmeshya, Journal of Materials Chemistry **17**, 1649 (2007).

[96] Y. Nakamura, A. Masada, and M. Ichikawa, Applied Physics Letters **91**, 013109 (2007).

[97] Y. Nakayama, K. Takase, T. Hirahara, S. Hasegawa, T. Okuda, A. Harasawa, I. Matsuda, Y. Nakamura, and M. Ichikawa, Japanese Journal of Applied Physics **46**, L1176 (2007).

[98] R. Soref, IEEE Journal of Selected Topics in Quantum Electronics **12**, 1678 (2006).

[99] P. Moontragoon, N. Vukmirovic, Z. Ikonic, and P. Harrison, Journal of Applied Physics **103**, 103712 (2008).

[100] Y.-Y. Fang, J. Xie, J. Tolle, R. Roucka, V. R. DCosta, A. V. G. Chizmeshya, J. Menendez, and J. Kouvetakis, Journal of the American Chemical Society **130**, 16095 (2008).

[101] S.-W. Chang and S. L. Chuang, Quantum Electronics, IEEE Journal of **43**, 249 (2007).

[102] G. Sun, H. H. Cheng, J. Menéndez, J. B. Khurgin, and R. A. Soref, Applied Physics Letters **90**, 251105 (2007).

[103] R. Soref, Proceeding SPIE **6898**, 689809 (2008).

[104] J. Thalken, W. Li, S. Haas, and A. F. J. Levi, Applied Physics Letters **85**, 121 (2004).

[105] M. Aguilar, M. Carrascosa, F. Agulló-López, F. Agulló-Rueda, M. R. Melloch, and D. D. Nolte, Journal of Applied Physics **86**, 3822 (1999).

[106] D. K. Kim and D. Citrin, IEEE Journal of Quantum Electronics **43**, 651 (2007).

[107] D. K. Kim and D. Citrin, IEEE Journal of Quantum Electronics **43**, 765 (2007).

[108] H. Alause, W. Knap, J. L. Robert, R. Planel, V. Thierry-Mieg, F. H. Julien, K. Zekentes, and V. Mosser, Semiconductor Science and Technology **15**, 724 (2000).

[109] G. T. Reed and C. J. Png, Materials Today **8**, 40 (2005).

[110] W. C. Dash and R. Newman, Phys. Rev. **99**, 1151 (1955).

[111] Y.-H. Kuo, Y. K. Lee, Y. Ge, S. Ren, J. E. Roth, T. I. Kamins, D. A. B. Miller, and J. S. Harris, Nature **437**, 1334 (2005).

[112] D. A. B. Miller, D. S. Chemla, T. C. Damen, A. C. Gossard, W. Wiegmann, T. H. Wood, and C. A. Burrus, Phys. Rev. B **32**, 1043 (1985).

[113] N. Susa, Journal of Applied Physics **73**, 932 (1993).